University of Oxford

D. Phil. Thesis

Fluid venting phenomena in the Eastern Mediterranean

Luke M. Kearney

Supervisors: Prof. Richard F. Katz, Prof. Christopher W. MacMinn and Prof. Joe Cartwright

A thesis submitted for the degree of Doctor of Philosophy

Department of Earth Sciences

Jesus College

Declaration of Authorship

I declare that the contents of this thesis are my own. The contents of Chapter 2 have been published in Kearney et al. (2023) and the contents of Chapter 3 have been published in Kearney et al. (2024). I was the lead author of both studies, my contribution to these works is indicated in the statements of authorship at the end of each of these chapters.

Luke M. Kearney

Trinity Term, 2024

Acknowledgements

Firstly, I am tremendously grateful to my supervisors Richard Katz, Christopher MacMinn and Joe Cartwright. I thank Rich for his mentorship, insight and boundless enthusiasm for science. I thank Chris for his patience and guidance, as well as his unwavering optimism. I thank Joe, whose exceptional knowledge of the subsurface has been instrumental in ensuring the empirical grounding of my research.

My thanks go to the members of FOALAB and the Poromechanics Lab for the regular feedback and camaraderie that they have provided throughout. I also thank Chris Kirkham for his invaluable advice and helpful discussions. I am indebted to Seth Flaxman and the members of the Machine Learning & Global Health Network for introducing me to the world of point processes and Bayesian statistics.

I thank my friends in Oxford. In particular, I thank Joe Fishlock, who has been a constant source of support and insightful scientific discussion. I also thank Anna Jones, Alice Edney and Sophie Harbord for sharing their time, company and doctoral journeys with me.

I thank my family, who remain steadfast in their encouragement and confidence in me. Finally, I thank Leila for her endless love and support.

Table of Contents

Abstract

Fluid venting poses clear risks to various industrial applications including carbon dioxide sequestration. To assess these risks, a detailed understanding of the conditions for fluid venting is required. While *in-situ* measurements of these conditions are scarce, recent observations of natural fluid vents in the Eastern Mediterranean provide robust constraints for the validation of predictive models. In this thesis, I develop a general theory of fluid venting and test it against these observations.

I begin by examining episodic fluid venting. Venting is widely interpreted to occur via hydraulic fracturing, requiring near-lithostatic pore pressures. I propose that fluid expulsion causes a local pressure drop that is gradually recharged by ongoing basin-wide pressurisation and by pressure diffusion, whereby fluid flows from neighbouring regions. Pressure diffusion is predicted to be a major contributor to episodic venting globally.

I compare the predictions from my theory with the geological record of episodic fluid venting from the Levant Basin, where venting has been estimated to occur every ∼100 kyr. I invert these venting observations for a pressure recharge rate of ∼30 MPa/Myr. To explain this rate, I quantify and compare a range of candidate mechanisms. I find that pressure diffusion from neighbouring mudstones provides the most plausible explanation.

Remobilised mudstones are commonly expelled from fluid vents known as mud volcanoes, a significant geohazard. However, the mechanisms by which mudstones are remo-

bilised remain unclear. Observations of mud volcanoes from the Nile Deep Sea Fan reveal thinning of the mudstone unit in bowl-shaped zones at the base of each vent, resulting from mud depletion. I present a model of mud volcanism, whereby rapid fluid expulsion drives mudstone remobilisation. The model predicts that remobilisation spreads radially from the base of the vent, forming a bowl-shaped mud-depletion zone. I show that the predicted size of depletion zones is consistent with observed sizes.

Chapter 1

Introduction

Sedimentary basins can provide the capacity to sequester carbon dioxide and store hydrogen fuel. Current approaches to determining the feasibility of, and the risks involved in, subsurface fluid storage rely on accurate fluid and solid mechanical models. Subsurface fluid storage has been modelled extensively as the lateral, buoyancy-driven migration of the injected fluid through a porous aquifer (Huppert & Neufeld 2014). The majority of such models assume the presence of an overlying, impermeable sealing rock preventing the vertical migration of pore fluids. However, natural fluid vents in sedimentary basins demonstrate that even vanishingly low-permeability salt seals can be breached, allowing fluids to escape. Consequently, there is a need to better understand the conditions leading to seal failure.

To this end, the geological record of natural fluid vents provides a rare opportunity for testing related hypotheses using quantitative models. In particular, recent high-resolution 3-D seismic data from across the Eastern Mediterranean reveal a comprehensive record of venting over the past ∼6 Myr. Hitherto, there are few existing quantitative models of fluid venting; these existing models are computationally expensive as they typically include

additional physical, chemical and thermodynamical machinery (Dewers & Ortoleva 1994, L'Heureux & Fowler 2000). As such, these models cannot fully explore the associated parameter space governing fluid venting and thus are limited to the study of specific settings. Rather, a comprehensive overview of the dynamics of fluid venting can be obtained with a minimal model that incorporates the fundamental physical processes involved.

In many areas of the Eastern Mediterranean, fluid vents expel subsurface sediments such as remobilised mudstones (i.e., mud); these vents are known as mud volcanoes. Mud volcanoes produce massive effusions of hydrocarbon-rich mud and thus present a significant geohazard as the growing mud edifice can threaten both people and infrastructure. One notable example is the Lusi mud volcano, a drilling-induced environmental disaster in East Java that has been erupting since 2006 at an economic cost of billions of USD (Tingay et al. 2015, 2018). The broad consensus is that the remobilisation of subsurface sediment during mud volcano eruptions occurs during the rapid expulsion of gas-saturated fluids (Kopf 2002, Mazzini & Etiope 2017). However, the mechanism by which the sediment is remobilised and expelled remains understudied, and thus is an ideal target for investigation.

In this thesis, I develop a simplified theory of fluid venting from sedimentary basins that incorporates ongoing, basin-wide pressurisation and fluid flow between sedimentary layers. I show that the predictions of this theory are consistent with observations of episodic fluid venting from the Levant Basin, Eastern Mediterranean. I then extend this theory to include the subsurface remobilisation of sediment during mud volcano eruptions. Predictions from the extended theory agree with observations of mud volcanoes from the Nile Deep Sea Fan, Eastern Mediterranean.

In this introductory chapter, I summarise observations of fluid venting phenomena,

including recent observations from the Eastern Mediterranean, and state the open questions raised by these observations. I then discuss the strategy for using models to address these questions and the basic assumptions that are needed to build such models. Finally, I outline the structure of the remainder of this thesis.

1.1 Observations of fluid venting phenomena

Fluid venting phenomena have been frequently observed in sedimentary basins globally since they were first identified from seismic images in the 1980s (Hovland & Judd 1988). Seismic images are produced by propagating seismic waves into the Earth and recording the returning waves that result from reflection or refraction by distinct subsurface features (Yilmaz 2001). The returning waves are recorded by detectors that are distributed along the surface. The recorded waves that have been disrupted by these vents therefore reveal their presence. The vents themselves are localised vertical pathways known as fluid-escape pipes, named after the columnar zones of disrupted reflections that they produce on seismic images (Figure 1.1a). The diameters of fluid-escape pipes are estimated using the lateral extents of these disrupted reflections, commonly of order tens of metres. However, this length-scale corresponds to the lateral resolution of conventional seismic images, which is typically limited by the spacing of the surface detectors. Therefore, such measurements of pipe diameter may be significantly exaggerated. These limitations due to resolution are less problematic for measurements of the vertical extents of pipes. Fluid-escape pipes can extend over kilometres vertically (Cartwright & Santamarina 2015) and thus enable the transport of fluid through thick successions of low-permeability rock.

Fluid-escape pipes are commonly observed in sedimentary basins that consist primarily of fine-grained sedimentary rocks known as mudstones. Mudstones generally have low permeabilities due to their fine grain sizes. Therefore, an increase in pore pressure

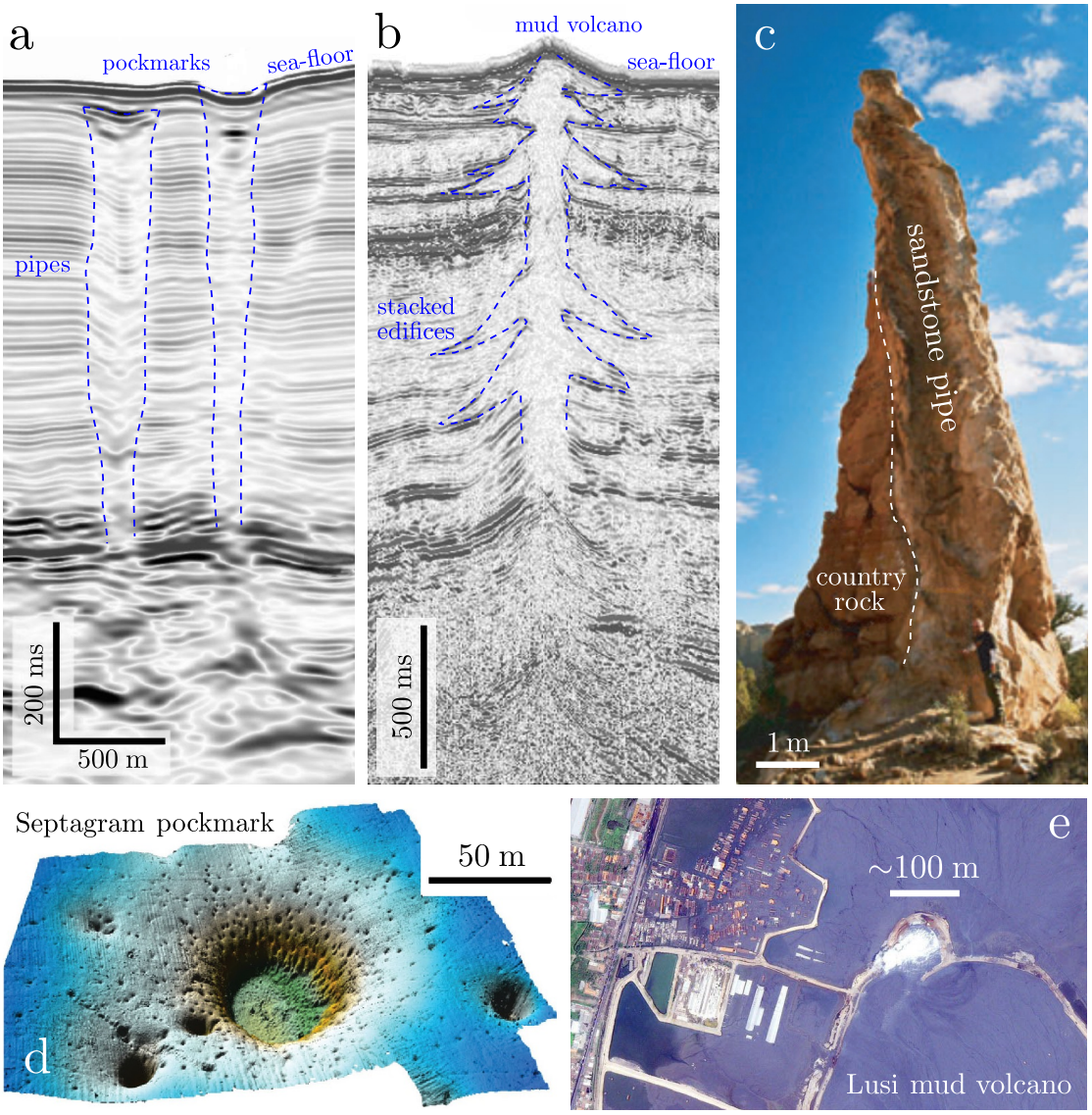

Figure 1.1: Examples of fluid venting phenomena. (a) Seismic image of two fluid-escape pipes from the Levant Basin, Eastern Mediterranean; adapted from Oppo et al. (2021). (b) Seismic image of a mud volcano from offshore Trinidad; adapted from Deville et al. (2010). (c) Relict sandstone pipe in the Kodachrome Basin, Utah; adapted from Huuse et al. (2005). (d) High-resolution bathymetry of the Septagram pockmark, offshore Norway, showing a 15 m-deep circular depression with a flat interior; adapted from Mazzini et al. (2017) (e) Ikonos satellite image © CRISP, NUS (2007) of the Lusi mud volcano and the nearby buried city in Sidoarjo, Indonesia, May 2007.

within a mudstone will dissipate slowly and, as a result, mudstones are often highly pressurised. This tendency for pressure build-up in low-permeability rocks is generally

thought to be connected to the formation of fluid-escape pipes, as pipes typically source fluids from highly pressurised rocks. Indeed, drilling in a region of active venting has revealed near-lithostatic pore pressures (Reilly & Flemings 2010). The above reasoning is frequently used to support the hypothesis that pipes are formed by hydraulic fracturing. Hydraulic fractures open when pore pressures exceed the stresses that hold the overlying rock together. While there is a lack of direct evidence from *in-situ* pipes, field observations of relict pipes (e.g., Figure 1.1c) consistently show evidence of fracturing (Huuse et al. 2005, Roberts et al. 2010, Løseth et al. 2011).

Offshore, fluid-escape pipes typically terminate at the seafloor either as pockmarks (Figure 1.1a,d) or as edifices (Figure 1.1b). Such edifices are commonly built with extruded sediment from the subsurface, in which case the pipe feeding the edifice is a conduit for a sedimentary volcano. Mud volcanoes, for example, expel a slurry of remobilised mud sourced from subsurface mudstones. Mud volcanoes are capable of continuously expelling mud at rates of $\sim 10^5$ m^3/day, as measured at the Lusi mud volcano, where the resulting mud flow has buried twelve nearby villages (Tingay 2010, see also Figure 1.1e). Such measurements are a direct consequence of the remobilisation of mud at depth. However, the mechanism by which mud is remobilised remains poorly understood, as the source of mud in mud-volcanic systems is rarely exposed at surface. Thus, our understanding of the source regions of mud volcanoes has mainly relied on indirect inferences made from surface measurements or, more recently, by direct observation of relict source regions with seismic imaging.

Seismic imaging of fluid vents has documented repeated fluid venting from a fixed locus in a subset of cases (Deville et al. 2010, Andresen & Huuse 2011, Cartwright et al. 2018, Oppo et al. 2021, Kirkham et al. 2022). In each of these cases, venting occurs in discrete episodes separated by long quiescent periods. During quiescence, the fractures comprising the venting conduit heal by solid creep, swelling and mineral precipitation

(Bock et al. 2010, Chen et al. 2013). Hence, each venting episode initiates with the formation of new hydraulic fractures. It follows that episodic venting requires the repeated recharge of pressure to the original point of failure, implying that the mechanism of pressurisation remains active across venting episodes. Sedimentary basins can be pressurised by various mechanisms (Osborne & Swarbrick 1997), including sedimentation. Evidence of episodic venting behaviour is best illustrated by seismic images from offshore Trinidad (Figure 1.1b), which show vertically stacked mud edifices formed by repeated episodes of mud expulsion contemporaneous with sedimentation. However, the dominant controls on the frequency of episodic venting have remained uncertain due to a previous lack of observational evidence.

The spatial distribution of fluid vents in sedimentary basins sheds additional light on the dynamics of venting. The majority of documented fluid-escape pipes occur in clusters (Cartwright & Santamarina 2015), often correlated with topographic highs (Oppo et al. 2021) and can align with features such as faults and underlying sandstone channels (Gay et al. 2006a,b). Furthermore, Moss & Cartwright (2010) showed that for pipes in the Namibe Basin, offshore Namibia, new pipes tend to form far from nearby active (or recently active) pipes. They hypothesise that this is a result of hydraulic connectivity between the fluid sources of these vents, though additional observational constraints are required to support this hypothesis.

Recent, high-resolution 3-D seismic observations of a wide variety of venting phenomena from across the Eastern Mediterranean provide crucial constraints on the fundamental physical processes that control venting (Figure 1.2). The majority of sedimentary basins in the Eastern Mediterranean comprise a kilometres-thick clastic succession overlain by a $\sim$1.5 km-thick layer of impermeable salt. This salt layer enables large overpressures to accumulate in the clastic succession by preventing pressure dissipation via vertical fluid flow. Thus, fluid-escape pipes and mud volcanoes typically form from

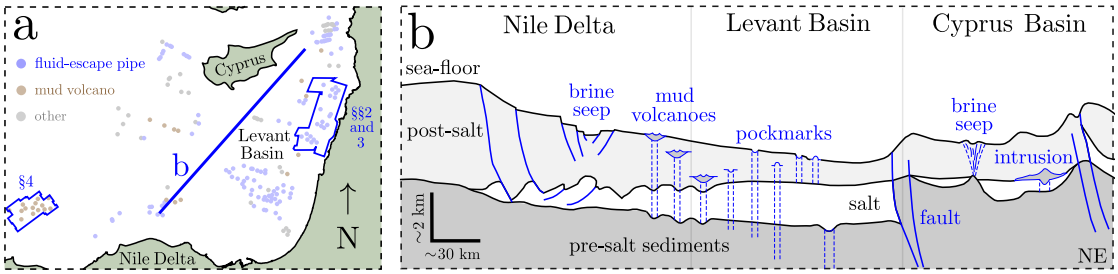

Figure 1.2: Overview of observations of fluid venting phenomena in the Eastern Mediterranean. (a) Map of the Eastern Mediterranean, showing documented evidence of venting (compiled from Bertoni et al. (2017), Oppo et al. (2021) and Cartwright et al. (2023)), the study area used in §§2 and 3 of this work, and the study area used in §4. (b) Summary diagram illustrating the variety of venting phenomena observed in the three main sub-basins of the Eastern Mediterranean across a representative cross-section, adapted from Bertoni et al. (2017). The scale indicated is only a rough guide.

this clastic succession, penetrate through the salt and terminate at the seafloor (Figure 1.2b). This simple structure is in contrast to venting phenomena from many other regions, which commonly source fluids and sediment from multiple stratigraphic layers (Planke et al. 2003, Davies et al. 2011, Deville et al. 2010). An understanding of venting in these complex systems is facilitated by the study of simple systems like the Eastern Mediterranean, which allows for broad applicability.

In the North Levant Basin (Figure 1.2a), more than 300 fluid-escape pipes have been documented by seismic data, recording trails of episodic fluid vents originating from 13 fixed locations across the region. Each pipe forms vertically but the viscous flow of salt advects existing pipes away from their initial positions, such that subsequent venting from the same location requires the formation of a replacement pipe. Repetition of this process leads to a linear trail of sea-floor pockmarks at each of the 13 venting locations. From the lateral spacings of these pockmarks, the time of formation of each pipe can be estimated, revealing that for each trail, pipe formation typically occurs every ∼100 kyr. These observations provide an unprecedented opportunity to distinguish between hypotheses of fluid venting. More broadly, since fluid-escape pipes record critical subsurface pressures,

the Levant pipe trails enable us to distinguish between hypotheses for the long-term pressure dynamics of sedimentary basins. Furthermore, the Levant fluid-escape pipes are spatially clustered, correlated with the crests of folded sandstone reservoirs (Oppo et al. 2021). Many pipes originate from the same fold and thus may be hydraulically connected. Therefore, the time-transformed venting observations will enable analysis of the spatiotemporal controls on episodic venting.

Finally, a recent high-resolution 3D seismic survey in the Nile Deep Sea Fan provides statistically robust observations of the plumbing systems of hundreds of mud volcanoes (Cartwright et al. 2023). In particular, this seismic data reveals that the expulsion of subsurface sediment by mud volcanoes leads to localised thinning of the mudstone source; these regions of localised thinning are known as mud-depletion zones. These mud-depletion zones are consistently bowl-shaped with a squat aspect ratio, with 340 ± 150 m reliefs and 790 ± 240 m radii. However, no existing quantitative theory exists that can explain the observed morphometrics of these depletion zones.

1.2 Key questions

These observations raise several important questions, particularly the following:

1. What are the fundamental physical processes that control the dynamics of fluid venting?
2. What governs the episodicity and spatial clustering of fluid-escape pipes?
3. What is the mechanism, material prerequisite and driver of sediment remobilisation during venting?
4. What physical factors determine the volume of sediment extruded over the lifetime of a mud volcano?

To address these questions, observations of fluid venting phenomena provide empirical data for the testing of related hypotheses. For hypothesis testing, mechanical models can provide a simplified and manipulable representation of physical systems like fluid vents. In particular, continuum mechanics provides a rigorous theoretical framework for analysing these systems based on established constitutive models. I thus propose an overarching hypothesis, that fluid venting phenomena can be explained in the context of a minimal continuum mechanical theory that accounts for the key processes involved.

1.3 Constitutive models of sedimentary rocks

Sedimentary rocks are formed by the deposition and compaction of mineral and organic matter. The most common sedimentary rock types are sandstones and mudstones, where sandstones consist predominantly of silicate grains (Figure 1.3a) and mudstones consist predominantly of clay grains (Figure 1.3b). The mechanical behaviour of sedimentary rocks varies dramatically depending on their composition and their degrees of compaction and cementation. These varied mechanical behaviours arise from the intergranular forces maintaining each grain in its position. These forces resist any attempt to move the grains from their equilibrium positions and typically give rise to the macroscopic elastic behaviour of rocks. The strength of these intergranular forces can be quantified by measuring the fractional change in volume of the solid per unit applied stress, i.e., the compressibility of the solid. The compressibility of a sedimentary rock depends on the degree of compaction and cementation of the rock. However, neither compaction nor cementation change significantly during fluid venting. Therefore for models of fluid venting, it is reasonable to assume that rock compressibilities remain constant.

Subsurface rocks are filled with cracks and pores that are saturated with one or more fluid phases (e.g., water or gas). These pore fluids flow through rocks towards regions

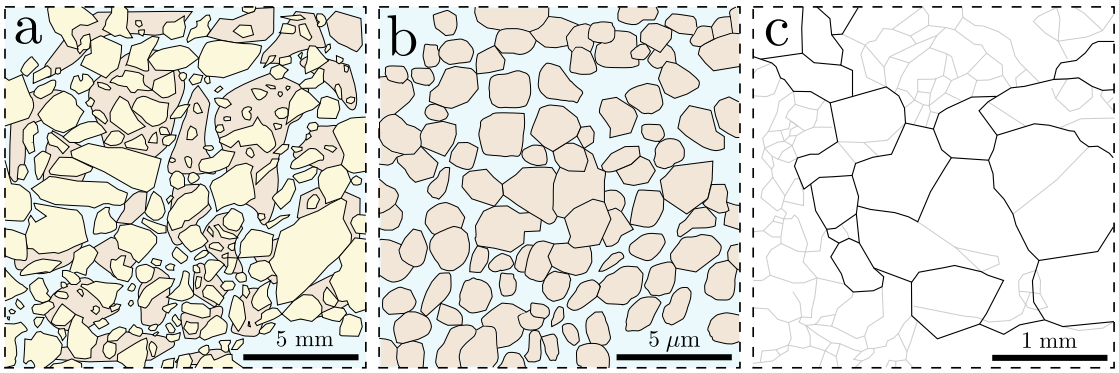

Figure 1.3: Typical microstructures of various sedimentary rocks. (a) Sandstone deposited by a turbidity current, composed of poorly sorted and angular silicate grains (yellow) supported by a mud matrix (brown, see (b)). The pore space is filled with brine (blue). Turbiditic sandstones are common in the Eastern Mediterranean. (b) Mudstone, composed of fine and well-sorted clay grains (brown). (c) Salt, a crystalline rock with a usual effective porosity of less than 1%. Strain-free salt grains (boundaries in black) have formed from strained subgrains (boundaries in grey) by dissolution and precipitation.

of low pore pressure, according to Darcy's law. The mobility of these pore fluids is determined by the viscosity of the fluids and the permeability of the rock. Permeability is a measure of the conductivity of a porous material to fluid flow. Permeability scales with the square of the grain size, as smaller grains tend to constrict flow through smaller pores. For a given grain size, rocks with larger proportions of pore space, i.e., larger porosities, are typically more permeable. However, changes in porosity caused by fluid flow generally tend to be small and thus during venting it is reasonable to assume that permeability remains constant during flow.

Despite only causing small deformations, pore fluids can still have a major influence on the mechanical behaviour of a rock mass. The mechanical deformation of a rock is therefore coupled to the pore fluid pressure. Porous flow is not only driven by pressure gradients, it is also driven by changes in stress from, for example, tectonic forces. Hence, the mechanical and hydrological behavior of rocks is fully coupled. This is especially true for compressible pore fluids such as gas, which expand and exsolve in response to decreases in pore pressure and stress. Exsolved gas bubbles can coalesce to form a

connected and mobile phase above a critical saturation. However, capillary forces can prevent the segregation (i.e., differential motion) of bubbles from the resident brine and thus prevent coalescence. The strength of capillary forces scales inversely with grain size. Therefore in fine-grained rocks like mudstones, bubble segregation is generally assumed to be negligible.

The presence of pore fluids may promote the brittle failure of a rock by fracturing. Rocks typically contain preexisting microscopic cracks which can act as nucleation sites for failure. These cracks propagate when the effective stress (i.e., the stress that is associated with deformation of the rock) exceeds the strength of the rock, leading to fracturing. Elevated pore fluid pressures reduce the strength of the rock and thus can induce fracturing under lower stresses. Rock failure is not limited to fracturing; the porous flow of fluids of a sufficient velocity can also induce the failure of a rock by fluidisation. Fluidisation occurs when the drag exerted by the pore fluid on the solid exceeds the intergranular forces (e.g., friction and cohesion) and body forces (e.g., gravity) that resist the motion of grains. Therefore, fluidisation commonly occurs in materials with weak intergranular forces (Geldart 1973); this is typical for poorly consolidated rocks. Once the intergranular forces are overcome, the solid grains are free to flow in suspension with the fluid and thus the rock is remobilised and exhibits behaviour that is similar to that of a viscous fluid.

However, fluidisation is not required for rocks to behave viscously. While rocks initially deform elastically in response to a differential stress, sustained stress over a long timescale causes gradual deformation, or 'creep', manifesting macroscopically as slow, viscous flow. This time-dependent rheology is known as viscoelasticity. One notable geological example of this rheology is rock salt. Salt is a crystalline rock which, depending on stress, deforms by either the movement of dislocations (i.e., irregularities in the crystal structure) or by the movement of grain boundaries by dissolution and precipitation

(Figure 1.3c). These deformation mechanisms enable salt to undergo large strains and produce striking geological structures such as domes, diapirs and glaciers. The viscoelastic behaviour of salt is critical in understanding the long-term stability and deformation of salt structures, especially for engineering applications such as subsurface storage and sequestration.

1.4 Thesis structure

In this chapter, I have highlighted the necessity of models describing fluid venting to better understand the pressure dynamics of sedimentary basins. It is crucial for such models to have a basis in material properties to ensure that the predictions deriving from them are accurate. In the remainder of this thesis, I develop a general theory of fluid venting from sedimentary basins and test it against observations of venting from the Eastern Mediterranean.

In Chapter 2, I develop a poroelastic theory of episodic fluid venting driven by tectonic compression. I explore the combined role of compression and fluid flow between sedimentary layers in episodic venting. In particular, I examine how these mechanisms set the resulting frequency of venting. I consider the properties of each sedimentary layer and evaluate their influences on the relative contributions of compression and fluid flow to venting. I conclude this chapter by considering typical layer properties in sedimentary basins that host fluid vents. This chapter has been published as:

> Kearney, L. M., MacMinn, C. W., Katz, R. F., Kirkham, C. & Cartwright, J. (2023), 'Episodic, compression-driven fluid venting in layered sedimentary basins', *Proceedings of the Royal Society A: Mathematical, Physical and Engineering Sciences* **479**(2274), 20220654. (doi:10.1098/rspa.2022.0654).

In Chapter 3, I compare the predictions of the theory derived in Chapter 2 with ob-

servations of episodic fluid venting from the Levant Basin, Eastern Mediterranean. I do so by constructing a stochastic model of pressure evolution during fluid venting. Using this stochastic model, I infer the rates of pressure recharge between venting episodes in the Levant Basin. Additionally, I infer the hydraulic connectivity of spatially clustered vents. I quantify and compare a range of candidate mechanisms of pressure recharge to determine whether fluid flow from mudstone layers provides the most plausible explanation for these observations. This chapter has been published as:

> Kearney, L. M., Katz, R. F., MacMinn, C. W., Kirkham, C. & Cartwright, J. (2024), 'Episodic fluid venting from sedimentary basins fueled by pressurized mudstones', *Proceedings of the National Academy of Sciences* **121**(8), e2312152121. (doi:10.1073/pnas.2312152121).

In Chapter 4, I develop a novel theory of mud volcano eruptions, whereby rapid fluid expulsion drives mudstone remobilisation. I examine the dynamics of this process of remobilisation, known as fluidisation, and the growth of a region of fluidised mud. I consider the parameters that govern these dynamics and the final size of the fluidised region. Using estimates of mudstone properties, I test if the predictions of this theory are consistent with observations of mud volcanoes from the Nile Deep Sea Fan, Eastern Mediterranean. This chapter is as yet unpublished.

Finally, in Chapter 5, I summarise my findings and highlight promising directions for future work.

Chapter 2

Episodic, compression-driven fluid venting

The theoretical model, results and analysis presented in this chapter have been published in Kearney et al. (2023). This chapter constitutes a minor reformatting of that work to fit within the context of this thesis.

2.1 Introduction

Fluid venting phenomena have been frequently observed in sedimentary basins since the advent of 3D seismic imaging (Løseth et al. 2001, Hovland & Judd 1988). The vents themselves are localised, typically comprising cylindrical conduits known as fluid-escape pipes that can create pockmarks or feed effusive mud volcanoes (Huuse et al. 2010, Cartwright & Santamarina 2015). Venting is thought to initiate when the seal of a pressurised reservoir fails through hydraulic fracturing (Huuse et al. 2005, Roberts et al. 2010, Løseth et al. 2011), creating a high-permeability pathway for the transport of basinal fluids through kilometres of low-permeability rock (Cartwright et al. 2021). This mode of seal failure poses clear risks for the subsurface storage of hydrogen and the long-term sequestration of anthropogenic waste such as carbon dioxide (CO_2). Indeed,

unexpected vertical fluid migration at the Sleipner CO_2 storage pilot site is likely due to exploitation of pre-existing conduits (Arts et al. 2004, Cavanagh & Haszeldine 2014).

Repeated fluid venting from a fixed locus has been documented in a subset of cases (Deville et al. 2010, Andresen & Huuse 2011, Cartwright et al. 2018, Oppo et al. 2021, Kirkham et al. 2022). In each of these cases, venting occurs in discrete episodes of fluid expulsion separated by long quiescent periods. In the North Levant Basin, located in the Eastern Mediterranean, the presence of a flowing salt sheet enables dating of individual venting episodes (Oppo et al. 2021, Evans et al. 2020, Cartwright et al. 2021), thus providing a robust basis for investigating episodic fluid venting. More than 300 fluid escape pipes record episodic venting through this ∼1.5 km-thick layer of low-permeability salt. The salt overlies a ∼3 km-thick clastic succession dominated by mudstone. These fluid-escape pipes are interpreted to form vertically from the crests of folded sandstone reservoirs, terminating at the seafloor as pockmarks. Viscous flow of the salt layer deforms the relic pipes over geological time, such that repeated venting leads to a linear trail of pockmarks along the direction of salt flow (Cartwright et al. 2018). Thirteen pockmark trails have been observed across the North Levant Basin, each recording up to 45 venting episodes since ∼2 Ma (Oppo et al. 2021). Dating of these venting episodes reveals a typical time interval between episodes (i.e., venting period) of ∼100 kyr (Oppo et al. 2021, Evans et al. 2020, Cartwright et al. 2021).

The initiation of a vent via hydraulic fracturing requires fluid pressure in excess of the minimum horizontal compressive stress (Price & Cosgrove 1990, Scandella et al. 2011). Once initiated, venting continues until this overpressure is sufficiently relieved that the pathway closes. Subsequently, during quiescence, fractures may self-heal by solid creep, swelling, and mineral precipitation (Bock et al. 2010, Chen et al. 2013). In the North Levant Basin, previous pathways are deformed and advected away from their original trajectory by salt flow. Hence, episodic venting requires the repeated recharge of

overpressure to the original point of failure, implying that the overpressure mechanism remains active across venting episodes. The disparity between the rapid drop in pressure during venting and the slow growth of pressure during recharge suggests that the time-history of reservoir pressure across multiple episodes resembles a sawtooth pattern, with the up-slope representing the rate of pressure recharge and the amplitude representing the pressure drop during venting (Cartwright et al. 2021). Cartwright et al. (2021) take this pressure drop to be equal to the tensile strength of the sealing rock, estimated to range from 0.6 to 2 MPa. Using the sawtooth concept and the measured period between venting episodes, Cartwright et al. (2021) inferred a rate of pressure recharge in the North Levant Basin of ∼9 MPa/Myr.

Overpressure can be generated by various mechanisms (Osborne & Swarbrick 1997). For the Levant basin, Cartwright et al. (2021) ascribe overpressure generation to regional tectonic compression on the basis of qualitative physical arguments. Previous studies have used numerical models to predict overpressures due to tectonic compression and quantify the role of factors such as duration and rate of shortening (Luo 2004, Obradors-Prats et al. 2017*a*,*b*, Maghous et al. 2014). For example, Obradors-Prats et al. (2017*a*) showed that an overpressure of ∼10 MPa can be generated by a shortening of ∼10% over a period of ∼100 kyr. However, overpressure will typically be heterogeneously distributed throughout the sedimentary column. Ge & Garven (1992) showed that tectonic compression pressurises stratigraphic layers at different rates due to their different elastic properties. These pressure differences equilibrate over time through vertical fluid redistribution, which can be described mathematically as the diffusion of pressure.

Pressure diffusion between sedimentary layers has been investigated in many previous works (e.g., Muggeridge et al. 2004, 2005, and refs. therein). The primary concern of these studies has been to estimate the timescales and mechanisms of pressure redistribution through low-permeability layers. As a result, these studies typically focus on the

diffusive equilibration of an initially non-hydrostatic pressure distribution while neglecting the origin of that distribution or any ongoing sources of overpressure generation. This omission may not always be justified, given that mechanisms such as tectonic compression persist for millions of years and are physically independent of pressure redistribution. Moreover, these studies generally neglect punctuated effects that modify the pressure, such as venting. An exception is Luo & Vasseur (2016), who investigated mechanisms of pressure dissipation including hydraulic fracturing.

Despite the large body of relevant work, most previous studies have neglected at least one of the three key components of episodic venting: pressure build-up, pressure diffusion, and hydraulic fracturing. The studies that include all three components predict episodic venting. However, these models incorporate a variety of additional physics such as reaction and heat transport, necessitating numerical solution (Dewers & Ortoleva 1994, L'Heureux & Fowler 2000). The complexity and computational expense of these models limits them to generating a small set of results for a specific setting, making it difficult to develop more general insight. Such insight is facilitated by a simplified theory that incorporates only the physical processes needed to describe the general, episodic dynamics of fluid venting in sedimentary basins. Moreover, measurements of the venting period are readily interpreted in this analytical context.

Here we develop a poroelastic model of tectonic overpressure generation, diffusive pressure redistribution, and fluid venting in layered sedimentary basins. We derive analytical solutions that elucidate the associated pressure dynamics and the parametric controls on venting. We show in particular that the venting period τ is given by $\tau \propto (\Delta P/\dot{e}_{xx})/(1+\nu/\gamma)$, where ΔP is the pressure drop from each venting event, $\dot{e}_{xx}$ is the horizontal strain rate due to tectonic compression and ν and γ are dimensionless parameters that are defined below. The quantity $\Delta P/\dot{e}_{xx}$ is proportional to the venting period in the absence of pressure diffusion, as estimated by Cartwright et al. (2021).

The dimensionless quantity $(1 + \nu/\gamma)$ incorporates the additional role of pressure diffusion from mudstones. We refer to this quantity as the *venting frequency multiplier* because it reduces the venting period relative to the compression-only case. We show that this frequency multiplier can be estimated using the thickness ratio of the mudstone and sandstone layers. In mudstone-dominated basins where fluid venting phenomena are commonly observed (Cartwright & Santamarina 2015), pressure recharge and venting period are controlled by pressure diffusion.

The remainder of this chapter is organised as follows. In §2.2.1, we derive and solve the poroelastic equations governing tectonic compression of, and pressure diffusion between, sedimentary layers in the absence of fluid venting. In §2.2.2, we explore the response of the system to fluid venting without compression. In §2.2.3, we combine solutions from §2.2.1 and §2.2.2 to obtain a full model for episodic venting; we then derive analytical solutions for periodic venting. In §2.3, we discuss the wider implications of this work, as well as limitations and potential generalisations of the model. In §2.4, we conclude with a summary and suggestions for promising avenues of future work.

2.2 Model

2.2.1 Compression

We consider two horizontal layers of rock, a sandstone with thickness h_s overlying a mudstone with thickness h_m, as illustrated in Figure 2.1a. To focus on large-scale pressurisation from regional tectonic compression, we assume that these layers have a large lateral extent, such that pressure diffusion occurs exclusively through vertical fluid migration. The development of large overpressure from tectonic compression thus requires that compression be rapid relative to pressure diffusion and/or that vertical flow be ob-

structed.

Sedimentary basins are typically underlain by dense basement rock, so we assume the existence of an impermeable layer below the mudstone. Furthermore, motivated by sedimentary basins such as the Levant basin that are capped with an extensive, thick salt layer, we apply the same assumption above the sandstone. Salt is considered to be impermeable on geological timescales (though see Ghanbarzadeh et al. 2015). This model configuration prohibits vertical pressure diffusion across the salt, but allows for sudden fluid expulsion via hydraulic fracturing. The theory below could be generalised to allow for a 'seal' with a small but nonzero permeability.

As in previous studies that consider pressure diffusion between sedimentary layers, we assume that flow is single-phase, isothermal and one-dimensional (Bredehoeft & Hanshaw 1968, Neuzil 1986, Luo & Vasseur 1997, Muggeridge et al. 2004). Crucially, we deviate from these previous studies by modelling the evolution of pressure due to ongoing (rather than historical) tectonic compression. Tectonic compression has been conceptualised as a bulldozer imparting sufficient differential stress to deform weaker sediments (Byrne et al. 1993). It has been modelled mathematically as an imposed, constant horizontal

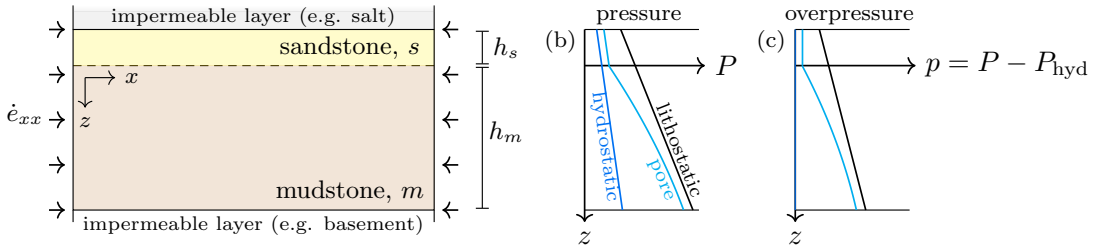

Figure 2.1: Schematic cross-section of sedimentary-basin model. (a) We consider the tectonic compression of two permeable sedimentary layers, sandstone (yellow) and mudstone (brown), at a constant horizontal strain rate $-\dot{e}_{xx}$. The system is sealed by impermeable layers above the sandstone and below the mudstone. (b) Example pressure–depth plot showing the hydrostatic pressure (blue), pore pressure resulting from compression (cyan) and lithostatic stress (black). (c) As in (b), but now showing the lithostatic stress in excess of hydrostatic (black) and the pore overpressure p (cyan), which is the pressure in excess of hydrostatic P_{hyd}.

strain rate $-\dot{e}_{xx}$, where $\dot{e}_{xx} > 0$ indicates compression; strain rates are routinely used to quantify tectonic deformation (e.g. Kahle et al. 1998, Kreemer et al. 2014). In the absence of venting, tectonic shortening is accommodated through compression of the pore fluid and/or of the solid grains. We refer to this specific process as tectonic compression.

Assuming that the solid skeleton obeys linear elasticity and taking tension to be positive, the effective stress tensor $\boldsymbol{\sigma}'$ is related to the strain tensor $\boldsymbol{e}$ via

$$\boldsymbol{\sigma}' = \lambda \mathrm{tr}\,(\boldsymbol{e})\,\mathbf{I} + 2\mu\boldsymbol{e}, \tag{2.1}$$

where λ and μ are the drained Lamé parameters and $\boldsymbol{e} \equiv \frac{1}{2}[\boldsymbol{\nabla u} + (\boldsymbol{\nabla u})^{\mathrm{T}}]$ with $\boldsymbol{u}$ denoting the solid displacement. The effective stress is related to the total stress $\boldsymbol{\sigma}$ and pore pressure P by Terzaghi's principle,

$$\boldsymbol{\sigma} = \boldsymbol{\sigma}' - \alpha P\mathbf{I}, \tag{2.2}$$

where α is Biot's coefficient and where we adopt the sign convention that tension is positive. Mass conservation leads to the storage equation (Verruijt 1969, see Appendix 2.A), which is equivalent to the classical continuity equation presented by Biot (1941),

$$\alpha\frac{\partial e}{\partial t} + S\frac{\partial P}{\partial t} = -\boldsymbol{\nabla}\cdot\boldsymbol{q}, \tag{2.3}$$

where $e \equiv \mathrm{tr}\,(\boldsymbol{e})$ is the volumetric strain, $\boldsymbol{q}$ is the Darcy flux of fluid through the pore space and $S \equiv \phi c_\ell + (\alpha - \phi)c_g$ is the storativity, with porosity ϕ, fluid compressibility c_ℓ and grain compressibility c_g. The time derivative of the xx-component of Equation (2.1) implies that

$$\frac{\partial \sigma'_{xx}}{\partial t} = \lambda\frac{\partial e}{\partial t} - 2\mu\dot{e}_{xx}, \tag{2.4}$$

and the trace of Equation (2.1) implies that $(3\lambda + 2\mu)\,e = \mathrm{tr}\,(\boldsymbol{\sigma}')$. From these results

and Equation (2.2), we arrive at

$$\frac{\partial P}{\partial t} = \frac{\lambda + \mu}{\alpha}\frac{\partial e}{\partial t} + \frac{\mu}{\alpha}\dot{e}_{xx} - \frac{1}{2\alpha}\left(\frac{\partial \sigma_{yy}}{\partial t} + \frac{\partial \sigma_{zz}}{\partial t}\right). \tag{2.5}$$

Equation (2.5) describes the evolution of pore pressure in response to changes in strain and total stress. The total vertical stress at a fixed depth can increase ($\partial_t \sigma_{zz} < 0$) in response to folding and thrust faulting, which are a commonly a consequence of tectonic shortening (e.g., the Levant Basin, see Oppo et al. 2021). Furthermore, the height of the rock column will increase, thus increasing the vertical stress and hydrostatic pressure. However, we are primarily focused on studying tectonic shortening in the absence of these secondary processes, so we assume that $\partial_t \sigma_{zz} = 0$. The evolution of the total horizontal stress in the orthogonal direction, $\partial_t \sigma_{yy}$ is less clear. Two endmember assumptions are that the orthogonal total stress remains constant ($\partial_t \sigma_{yy} = 0$), or that the associated strain remains constant ($\partial_t e_{yy} = 0$). The former unconditionally allows for hydraulic fracturing, whereas the latter may not in some cases (Appendix 2.B). For simplicity, we proceed with the former assumption and take σ_{yy} to be constant. Combining these assumptions with Eqs. (2.3) and (2.5) gives

$$\frac{\partial P}{\partial t} = \frac{\alpha\mu\dot{e}_{xx}}{\alpha^2 + S(\lambda + \mu)} - \frac{\lambda + \mu}{\alpha^2 + S(\lambda + \mu)}\boldsymbol{\nabla} \cdot \boldsymbol{q}. \tag{2.6}$$

Thus, two processes drive changes in pore pressure: compression and fluid flow. The first term in Eq. (2.6) corresponds to compression, which acts to increase pressure everywhere at a rate determined by the compression rate and the poroelastic properties of the medium. The second term in Eq. (2.6) demonstrates that pressure increase at a point is impeded by a net export of fluid ($\boldsymbol{\nabla} \cdot \boldsymbol{q} > 0$) or enhanced by a net import ($\boldsymbol{\nabla} \cdot \boldsymbol{q} < 0$).

For a system that is both laterally extensive and laterally homogeneous (i.e., no variations in x or y; Fig. 2.1), fluid flow is limited to the vertical direction, $\boldsymbol{q} \equiv q\,\hat{\mathbf{z}}$.

Then, applying Eq. (2.6) to each layer,

$$\frac{\partial P_s}{\partial t} = \frac{\alpha_s \mu_s \dot{e}_{xx}}{\alpha_s^2 + S_s(\lambda_s + \mu_s)} - \frac{\lambda_s + \mu_s}{\alpha_s^2 + S_s(\lambda_s + \mu_s)} \frac{\partial q}{\partial z} \quad \text{for } z \in [-h_s, 0], \tag{2.7a}$$

$$\frac{\partial P_m}{\partial t} = \frac{\alpha_m \mu_m \dot{e}_{xx}}{\alpha_m^2 + S_m(\lambda_m + \mu_m)} - \frac{\lambda_m + \mu_m}{\alpha_m^2 + S_m(\lambda_m + \mu_m)} \frac{\partial q}{\partial z} \quad \text{for } z \in [0, h_m]. \tag{2.7b}$$

where the subscripts s and m represent properties of the sandstone and of the mudstone, respectively.

Sandstones typically have permeabilities that are many orders of magnitude larger than those of mudstones. Consequently, pressure diffuses much faster in sandstone than in mudstone. Hence over timescales of pressure diffusion in the mudstone, the overpressure in the sandstone can be taken to be vertically uniform. From this assumption, the only relevant fluid flux within the sandstone occurs at the contact with the mudstone,

$$\frac{\mathrm{d}P_s}{\mathrm{d}t} = \frac{\alpha_s \mu_s \dot{e}_{xx}}{\alpha_s^2 + S_s(\lambda_s + \mu_s)} - \frac{\lambda_s + \mu_s}{\alpha_s^2 + S_s(\lambda_s + \mu_s)} \frac{q(0,t)}{h_s}. \tag{2.8}$$

Fluid transport in the mudstone is governed by Darcy's law,

$$q = -\frac{k_m}{\eta}\left(\frac{\partial P_m}{\partial z} - \rho_\ell g\right), \tag{2.9}$$

where η is the viscosity of the fluid and k_m is the permeability of the mudstone, both assumed to be constant. Equations (2.7a), (2.8) and (2.9) combine to form a coupled system for the pressure of each layer,

$$\frac{\mathrm{d}P_s}{\mathrm{d}t} = \frac{\alpha_s \mu_s \dot{e}_{xx}}{\alpha_s^2 + S_s(\lambda_s + \mu_s)} + \frac{\lambda_s + \mu_s}{\alpha_s^2 + S_s(\lambda_s + \mu_s)} \frac{1}{h_s} \frac{k_m}{\eta} \frac{\partial P_m}{\partial z}\bigg|_{z=0} \quad \text{for } z \in [-h_s, 0], \tag{2.10a}$$

$$\frac{\partial P_m}{\partial t} = \frac{\alpha_m \mu_m \dot{e}_{xx}}{\alpha_m^2 + S_m(\lambda_m + \mu_m)} + \frac{\lambda_m + \mu_m}{\alpha_m^2 + S_m(\lambda_m + \mu_m)} \frac{k_m}{\eta} \frac{\partial^2 P_m}{\partial z^2} \quad \text{for } z \in [0, h_m]. \tag{2.10b}$$

In this system, the hydrostatic contribution to the pressure remains constant. It has no effect on the dynamics and hence we replace total pressure P with overpressure p. The overpressure is the pressure in excess of hydrostatic, $p \equiv P - P_{\text{hyd}}$ (see Fig. 2.1b,c),

$$\frac{\mathrm{d}p_s}{\mathrm{d}t} = \frac{\alpha_s \mu_s \dot{e}_{xx}}{\alpha_s^2 + S_s(\lambda_s + \mu_s)} + \frac{\lambda_s + \mu_s}{\alpha_s^2 + S_s(\lambda_s + \mu_s)} \frac{1}{h_s} \frac{k_m}{\eta} \frac{\partial p_m}{\partial z}\bigg|_{z=0} \quad \text{for } z \in [-h_s, 0], \tag{2.11a}$$

$$\frac{\partial p_m}{\partial t} = \frac{\alpha_m \mu_m \dot{e}_{xx}}{\alpha_m^2 + S_m(\lambda_m + \mu_m)} + \frac{\lambda_m + \mu_m}{\alpha_m^2 + S_m(\lambda_m + \mu_m)} \frac{k_m}{\eta} \frac{\partial^2 p_m}{\partial z^2} \quad \text{for } z \in [0, h_m]. \tag{2.11b}$$

Equation (2.11a) is an ordinary differential equation for the time-evolution of the pressure in the sandstone. Equation (2.11b) is a partial differential equation for the pressure in the mudstone in depth and time. The latter requires two boundary conditions. The first boundary condition is that the sandstone and mudstone pressures must match at the contact, $p_m(0, t) = p_s$. The second boundary condition is that there is no fluid flux through the impermeable layer at the bottom of the mudstone $\partial p_m / \partial z|_{h_m} = 0$. Equations (2.11) are simplified by introducing the following parameters,

$$D_m = \frac{k_m}{\eta} \frac{\lambda_m + \mu_m}{\alpha_m^2 + S_m(\lambda_m + \mu_m)}, \qquad D_s = \frac{k_m}{\eta} \frac{\lambda_s + \mu_s}{\alpha_s^2 + S_s(\lambda_s + \mu_s)}, \tag{2.12}$$

$$\Gamma_m = \frac{\alpha_m \mu_m \dot{e}_{xx}}{\alpha_m^2 + S_m(\lambda_m + \mu_m)}, \qquad \Gamma_s = \frac{\alpha_s \mu_s \dot{e}_{xx}}{\alpha_s^2 + S_s(\lambda_s + \mu_s)}, \tag{2.13}$$

The parameters Γ_m and Γ_s represent the rates of pressure build-up in the mudstone and sandstone layers, respectively, due to compression. The parameter D_m represents the diffusivity of pressure across the mudstone whereas the parameter D_s represents the diffusivity of pressure across the sandstone–mudstone boundary. The full model can then be written,

$$\frac{\partial p_m}{\partial t} = \Gamma_m + D_m \frac{\partial^2 p_m}{\partial z^2} \quad \text{for } z \in [0, h_m], \tag{2.14}$$

with boundary conditions,

$$\left.\begin{aligned} \frac{\partial p_m}{\partial t} &= \Gamma_s + \frac{D_s}{h_s}\frac{\partial p_m}{\partial z} && \text{at } z = 0, \\ \frac{\partial p_m}{\partial z} &= 0 && \text{at } z = h_m, \end{aligned}\right\} \tag{2.15}$$

where $p_s = p_m(0,t)$. We finally assume that the mudstone and sandstone are initially at hydrostatic pressure,

$$p_m(z,0) = 0. \tag{2.16}$$

This initial condition is chosen for simplicity and is not essential to the model; in many circumstances, it may be more appropriate to invoke a different initial pressure distribution. Here, we are interested in the general response to tectonic compression, decoupled from the basin-specific response due to an initial pressure disequilibrium.

Nondimensionalised equations

We nondimensionalise this system of equations using mudstone properties, introducing a dimensionless depth z^*, mudstone pressure p_m^*, and time t^* defined as

$$z \equiv h_m z^*, \qquad p_m \equiv \frac{\Gamma_m h_m^2}{D_m} p_m^*, \qquad t \equiv \frac{h_m^2}{D_m} t^*. \tag{2.17}$$

Note that time is scaled by the characteristic time for a pressure perturbation to diffuse across the mudstone. This process typically requires thousands to millions of years and thus we scale time to study the pressure behaviour over these geological timescales. Pressure is scaled by the increase in mudstone pressure due to compression over this characteristic time. This formulation helps to highlight the effects of differences in layer properties on pressure behaviour. The dimensionless equation for the mudstone is then

$$\frac{\partial p_m^*}{\partial t^*} = 1 + \frac{\partial^2 p_m^*}{\partial z^{*2}} \quad \text{for } z^* \in [0,1]. \tag{2.18}$$

with boundary conditions,

$$\left.\begin{aligned} \frac{\partial p_m^*}{\partial t^*} &= \gamma + \nu \frac{\partial p_m^*}{\partial z^*} && \text{at } z^* = 0, \\ \frac{\partial p_m^*}{\partial z^*} &= 0 && \text{at } z^* = 1, \end{aligned}\right\} \tag{2.19}$$

and initial condition $p_m^*(z^*, 0) = 0$. Two dimensionless parameters γ and ν emerge to characterise the system,

$$\gamma \equiv \frac{\Gamma_s}{\Gamma_m}, \qquad \nu \equiv \frac{D_s}{D_m}\frac{h_m}{h_s}. \tag{2.20}$$

The parameter γ measures the rate of pressure build-up of the sandstone relative to that of the mudstone, which depends on the material properties of each rock type and is independent of strain rate. We refer to the parameter ν as the hydraulic capacitance ratio. The hydraulic capacitance of a layer is given by the product of compressibility and volume (or thickness, in one dimension); it measures the change in bulk volume associated with a unit change in the pressure of that layer. If the sandstone layer is thinner and less compressible than the mudstone, as would typically be expected, then the sandstone will have a lower hydraulic capacitance than the mudstone ($\nu > 1$). As a result, a transfer of fluid from the mudstone to the sandstone would lead to a pressure decrease in the mudstone and a pressure increase in the sandstone, but the increase would be larger than the decrease by a factor of ν. This asymmetry is central to our results here because it implies that a pressurised mudstone can fully recharge a sandstone that has been depressurised by venting ν times, even without further tectonic compression.

We solve the system of equations (2.18) and (2.19) via Laplace transforms (Appendix 2.C) to arrive at

$$p_m^* = t^* + 2\nu(\gamma - 1)\sum_{j=1}^{\infty} \frac{\cos\{\xi_j(1 - z^*)\}}{\cos \xi_j} \frac{1 - \exp(-\xi_j^2 t^*)}{\xi_j^2(\nu^2 + \nu + \xi_j^2)}, \tag{2.21}$$

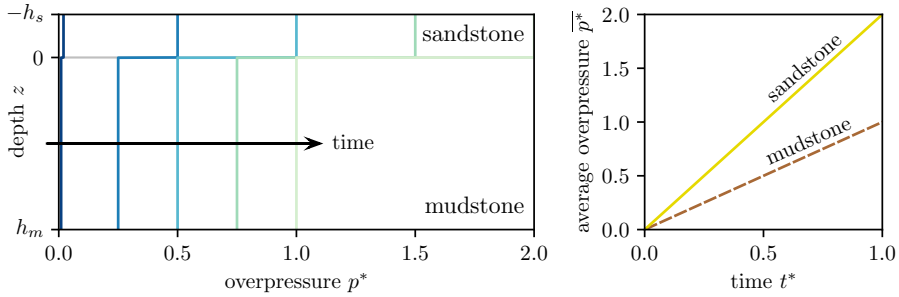

Figure 2.2: Early-time compression solution for $\gamma = 2$. Left: Overpressure versus depth at times $t^* = (0.01, 0.25, 0.5, 0.75, 1)$ (dark to light colours). Right: Time evolution of the average overpressure in the sandstone (solid yellow) and mudstone (dashed brown).

where ξ_j is the j^{th} solution to $\tan \xi_j = -\xi_j/\nu$. The first term t^* is the pressure response to the compression of the mudstone. The second term expresses pressure communication between the sandstone and mudstone. Two time-regimes emerge because compression begins to act instantaneously whereas diffusion takes effect over a characteristic timescale h_m^2/D_m. Our dimensionless time variable t^* is scaled by the latter and so diffusion becomes important for dimensionless times $t^* \sim 1$ and larger. For early times $t^* \ll 1$, diffusion is negligible and layer pressures increase independently. It can be shown that this early-time behaviour is given by (Appendix 2.C)

$$p_m^* \sim t^*, \qquad p_s^* \sim \gamma t^*, \qquad \text{for } t^* \ll 1. \tag{2.22}$$

In this limit, the mudstone pressure is uniform in space. The mudstone and sandstone pressures will rise in equilibrium if the layers have equivalent elastic properties ($\gamma = 1$). Otherwise, the two pressures will increase at different rates, diverging linearly. Fig. 2.2 illustrates this early time solution for $\gamma = 2$, meaning that the mudstone is twice as compressible as the sandstone. In this case, the sandstone pressurises twice as fast as the mudstone. Mudstones are generally expected to be more compressible than sandstones (Chang et al. 2013*b*). However, mudstones are also typically more overpressured than sandstones (Osborne & Swarbrick 1997), contrary to the model result above. This is

because sandstones typically leak some overpressure via a baffled pathway; without this leakage, the sandstone would be more overpressured during tectonic compression.

For times $t^* \sim 1$ and larger, the homogenising action of diffusion becomes increasingly important. The system evolves toward a late-time ($t^* \gg 1$) behaviour characterised by

$$p_m^* \sim \frac{\gamma+\nu}{1+\nu}t^* + \frac{\nu(\gamma-1)}{3(1+\nu)^2} - \frac{\gamma-1}{2(1+\nu)}z^*(2-z^*), \qquad p_s^* \sim \frac{\gamma+\nu}{1+\nu}t^* + \frac{\nu(\gamma-1)}{3(1+\nu)^2}. \quad (2.23)$$

In this late-time state, the sandstone pressure increases at a rate given by $(\gamma+\nu)/(1+\nu)$, which is between the independent, early-time rates of the two layers. The mudstone pressure tends toward a parabolic profile in z. If $\gamma > 1$, the mudstone pressure will be maximum at the sandstone and decrease with depth (Fig. 2.3). If $\gamma < 1$, the mudstone pressure will be minimum at the sandstone and increase with depth.

Fig. 2.3 illustrates the impact of ν on the pressure behaviour at late times, taking $\gamma = 2$ for comparison with the early-time in Fig. 2.2. Compression pressurises the sandstone more quickly than the mudstone, driving fluid from the sandstone into the mudstone. At $\nu = 5$, the sandstone is small compared to the mudstone, thus the mudstone pressure will not vary significantly from its compression-driven trajectory while the pressures equilibrate. In the opposite limit ($\nu = 0.2$), this transfer of fluid depressurises the mudstone without noticeably pressurising the sandstone. For any ν, however, both pressures grow in time and will eventually reach the minimum compressive stress (Appendix 2.B), leading to hydraulic fracturing and fluid venting. We incorporate these phenomena into the model in the next section.

2.2.2 Fluid venting

Fluid venting is assumed to occur by hydraulic fracturing. A vertical hydraulic fracture forms when the pore pressure exceeds a critical value P_f, given by the sum of the mini-

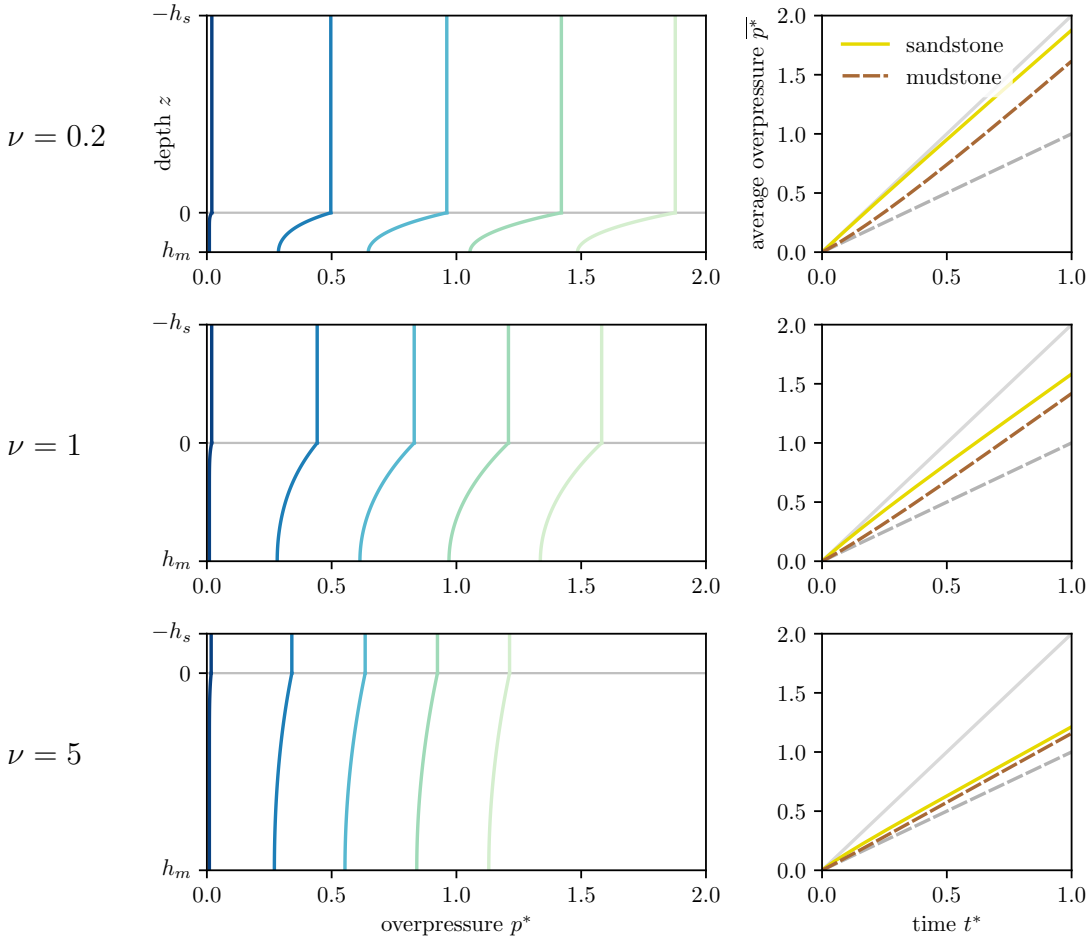

Figure 2.3: Full compression solution for $\gamma = 2$, and three different values of ν. Left: Overpressure versus depth at times $t^* = (0.01, 0.25, 0.5, 0.75, 1)$ (dark to light colours). Right: Time evolution of the average overpressure in the sandstone (solid yellow) and mudstone (dashed brown). We use ν to indicate the relative thicknesses of each layer, assuming $\nu = h_m/h_s$. We also show the corresponding early-time solutions for each layer (solid grey for sandstone, dashed grey for mudstone).

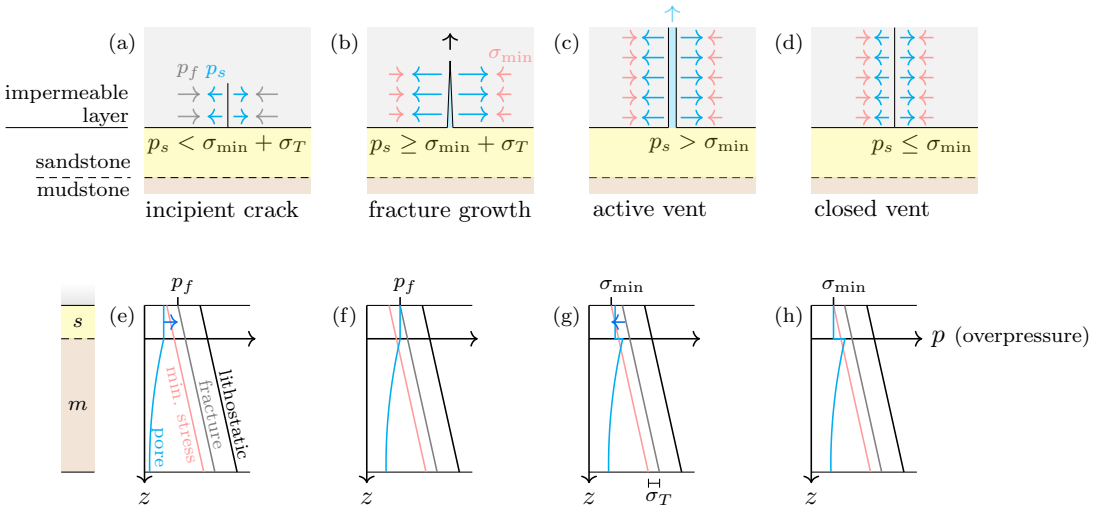

Figure 2.4: Schematic diagrams of our conceptual model for venting with corresponding overpressure–depth plots. Panels (a)–(d) are as in Fig. 2.1a, but magnified into the sandstone layer (yellow) and the overlying sealing layer (grey). (a) A microscopic incipient fracture in the sealing layer will remain closed as long as the sandstone overpressure p_s (blue arrows) is less than the critical fracture overpressure $p_f = \sigma_{\min} + \sigma_T$ (grey arrows), where $\sigma_{\min}$ here represents the minimum compressive stress minus the hydrostatic pressure. (b) Once p_s exceeds p_f, a fracture will open and grow toward the surface. The fractured rock has no tensile strength, so only $\sigma_{\min}$ acts against the fracture. (c) An active vent sources fluid from the sandstone layer and depressurises it until p_s falls back to $\sigma_{\min}$. (d) Once p_s equals $\sigma_{\min}$, the vent closes, allowing the fracture to heal. Panels (e)–(h) show overpressure–depth plots corresponding to the incipient-crack scenario in (a), the fracture-growth scenario in (b), the active-vent scenario in (c) and the closed-vent scenario in (d), respectively. (e) The pore overpressure in the sandstone p_s is less than the critical fracture overpressure at the top sandstone p_f (grey). (f) The fracture propagates and opens once p_s exceeds p_f. (g) Venting occurs until p_s falls back to $\sigma_{\min}$. (h) At which point, the vent closes.

mum horizontal compressive stress $\sigma_{\min}$ and the tensile strength σ_T of the impermeable rock (Price & Cosgrove 1990),

$$P_f = \sigma_{\min} + \sigma_T. \tag{2.24}$$

Once venting begins, the sandstone pressure drops rapidly until the fracture closes, which we assume occurs when P_s reaches $\sigma_{\min}$, giving an overall pressure drop of σ_T. Once closed, the fracture heals and may be carried away from the venting point by viscous creep of the salt. Since venting is geologically instantaneous, we incorporate venting into our model by augmenting the (nondimensional) sandstone boundary condition as follows,

$$\frac{\partial p_m^*}{\partial t^*} = -\sigma_T^* \delta(t^* - t_f^*) + \gamma + \nu \frac{\partial p_m^*}{\partial z^*} \quad \text{at } z^* = 0. \tag{2.25}$$

where $\sigma_T \equiv \sigma_T^* \Gamma_m h_m^2 / D_m$ is a dimensionless tensile strength, t_f^* is the dimensionless time when the sandstone overpressure reaches p_f^* (i.e., $p_m^*(0, t_f^*) \equiv p_f^*$), and $\delta(t^* - t_f^*)$ is the Dirac delta function. This boundary condition imposes an instantaneous drop in sandstone pressure of σ_T at time t_f^*. The solution to the modified system of equations is separable into two parts: one for compression (i.e., the solution derived above, Eq. (2.21)), and one representing the response to pipe formation. We derive the latter solution for the overpressure response to pipe formation, $\tilde{p}_m$ (dimensional), via Laplace transforms (Appendix 2.D), arriving at

$$\frac{\tilde{p}_m}{\sigma_T} = -\frac{1}{1+\nu} - 2\nu \sum_{j=1}^{\infty} \frac{\cos\{\xi_j(1-z^*)\}}{\cos \xi_j} \frac{\exp\{-\xi_j^2 (t^* - t_f^*)\}}{\nu^2 + \nu + \xi_j^2}. \tag{2.26}$$

At late times, the rightmost term vanishes as the layer pressures equilibrate by pressure diffusion. In transferring fluid to the depressurised sandstone, the mudstone pressure drops by $\sigma_T/(1+\nu)$, while the sandstone pressure rises by $\sigma_T \nu/(1+\nu)$. Increasing ν, for example by increasing the size of the mudstone relative to the sandstone, reduces

the sensitivity of the mudstone to venting from the sandstone (Fig. 2.5). An infinitely large mudstone will have a constant mean pressure in response to venting. Increasing ν also reduces the time needed for pressure equilibration because depressurisation is more localised to the mudstone–sandstone boundary.

Even in the absence of further tectonic compression, pressure diffusion from the mudstone can fully recharge the sandstone layer after venting, potentially multiple times. However, it is likely that compression continues to act once venting has initiated. In the next section, we explore the combined system for compression and venting.

2.2.3 Episodic venting

The solution for simultaneous compression and venting is obtained by superposing the two independent solutions above for compression Eq. (2.21) and Eq. (2.26). In particular, the linearity of the model allows episodic venting to be represented by a superposition of venting responses at a set of fracture times. The n^{th} fracture time $t_{f,n}$ must be determined numerically using the condition $p_m(0, t_{f,n}) = p_f$. An example scenario of continuous compression with venting is illustrated in Fig. 2.6 for $\gamma = 2$ and $\nu = 5$, in which case the mudstone is larger and more compressible than the sandstone.

Without pressure diffusion (i.e., with compression only), our model reduces to the sawtooth model proposed by Cartwright et al. (2021) (Fig. 2.6a). With pressure diffusion, our full model produces qualitatively similar sawtooth behaviour for the sandstone pressure. However, time between venting episodes (i.e., the venting period) is notably shorter because pressure diffusion from the mudstone provides an additional contribution to pressure recharge. As the mudstone pressure increases relative to the sandstone pressure, this diffusive flux into the sandstone increases and the venting period decreases. At late times, the venting period tends towards a constant as the mudstone pressure os-

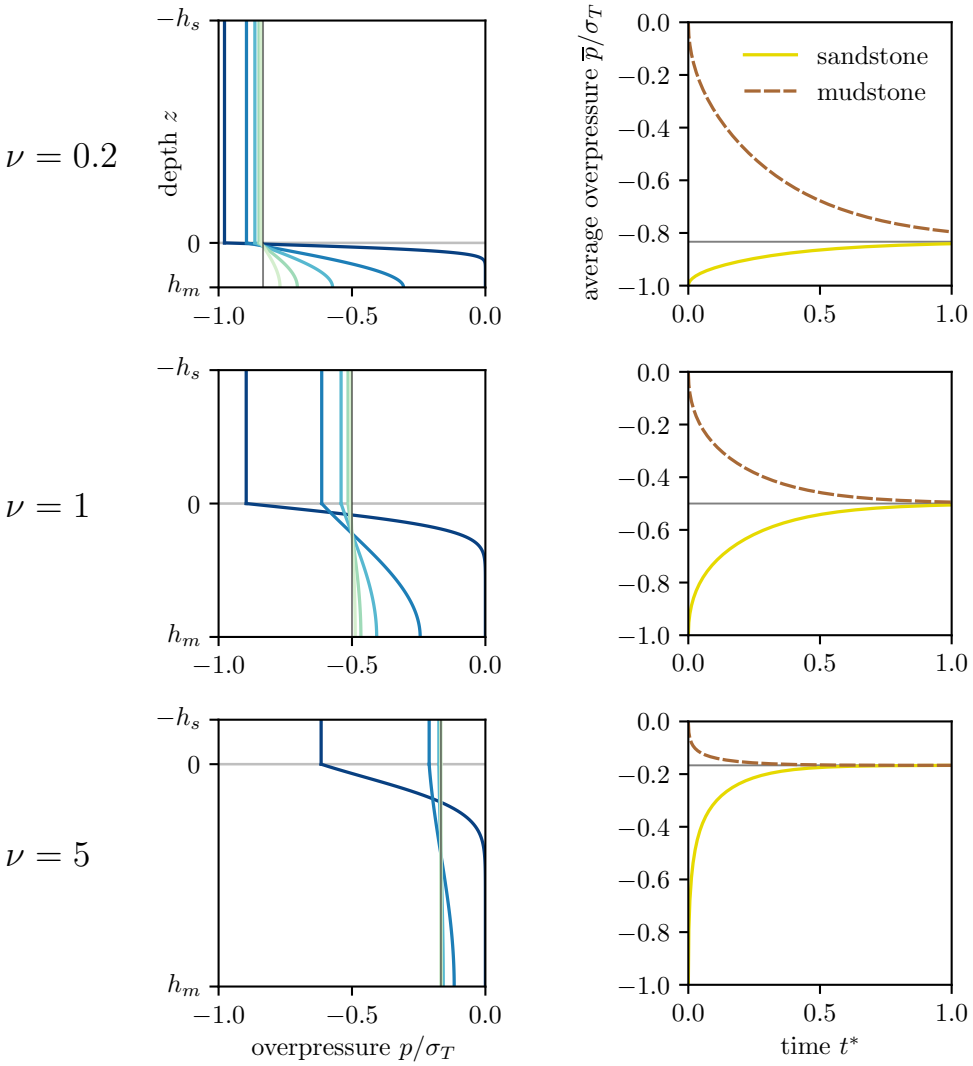

Figure 2.5: Pressure evolution after a venting episode for three different values of ν in the absence of tectonic compression. Left: Pressure–depth curves at different times with time increasing from dark to light. Right: Average pressure evolution of the sandstone (solid yellow) and mudstone (dashed brown). The late-time equilibrium pressure is also shown (grey).

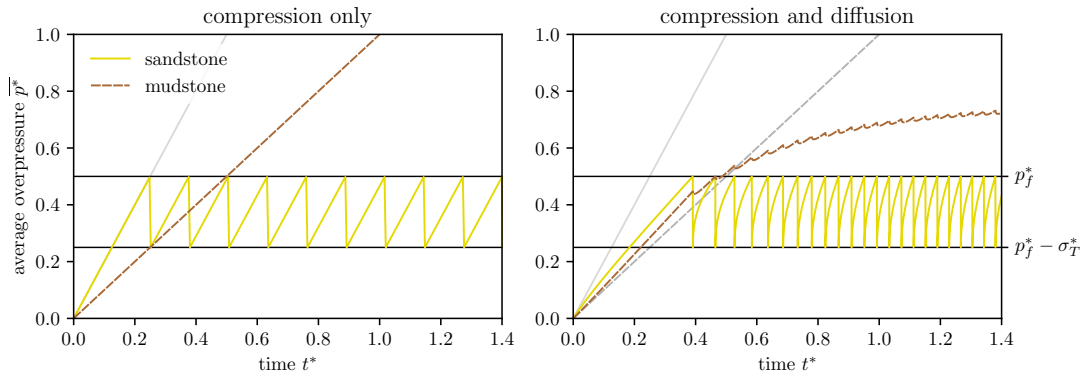

Figure 2.6: Comparison of average overpressure evolution of the sandstone (solid yellow) and mudstone (dashed brown) layers with compression only (left) and with both compression and pressure diffusion (right). Early time solutions without venting are plotted in grey for each layer. Here, $\gamma = 2$, $\nu = 5$, $p_f^* = 0.5$ and $\sigma_T^* = 0.25$.

cillates around its asymptotic mean value. In this periodic limit, we can recover explicit solutions for behaviour of this system.

Periodic venting

To express the periodic solution for pressure in the sandstone, we assume that venting initiates at time $t^* = 0$ and occurs thereafter at times $t^* = \tau^*, 2\tau^*, ..., N\tau^*, (N+1)\tau^*$, where τ^* is the dimensionless venting period to be determined. To simplify the solution, we further assume that tectonic compression initiated long before venting, such that the corresponding initial transient response is negligible. We note, however, that including this transient in the solution does not affect our results. Then, using the principle of superposition, the periodic solution for pressure in the sandstone is, for $N\tau^* < t^* < (N+1)\tau^*$,

$$p_s^* = \frac{\gamma+\nu}{1+\nu}t^* + \frac{\nu(\gamma-1)}{3(1+\nu)^2} - \sigma_T^* \sum_{n=1}^{N} \left(\frac{1}{1+\nu} + 2\nu \sum_{j=1}^{\infty} \frac{\exp\{-\xi_j^2(t^* - n\tau^*)\}}{\nu^2+\nu+\xi_j^2} \right), \qquad (2.27)$$

where τ^* is the dimensionless venting period, scaled with the characteristic time for pressure diffusion h_m^2/D_m (and hence the dimensional venting period is $\tau \equiv \tau^* h_m^2/D_m$). The periodic venting solution (2.27) is a function of two dimensionless parameters, ν and τ^*. Figure 2.7 shows how these parameters control the periodic recharge pathway.

Solving (2.27) for τ^* (Appendix 2.F) gives

$$\tau^* = \frac{\sigma_T^*}{\gamma + \nu}. \tag{2.28}$$

If $\tau^* \ll 1$ (i.e., if the dimensional venting period τ is much shorter than the diffusive time h_m^2/D_m), tectonic compression is the dominant contribution to pressure recharge and we recover a sawtooth; this is shown by the dashed black curve in Fig. 2.7a. If instead the venting period is much longer than the diffusive time, $\tau^* \gg 1$, diffusion equilibrates the sandstone and mudstone pressures to $p_s/\sigma_T = p_m/\sigma_T = \nu/(1+\nu)$; both then rise at the same rate, due to tectonic compression (solid black curve in Fig. 2.7a).

These diffusive effects are also controlled by the capacitance ratio ν of the two layers. If the hydraulic capacitance of the mudstone is negligible relative to that of the sandstone ($\nu \ll 1$), we again recover the sawtooth model (dashed black curve in Fig. 2.7b). Increasing ν (i.e., increasing the mudstone size) leads to faster diffusive pressure equilibration and a higher equilibration pressure, much like in Fig. 2.5. However, increasing ν also decreases the compressive pressurisation rate of the equilibrated sandstone and mudstone layers, as shown in Fig. 2.3. This means that a family of compressive and diffusive pressure recharge rates can produce the same venting period. Consequently, observational measurement of the mean venting period alone is insufficient to determine the dominant recharge mechanism. However, the dominant recharge mechanism can be inferred using the expression for venting period in combination with estimates of basin

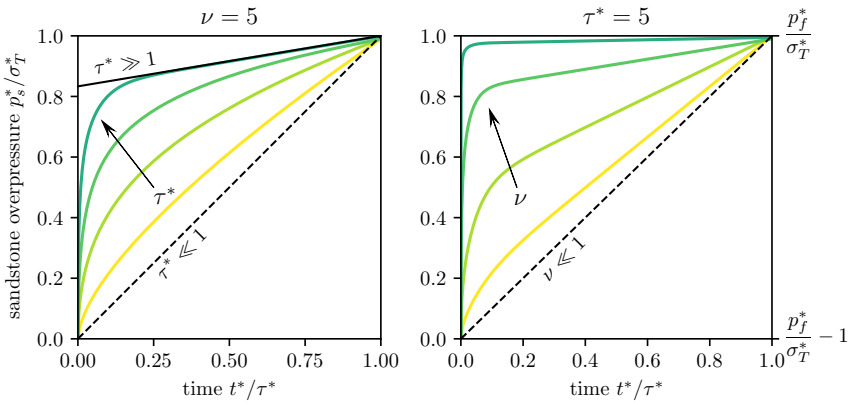

Figure 2.7: Sandstone pressure recharge behaviour during periodic venting, with varying τ^* and ν. We normalise dimensionless time t^* by the dimensionless venting period τ^*, such that $t^*/\tau^* \in [0, 1]$ over one period. Similarly, the dimensionless sandstone pressure p_s^* is scaled by the dimensionless tensile strength σ_T^*. With this normalisation, Eq. (2.27) is explicitly controlled by two dimensionless parameters, ν and τ^*. (a) Varying $\tau^* = (0.01, 0.1, 0.5, 2.5)$ at $\nu = 5$ with limiting behaviours for $\tau^* \ll 1$ (dashed black) and $\tau^* \gg 1$ (solid black). (b) Varying $\nu = (0.2, 1, 5, 50)$ at $\tau^* = 5$ with an limiting behaviour for $\nu \ll 1$ (dashed).

properties. To this end, we rewrite Eq. (2.28) in dimensional terms as

$$\tau = \frac{\sigma_T/\Gamma_s}{1 + \nu/\gamma}, \tag{2.29}$$

showing that the period is determined by the tensile strength of the impermeable seal, the tectonic pressurisation rate in the sandstone and $(1 + \nu/\gamma)$. This denominator is termed the venting frequency multiplier, where ν/γ is a dimensionless number that quantifies the effect of diffusion. Without pressure diffusion (i.e., for $\nu/\gamma \ll 1$), the frequency multiplier is unity and the period reduces to the compression-only (sawtooth) period, σ_T/Γ_s (Fig. 2.8). Considering the role of pressure diffusion divides the compression-only period or, equivalently, multiplies the compression-only frequency by a factor of $(1 + \nu/\gamma)$. If the frequency multiplier is much greater than unity, neglecting its effect will lead to an erroneous diagnosis of the tectonic compression rate from an observed venting period.

The results above enable us to estimate the contribution to pressure recharge from compression relative to that of pressure diffusion over a single period τ. In the absence of diffusion, compression will generate a pressure of $\gamma\tau^*$ per period. By definition, the overpressure at the end of one period is the amount needed to trigger venting, σ_T^*, so the relative contributions from compression and diffusion are $\gamma\tau^*/\sigma_T^* = (1+\nu/\gamma)^{-1}$, and $(\sigma_T^* - \gamma\tau^*)/\sigma_T^* = \nu/\gamma\,(1+\nu/\gamma)^{-1}$, respectively, having used Eq. (2.28). The ratio of the contribution from diffusion to the contribution from compression is then

$$\frac{\nu}{\gamma} = \frac{h_m}{h_s}\frac{\alpha_m}{\alpha_s}\frac{1+\lambda_s/\mu_s}{1+\lambda_m/\mu_m} \tag{2.30}$$

This dimensionless ratio is the ratio of fluid volumes expelled from each layer during tectonic compression at constant pore pressure. Remarkably, this quantity is independent of strain rate and permeability; it depends only on the thicknesses and poroelastic properties of the layers. Permeability plays an important role in the timescales associated with compression and diffusion, and thus in the shape of the recharge curve, but does not affect the overall contributions. The dimensionless quantity $(1+\lambda/\mu)$ can be rewritten as $1/(1-2v)$ where v is the Poisson ratio (not to be confused with the hydraulic capacitance ratio ν). We can simplify Eq. (2.30) by recognising that in most mudstone–sandstone successions, $v_s \sim v_m$, implying that $(1+\lambda_m/\mu_m)/(1+\lambda_s/\mu_s) \sim O(1)$, and the ratio of Biot coefficients is $\alpha_m/\alpha_s \sim O(1)$ so that

$$\frac{\nu}{\gamma} \sim \frac{h_m}{h_s}. \tag{2.31}$$

In other words, the role of pressure diffusion relative to compression is controlled primarily by the thickness of the mudstone relative to that of the sandstone. This equation means that for a mudstone unit that is thick compared to the adjacent sandstone, diffusion dominates the pressure recharge. Fluid venting phenomena are frequently observed in

mudstone-dominated basins (Cartwright & Santamarina 2015), so pressure diffusion is likely to be a major contributor to pressure recharge for fluid venting phenomena.

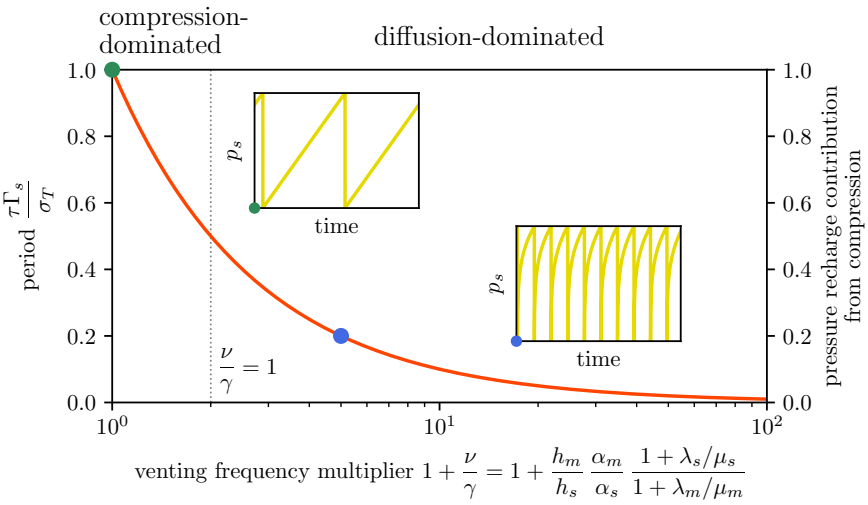

Figure 2.8: Venting period (left axis) and fraction of total pressure recharge from compression (right axis) as functions of the venting frequency multiplier, $(1 + \nu/\gamma)$, where the dimensionless ratio ν/γ measures the contribution of pressure diffusion relative to that of compression. The two quantities have the same mathematical relationship with $(1+\nu/\gamma)$ and therefore follow the same curve. The same function is the pressure recharge contribution from tectonic compression. Insets show example compression-dominated (green dot) and diffusion-dominated (blue dot) pressure evolution curves for the sandstone.

2.3 Discussion

The expression derived above for the venting period can be used to interpret observations of episodic venting and to infer the history of tectonic compression. As a prototype of such analysis, we consider the Oceanus pockmark trail located in the North Levant Basin (Cartwright et al. 2018). Cartwright et al. (2021) performed a similar analysis, beginning with the assumption that the associated reservoir was hydrostatically pressured (i.e., zero overpressure) immediately after the Messinian Salinity Crisis. They then estimated that ∼30 MPa of overpressure must have been generated over a period of ∼3 Myr to exceed the critical fracture pressure and initiate the first venting episode, implying a pressurisation

rate of ∼10 MPa/Myr prior to initiation of venting. They attributed this pressurisation rate solely to tectonic compression.

The Oceanus trail records 21 venting episodes from ∼1.7 Ma until recent, suggesting a mean venting period of ∼80 kyr. During each venting episode, the Messinian salt layer is re-fractured and fluid is expelled until the sandstone pressure drops by the tensile strength of the salt, as described above. Extended leak-off tests suggest that this tensile strength is in the range 2 ± 1 MPa (Bérest et al. 2015). Consequently, a pressurisation rate of 25 ± 13 MPa/Myr would be required to recharge the reservoir to failure every 80 kyr. At Oceanus, the pre-salt clastic succession from which the fluid is sourced is predominantly mudstone, with $h_m/h_s \sim 20 \pm 7$ (Cartwright et al. 2021). Using typical sandstone and mudstone properties from Table 2.1 in Eq. (2.30), we estimate the venting frequency multiplier to be $(1 + \nu/\gamma) \sim 24 \pm 12$. With this result, we use Eq. (2.29) to calculate the pressurisation rate due to tectonic compression during the periodic-venting phase to be $\Gamma_s \sim 1.4 \pm 0.9$ MPa/Myr. This result is much lower than the total inferred pressurisation rate during periodic venting because the major recharge contribution is from pressure diffusion, with a rate of 24 ± 14 MPa/Myr. Additionally, the inferred pressurisation rate due to tectonic compression during periodic venting is much lower than that obtained by Cartwright et al. (2021) for the period prior to the onset of venting. One possible explanation for this discrepancy is that tectonic compression has eased since the initiation of venting. However, it is also plausible that the Messinian Salinity Crisis left the Oceanus reservoir significantly overpressured (Al-Balushi et al. 2016), rather than hydrostatically pressured, and that the rate of tectonic compression has been roughly constant since that time.

Tectonic compression of the North Levant Basin stems from activity on the Dead Sea Transform fault, where geodetic strain rates of order 10^{-16} s^{-1} are observed (Palano et al. 2013). From the pressurisation rate calculated above, we can infer the strain

Parameter	**Description**	**mean**	**std. dev.**	**min.**	**max.**	**Reference**
σ_T (MPa)	salt tensile strength	2	1	0.5	4	Bérest et al. (2015)
h_s (m)	sandstone thickness	150	50	50	200	Cartwright et al. (2021),
h_m (m)	mudstone thickness	2500	250	2000	3000	Fig. 2b
α_s	sandstone Biot coefficient	0.62	0.17	0.38	0.83	Ge & Garven (1992)
α_m	mudstone Biot coefficient	0.68	0.35	0.30	0.98	
v_s	sandstone Poisson ratio	0.24	0.04	0.20	0.30	
v_m	mudstone Poisson ratio	0.25	0.05	0.15	0.30	
K_s (GPa)	sandstone bulk modulus	18	8	8	30	
K_m (GPa)	mudstone bulk modulus	15	17	5	33	
ϕ_s	sandstone porosity	0.22	0.01	0.19	0.24	Ortega et al. (2018)
ϕ_m	mudstone porosity	0.20	0.05	0.05	0.30	Yang & Aplin (2007)
$\log_{10} k_m$ ($\log_{10}$ m^2)	(log) mudstone permeability	-19	0.5	-22	-18	
η (mPa s)	water viscosity	0.3	0.1	0.1	0.5	Abramson (2007)
c_ℓ (10^{-11} Pa^{-1})	water compressibility	4.0	0.1	3.7	4.3	Fine & Millero (1973)

Table 2.1: Sandstone and mudstone properties used in estimating the compression rate at the Oceanus pockmark trail in the North Levant Basin. We assign a truncated normal distribution for each parameter, taking all parameters to be uncorrelated. The mean and standard deviation of each distribution, as well as the minimum and maximum values at which the distributions are truncated, are given by the values presented in the table. From these distributions, we use the model under a Monte Carlo framework to calculate a distribution for the local strain rate at Oceanus.

rate associated with tectonic compression at the Oceanus pockmark trail. Using typical sandstone properties (Table 2.1), we use Eq. (2.13) to estimate a horizontal strain rate of $1.6 \pm 1.1 \times 10^{-4}$ Myr^{-1} $= 5.1 \pm 3.7 \times 10^{-18}$ s^{-1}. This value is much smaller than the observed rate of regional shortening because folding and thrusting across the basin (Oppo et al. 2021) accommodate a large portion of the shortening. Only the much smaller fraction accommodated by compression is relevant to our model. Strain rates typically vary laterally across sedimentary basins, so this measurement only provides a local strain rate at the Oceanus pockmark trail.

The above analysis of the Oceanus pockmark trail relies upon the assumption that the transition to periodic venting is complete. This transition occurs after the onset of venting over the characteristic poroelastic timescale of the system h_m^2/D_m (Appendix 2.E). For the Levant Basin, using estimated values from Table 2.1, we calculate an expected poroelastic timescale of 23 kyr. Within the 95% confidence interval, however, the poroelastic timescale could be an order of magnitude higher or lower. This range is primarily due to the uncertainty in the mudstone permeability. For the typical ∼100 kyr venting period, this implies that the transition to periodic venting is complete by the second venting episode or, at most, after a few episodes. Venting observations from the Oceanus trail and other trails across the North Levant Basin show no evidence of an initial transition to periodic venting. This suggests that the regional poroelastic timescale is similar to or less than the ∼100 kyr venting period and that our assumption of periodicity is justified.

Oppo et al. (2021) documented a set of 12 pockmark trails across the margin of the North Levant Basin, where venting initiates at a similar time to Oceanus. Mean venting periods vary between trails, ranging from ∼30 to ∼220 kyr. Equation (2.29) suggests that these spatial variations in period can most likely be attributed to spatial variations in layer thicknesses and the local tectonic strain rate. Moreover, the time of the first

venting episode varies significantly between trails; this is controlled by the local tectonic strain rate and the residual overpressure from the Messinian Salinity Crisis. The time of the last observed venting event also varies between trails, potentially associated with the time that compression ceases locally. However, a given reservoir may continue to vent after tectonic compression ceases, driven by pressure diffusion alone (Appendix 2.H). The number of excess venting episodes depends on the local hydraulic capacitance ratio and salt tensile strength.

Oppo et al. (2021) showed that pipe trails have formed exclusively above anticlines across the North Levant Basin. From this, one might infer that folding generates sufficient overpressure for venting, despite our assumption of the contrary for the present model. Cartwright et al. (2021) estimate that growth of the Oceanus anticline has increased the reservoir trap capacity by 320 m since the initiation of venting. Anticline growth generates overpressure in a high-permeability reservoir through the lateral transfer of pressure to its crest from the surrounding overpressured, low-permeability rock, which is the mudstone in this case (Flemings et al. 2002). If the reservoir has a parabolic fold geometry with constant thickness, then the corresponding increase in overpressure is $\frac{1}{3}(\rho_m - \rho_g)g\Delta h$, where ρ_m is the density of the mudstone, ρ_g is the density of gas, g is the acceleration due to gravity, and Δh is the increase in trap capacity. Using density values from Cartwright et al. (2021), we obtain an increase in overpressure by lateral transfer of $\sim$2 MPa. Additionally, an increase in trap capacity will enable the accumulation of a thicker gas column, increasing overpressure due to buoyancy by $(\rho_g - \rho_w)g\Delta h \sim 1$ MPa, where ρ_w is the density of water. The overpressure generated in the sandstone due to fold growth is thus negligible, merely supplying enough overpressure for one additional venting episode. Despite this, the additional overpressure (and high topography, hence reduced compressive stress) associated with anticlines make them preferential sites for venting.

However, the overpressure generated by fold growth is comparable to that generated by tectonic compression, inferred to be 2.4 ± 1.5 MPa since the initiation of venting. The fundamental difference between these overpressure mechanisms is that tectonic compression also pressurises the mudstone. For example, an overpressure increase in the mudstone of 1 MPa can provide an increase in overpressure in the sandstone of ν MPa via pressure diffusion. In mudstone-dominated basins $\nu \gg 1$, thus a small amount of mudstone overpressure can drive many venting episodes. This suggests that overpressure mechanisms that pressurise the mudstone, e.g., tectonic compression, disequilibrium compaction and sea-level change are potent drivers of episodic fluid venting in other sedimentary basins.

Our model can speculatively be applied to basins containing mud volcanoes, where a sandstone layer may not be present. To do so, the modelled sandstone layer can be recast as a fluidised mud region that depressurises during venting. The thickness of the depressurised region depends on details of the fracture mechanics of venting, and may vary as mud is expelled. If this region is much smaller than the overall mudstone thickness, then it is likely that pressure diffusion provides the dominant contribution to recharge. In the Eastern Mediterranean, the West Nile Delta hosts linear trails composed of fluid escape pipes and mud volcanoes. Sandstone reservoirs are not observed, in contrast to the North Levant Basin. The West Nile Delta is likely pressurised by hydrocarbon generation and lateral pressure transfer rather than tectonic compression (Kirkham et al. 2022). Despite these differences, similar $\sim$100 kyr periods are observed in the West Nile Delta (Kirkham et al. 2022). This timescale is comparable to the poroelastic diffusion time for the North Levant Basin, suggesting that recharge in this region is also controlled by pressure diffusion.

The model is readily generalisable to other settings and scenarios. For example, the impermeable sealing layer could be replaced with a permeable unit (e.g., mudstone) to study the effect of pressure dissipation due to fluid migration through an imperfect seal.

The model could also be reformulated to include disequilibrium compaction as the active overpressure mechanism (Appendix 2.G). Disequilibrium compaction is a prevalent driver of overpressure in low-permeability sediments (Osborne & Swarbrick 1997), especially in basins with high sedimentation rates (e.g., the South Caspian Basin, see Stewart & Davies 2006). For this mechanism, an increasing vertical stress acts on the system, rather than a horizontal compression. Much of our qualitative findings will also apply for disequilibrium compaction.

Despite the widespread occurrence of venting phenomena, there are many basins comprising overpressured mudstones that have not vented. Venting requires a mechanism that generates overpressure faster than fluid flow can dissipate it, and that is active for long enough to achieve critical overpressures. Therefore, lateral reservoir connectivity and/or poor vertical sealing can inhibit fluid venting. Venting is also less likely to initiate at larger depths, where the critical fracture pressure is larger. Once venting initiates, further episodes require pressure recharge in the reservoir unit, from either sustained overpressure generation or by pressure diffusion from an adjacent overpressured mudstone.

Our model invokes a variety of simplifying assumptions. These assumptions make the model tractable and transparent, but also carry limitations. In reality, tectonic compression is unlikely to be a constant-strain-rate process and compression may not be the sole overpressure mechanism in a basin. Furthermore, basin stratigraphies seldom consist of uniform, horizontal layers; layer topography and heterogeneity will affect the spatial distribution of overpressure and fracture pressure, and thus also of venting loci. The sedimentary layers themselves are composed of rocks with porosity-dependent permeability that do not behave perfectly poro-elastically. For example, many sedimentary rocks may partially fluidise during sudden fluid expulsion. We have assumed that the vented fluid is water, but in reality it is a mixture of water, natural gas and sediment. However, we do

not expect any of these features to change the key qualitative implications of our model.

Many open questions remain regarding fluid venting phenomena that are not addressed by this work. The mechanics of venting are not explicitly stated in the model; the high permeability of the sandstone layer enables us to circumvent this. If the sandstone is also overlain by mudstone, then we might expect that hydraulic fracturing occurs through the mudstone. But the mudstone is also predicted to be overpressured and to recharge the reservoir during episodic venting. It is unclear how a hydraulic fracture could propagate through a unit with a higher overpressure; perhaps the presence of natural gas and fluidised sediment enables this. This lack of clarity in the conditions for venting motivates incorporation of fracture mechanics and mudstone fluidisation into our model. Furthermore, since the model contains only one spatial dimension, it cannot be used to address observations such as the strong correlation of venting sites with areas of high reservoir-layer topography. This strong spatial dependence can lead to clusters of multiple venting sites in close proximity. For example, in the North Levant Basin margin (Oppo et al. 2021), four pockmark trails originate along the crest of the same folded sandstone reservoir and thus may be hydraulically connected. A model that considers these spatial variations may be capable of inferring basin properties such as reservoir architecture from dates of venting episodes.

2.4 Conclusions

We have developed and solved a one-dimensional model of pressure evolution of sedimentary layers subject to horizontal tectonic compression, leading to episodic fluid venting. Our main goal was to elucidate the interactions between the three fundamental ingredients of episodic venting: pressure build-up, pressure diffusion and hydraulic fracturing. The main conclusions from the study are as follows.

- In the absence of hydraulic fracturing, two time regimes emerge. At early times, the pressure of each layer rises independently at a rate determined by the elastic properties of the layer. At timescales corresponding to mudstone fluid flow ($t \gg h_m^2/D_m$), layer pressures equilibrate by pressure diffusion and rise at the same rate.

- Sustained tectonic compression will generate extreme overpressures required for hydraulic fracturing of the sealing layer. Once hydraulic fracturing initiates, the sandstone pressure drops rapidly. The sandstone pressure is then slowly recharged by tectonic compression and pressure diffusion from the mudstone layer, leading to repeated venting episodes.

- During episodic venting, the time interval between episodes tends towards a fixed period, given by $\tau = \sigma_T/\Gamma_s/(1+\nu/\gamma)$, where σ_T is the tensile strength of the seal, Γ_s is the pressure build-up rate in the sandstone layer due to tectonic compression, and $(1+\nu/\gamma)$ is the venting frequency multiplier.

- The venting frequency multiplier $(1+\nu/\gamma)$ is determined by the dimensionless ratio ν/γ, which is independent of strain rate and permeability. When ν/γ is small, diffusion is negligible compared to compression and the sandstone pressure evolves as a sawtooth wave with a venting period $\tau \sim \sigma_T/\Gamma_s$. The period decreases with increasing ν/γ as the additional contribution to pressure recharge from diffusion increases. Based on estimates of sandstone and mudstone elastic properties, ν/γ is controlled by the ratio of thicknesses of the mudstone and sandstone layers. Fluid venting phenomena are commonly found in mudstone-dominated basins; we have shown that in these settings, pressure recharge will be dominated by diffusion.

- More generally, we have shown that tectonic compression cannot be decoupled from pressure diffusion. Episodic expulsion depends on more than simply the rate of tectonic compression — pressure diffusion can markedly reduce the time interval

between episodes.

Appendices

2.A Storage equation

Here, we follow the derivation of the storage equation by Verruijt (1969). Starting from conservation of mass of the fluid ℓ and solid g phases,

$$\frac{\partial \phi \rho_\ell}{\partial t} + \boldsymbol{\nabla} \cdot \phi \rho_\ell \boldsymbol{v}_\ell = 0, \tag{32}$$

$$\frac{\partial (1-\phi) \rho_g}{\partial t} + \boldsymbol{\nabla} \cdot (1-\phi) \rho_g \boldsymbol{v}_g = 0, \tag{33}$$

where ϕ is the porosity of the medium, ρ_i is the phase density and $\boldsymbol{v}_i$ is the phase velocity. Assuming spatial variations in phase densities are negligible, then

$$\frac{1}{\rho_\ell} \frac{\partial \phi \rho_\ell}{\partial t} + \boldsymbol{\nabla} \cdot \phi \boldsymbol{v}_\ell = 0, \tag{34}$$

$$\frac{1}{\rho_g} \frac{\partial (1-\phi) \rho_g}{\partial t} + \boldsymbol{\nabla} \cdot (1-\phi) \boldsymbol{v}_g = 0. \tag{35}$$

For the solid phase, c_g is the compressibility of the solid grains such that for the pure solid material, $c_g \equiv 1/\rho_g \, \partial \rho_g / \partial p$. However, in poroelastic materials, grains compress in response to changes in both total isotropic stress σ and pore pressure p.

We determine this relationship by considering an undrained compression of Δp fol-

lowed by a drained compression of $(-\Delta\sigma) - \Delta p$ such that the overall change in pore pressure is Δp and the overall change in isotropic stress is $-\Delta\sigma$ (stress is tension-positive). For an undrained deformation of magnitude Δp, the change in grain density $\Delta\rho_g = c_g\rho_g\Delta p$, by definition. For a drained compression of magnitude $(-\Delta\sigma) - \Delta p$, the grains experience an amplified stress increase of $-(\Delta p + \Delta\sigma)/(1-\phi)$, so

$$\Delta\rho_g = -c_g\rho_g\frac{\Delta p + \Delta\sigma}{1-\phi}. \tag{36}$$

Superposition of these two responses gives the change in grain density,

$$\Delta\rho_g = -\frac{c_g\rho_g}{1-\phi}(\phi\Delta p + \Delta\sigma). \tag{37}$$

If these changes occur over a time Δt, the limit as $\Delta t \to 0$ is

$$\frac{\partial\rho_g}{\partial t} = -\frac{c_g\rho_g}{1-\phi}\left(\phi\frac{\partial p}{\partial t} + \frac{\partial\sigma}{\partial t}\right). \tag{38}$$

Using (38), we can simplify the solid mass conservation equation (35) to

$$-\frac{\partial\phi}{\partial t} - \phi c_g\frac{\partial p}{\partial t} - c_g\frac{\partial\sigma}{\partial t} + \boldsymbol{\nabla}\cdot(1-\phi)\boldsymbol{v}_s = 0. \tag{39}$$

Applying the definition of fluid compressibility $c_\ell \equiv 1/\rho_\ell\,\partial\rho_\ell/\partial p$ to (34) gives

$$\frac{\partial\phi}{\partial t} + \phi c_\ell\frac{\partial p}{\partial t} + \boldsymbol{\nabla}\cdot\phi\boldsymbol{v}_\ell = 0. \tag{40}$$

We add (39) and (40) to eliminate the porosity derivative terms, resulting in

$$\frac{\partial e}{\partial t} + \phi(c_\ell - c_g)\frac{\partial p}{\partial t} - c_g\frac{\partial\sigma}{\partial t} = -\boldsymbol{\nabla}\cdot\boldsymbol{q}, \tag{41}$$

where $\boldsymbol{q} \equiv \phi(\boldsymbol{v}_\ell - \boldsymbol{v}_g)$ and $\partial e/\partial t \equiv \boldsymbol{\nabla}\cdot\boldsymbol{v}_g$. We can eliminate the isotropic total stress from

the equation using Terzaghi's principle, $\sigma = \sigma' - \alpha p$ where the effective stress $\sigma' = e/c$ and $\alpha \equiv 1 - c_g/c$ with c denoting the compressibility of the solid skeleton. It follows that

$$\alpha \frac{\partial e}{\partial t} + S \frac{\partial p}{\partial t} = -\boldsymbol{\nabla} \cdot \boldsymbol{q}, \tag{42}$$

where the storativity $S \equiv \phi c_\ell + (\alpha - \phi) c_g$. Equation (42) is termed the storage equation by Verruijt (1969). The only assumptions made in deriving this equation are that spatial variations in phase densities are negligible and that each phase is linearly compressible.

2.B Stress conditions for hydraulic fracturing

For this analysis, we assume that the initial compressive stress in the y-direction is less than the lithostatic stress. As compression is acting in the x-direction, a vertical fracture will open aligned with the y-direction. In this case, the condition for hydraulic fracturing is

$$P_f > -\sigma_{yy} + \sigma_T. \tag{43}$$

Assuming a steady-state, hydraulic fracturing thus requires that the sandstone pressure P_s increases faster than $-\sigma_{yy}$,

$$\frac{\partial P_s}{\partial t} > -\frac{\partial \sigma_{yy}}{\partial t}. \tag{44}$$

We use this condition to predict if hydraulic fracturing will occur under different stress conditions. If we assume $\partial_t \sigma_{yy} = 0$, then vertical hydraulic fracturing will always occur. However, if we instead assume $\partial_t e_{yy} = 0$, then

$$(\lambda_s + 2\mu_s) \frac{\partial e}{\partial t} = \alpha_s \frac{\partial P_s}{\partial t} - 2\mu_s \dot{e}_{xx}. \tag{45}$$

From the storage equation for the sandstone,

$$\frac{\partial P_s}{\partial t} = \frac{2\alpha_s \mu_s \dot{e}_{xx}}{\alpha_s^2 + S_s(\lambda_s + 2\mu_s)} - \frac{\lambda_s + 2\mu_s}{\alpha_s^2 + S_s(\lambda_s + 2\mu_s)} \frac{q}{h_s}, \tag{46}$$

where $q < 0$ indicates flow from the mudstone into the sandstone. From the condition for vertical hydraulic fracturing, we obtain

$$2\mu_s \dot{e}_{xx}[\alpha_s(1-\alpha_s) - S_s\lambda_s] - [\lambda_s + 2\mu_s(1-\alpha_s)]\frac{q}{h_s} > 0. \tag{47}$$

To simplify interpretation, we assume $\alpha \sim 1$, giving

$$\dot{e}_{xx} < -\frac{q/h_s}{2\mu_s S_s}. \tag{48}$$

If the mudstone is impermeable, $q = 0$, thus vertical hydraulic fracturing will never occur. Indeed, an additional flux from the mudstone is required for fracturing when $\partial_t e_{yy} = 0$. This only occurs when the sandstone is more compressible than the mudstone, which is not commonly observed. Furthermore, if the sandstone is highly compressible, i.e., S_s is large, a higher flux may be required to satisfy the inequality.

However, assuming $\partial_t e_{yy} = 0$ is likely less physically realistic as pore pressure increases of, for example, ∼10 MPa would lead to predictions of ∼10 MPa differential stresses; these stresses are typically relieved by faulting in natural systems. For this reason we assume $\partial_t \sigma_{yy} = 0$ in the main text.

2.C Compression solution

The Laplace transform $\mathbb{F}$ of a function f is defined as

$$\mathbb{F}(s) = \int_0^\infty f(t) \exp(-st)\, \mathrm{d}t. \tag{49}$$

Transforming equations (2.18)–(2.19) to Laplace space using $p_m^*(z^*, 0) = 0$ gives a second-order ordinary differential equation,

$$\frac{\mathrm{d}^2 \mathbb{P}_m^*}{\mathrm{d}z^{*2}} - s^* \mathbb{P}_m^* = -\frac{1}{s^*} \quad \text{for } z^* \in (0, 1), \tag{50}$$

with boundary conditions

$$\left.\begin{aligned} \mathbb{P}_m^* &= \frac{\gamma}{s^{*2}} + \frac{\nu}{s^*} \frac{\mathrm{d}\mathbb{P}_m^*}{\mathrm{d}z^*} && \text{at } z^* = 0, \\ \frac{\mathrm{d}\mathbb{P}_m^*}{\mathrm{d}z^*} &= 0 && \text{at } z^* = 1. \end{aligned}\right\} \tag{51}$$

The solution to this system of equations is

$$\mathbb{P}_m^* = \frac{1}{s^{*2}} + \frac{\gamma - 1}{s^{*2}} \frac{\cosh(1 - z^*)\sqrt{s^*}}{\cosh \sqrt{s^*} + \nu \sinh \sqrt{s^*}/\sqrt{s^*}}. \tag{52}$$

The inverse Laplace transform can be expressed as

$$f(t) = \frac{1}{2\pi i} \lim_{T \to \infty} \int_{G - iT}^{G + iT} \mathbb{F}(s) \exp(st)\, \mathrm{d}s, \tag{53}$$

where G is greater than the real part of all the singularities of $\mathbb{F}(s)$. Assuming that the integrand is single-valued, it follows from the Cauchy residue theorem that the integral

equals the sum of the residues at all the poles $s_1, s_2, ..., s_j$,

$$f(t) = \sum_j \operatorname*{Res}_{s=s_j} \Big\{ \mathbb{F}(s_j) \exp(s_j t) \Big\}. \tag{54}$$

Equation (52) has poles at $s^* = 0$ and at the zeros of the denominator of the second term, i.e.,

$$\tanh \sqrt{s^*} = -\frac{\sqrt{s^*}}{\nu}. \tag{55}$$

The solutions to this equation are imaginary, so by substituting $\sqrt{s^*} = i\xi$ we obtain the transcendental equation

$$\tan \xi = -\frac{\xi}{\nu}. \tag{56}$$

For the pole at $s^* = 0$, using Taylor expansions we obtain the late-time solution

$$p_m^*(z^*, \infty) = \frac{\gamma + \nu}{1 + \nu} t^* + \frac{\gamma - 1}{1 + \nu} \left\{ \frac{\nu}{3(1 + \nu)} - \tfrac{1}{2} z^* (2 - z^*) \right\}. \tag{57}$$

The residue of a quotient $f(s)/g(s)$ at a simple zero, s_0 is given by

$$\operatorname*{Res}_{s=s_0} (f/g) = \lim_{s \to s_0} \frac{f(s)}{g(s)} = \frac{f(s_0)}{g'(s_0)}, \tag{58}$$

hence the residues at $s^* = s_j^*$ can be expressed as,

$$-2\nu(\gamma - 1) \sum_{j=1}^{\infty} \frac{\cos\{\xi_j (1 - z^*)\}}{\cos \xi_j} \frac{\exp(-\xi_j^2 t^*)}{\xi_j^2 (\nu^2 + \nu + \xi_j^2)}. \tag{59}$$

Combining residues gives the desired solution,

$$p_m^* = \frac{\gamma + \nu}{1 + \nu} t^* + \frac{\gamma - 1}{1 + \nu} \left\{ \frac{\nu}{3(1 + \nu)} - \tfrac{1}{2} z^* (2 - z^*) \right\} - 2\nu(\gamma - 1) \sum_{j=1}^{\infty} \frac{\cos\{\xi_j (1 - z^*)\}}{\cos \xi_j} \frac{\exp(-\xi_j^2 t^*)}{\xi_j^2 (\nu^2 + \nu + \xi_j^2)}, \tag{60}$$

which can be expressed more compactly, with

$$p_m^* = t^* + (\gamma - 1)\left\{ \frac{t^*}{1+\nu} + 2\nu \sum_{j=1}^{\infty} \frac{\cos\{\xi_j(1-z^*)\}}{\cos\xi_j} \frac{1-\exp(-\xi_j^2 t^*)}{\xi_j^2(\nu^2+\nu+\xi_j^2)} \right\}. \tag{61}$$

Early-time compression

At early times, $\exp(-\xi_j^2 t^*) \sim 1 - \xi_j^2 t^*$,

$$p_m^* \sim t^* + (\gamma - 1)\left\{ \frac{1}{1+\nu} + 2\nu \sum_{j=1}^{\infty} \frac{\cos\{\xi_j(1-z^*)\}}{\cos\xi_j} \frac{1}{\nu^2+\nu+\xi_j^2} \right\} t^*. \tag{62}$$

Therefore, the mudstone overpressure initially increases linearly with time. By applying the initial condition $\tilde{p}_m^*(z^*, 0) = -H(-z^*)$, where H is the Heaviside function, to the fluid venting solution (2.26), we find that

$$\sum_{j=1}^{\infty} \frac{\cos\{\xi_j(1-z^*)\}}{\cos\xi_j} \frac{1}{\nu^2+\nu+\xi_j^2} = \frac{(1+\nu)H(-z^*) - 1}{2\nu(1+\nu)}. \tag{63}$$

Therefore,

$$p_m^* \sim \{1 + (\gamma - 1)H(-z^*)\} t^*, \tag{64}$$

i.e., $p_s^* = p_m^*(0, t) \sim \gamma t^*$ and, for $z^* > 0$, $p_m^* \sim t^*$.

2.D Fluid venting solution

For fluid venting, we assert that at $t^* = t_f^*$ the sandstone instantaneously drops in pressure by σ_T^* such that

$$\left.\frac{\partial p_m^*}{\partial t^*}\right|_{z^*=0} = \gamma + \nu \left.\frac{\partial p_m^*}{\partial z^*}\right|_{z^*=0} - \sigma_T^* \delta(t^* - t_f^*). \tag{65}$$

Transforming the augmented system of equations to Laplace space using $p^*_m(z^*, 0) = 0$, we have

$$\frac{\mathrm{d}^2\mathbb{P}^*_m}{\mathrm{d}z^{*2}} = \mathbb{P}^*_m - \frac{1}{s^{*2}}, \tag{66}$$

with boundary conditions

$$\left.\begin{aligned} \mathbb{P}^*_m &= \frac{\gamma}{s^{*2}} + \frac{\nu}{s^*}\frac{\mathrm{d}\mathbb{P}^*_m}{\mathrm{d}z^*}\bigg|_{z^*=0} - \frac{\sigma^*_T \mathrm{e}^{-s^* t^*_f}}{s^*} && \text{at } z^* = 0, \\ \frac{\mathrm{d}\mathbb{P}^*_m}{\mathrm{d}z^*} &= 0 && \text{at } z^* = 1. \end{aligned}\right\} \tag{67}$$

The particular solution to this system of equations is

$$\mathbb{P}^*_m = \frac{1}{s^{*2}} + \frac{\gamma - 1}{s^{*2}} \frac{\cosh(1 - z^*)\sqrt{s^*}}{\cosh\sqrt{s^*} + \nu \sinh\sqrt{s^*}/\sqrt{s^*}} - \frac{\sigma^*_T \mathrm{e}^{-s^* t^*_f}}{s^*} \frac{\cosh(1 - z^*)\sqrt{s^*}}{\cosh\sqrt{s^*} + \nu \sinh\sqrt{s^*}/\sqrt{s^*}}. \tag{68}$$

We know the inverse transform of the first two terms from the solution for compression in the absence of venting (Appendix 2.C). The third term describes the system response to venting, thus we discard the former two terms for the present analysis. We denote the venting response with $\tilde{p}^*_m$. The third term of Eqn. (68) has residue at $s^* = 0$, giving the late-time solution

$$\tilde{p}^*_m(z^*, \infty) = -\frac{\sigma^*_T}{1 + \nu}. \tag{69}$$

Adding the residue at the poles of the denominator s^*_j, we get

$$\tilde{p}^*_m = -\frac{\sigma^*_T}{1 + \nu} - 2\nu\sigma^*_T \sum_{j=1}^{\infty} \frac{\cos\{\xi_j(1 - z^*)\}}{\cos\xi_j} \frac{\exp\{-\xi_j^2(t^* - t^*_f)\}}{\nu^2 + \nu + \xi_j^2}, \tag{70}$$

where ξ_j is the j-th solution to $\tan\xi = -\xi/\nu$.

2.E Transition to periodic behaviour

To understand the pressure evolution without oscillations due to venting, we take the sandstone pressure to be a constant. For simplicity, we set $p_s^* = 0$ so the system of equations become

$$\frac{\partial p_m^*}{\partial t^*} = 1 + \frac{\partial^2 p_m^*}{\partial z^{*2}} \quad \text{for } z^* \in [0,1]. \tag{71}$$

and

$$\left.\begin{aligned} p_m^* &= 0 && \text{at } z^* = 0, \\ \frac{\partial p_m^*}{\partial z^*} &= 0 && \text{at } z^* = 1. \end{aligned}\right\} \tag{72}$$

Solving this system in Laplace space gives

$$\mathbb{P}_m^* = \frac{1}{s^{*2}}\left[1 - \frac{\cosh(1-z^*)\sqrt{s^*}}{\cosh\sqrt{s^*}}\right]. \tag{73}$$

Equation (73) has a pole at $s^* = 0$, with residue representing the steady-state solution

$$p_m^*(z^*, \infty) = -\tfrac{1}{2} z^*(2 - z^*). \tag{74}$$

The remainder of the poles are at the zeros of the denominator of the second term, i.e. $s_n^* = -(2n-1)^2\pi^2/4$ for $n \in \mathbb{Z}$. Combining residues gives the full solution,

$$p_m^* = \tfrac{1}{2} z^*(2 - z^*) + \frac{16}{\pi^3}\sum_{n=1}^{\infty} \frac{(-1)^n}{(2n-1)^3} \cos\{(1-z^*)(2n-1)\pi/2\} \exp\{-t^*\,(2n-1)^2\pi^2/4\}. \tag{75}$$

Therefore, the average mudstone pressure evolves such that,

$$\overline{p_m^*} = \frac{1}{3} - \frac{32}{\pi^4}\sum_{n=1}^{\infty} \frac{\exp\{-t^*\,(2n-1)^2\pi^2/4\}}{(2n-1)^4}. \tag{76}$$

We compare the constant-pressure solution with the full solution for an example scenario in Fig. 9. There is good agreement between the two solutions for the mudstone overpressure, with the constant-pressure solution generally following the full solution but without the oscillations produced by venting. Minor deviations between solutions at early times ($t^* \sim 0.4$) are explained by differences in their initial states.

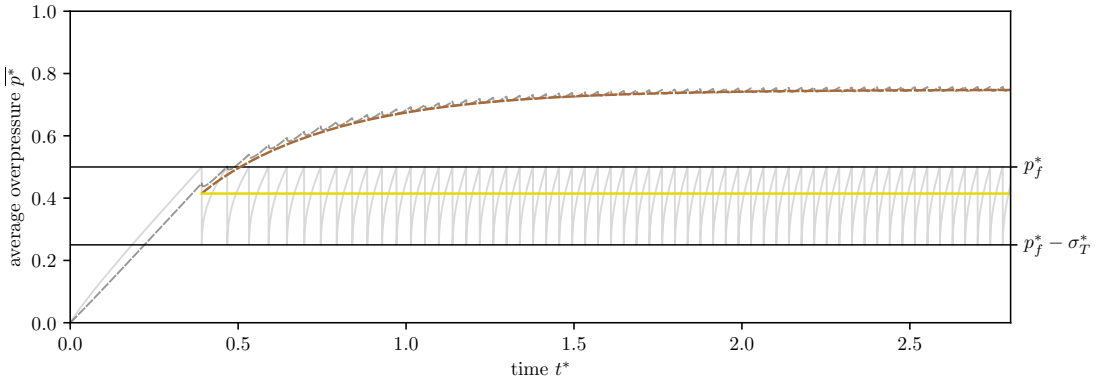

Figure 9: Average overpressure evolution of the mudstone layer (brown dashed) assuming that the sandstone layer (solid yellow) has a constant pressure. We compare this constant-pressure solution with the full solution from Fig. 2.6b, plotted in grey, with $\gamma = 2$, $\nu = 5$, $p_f^* = 0.5$ and $\sigma_T^* = 0.25$. The sandstone overpressure is fixed at the time-average of the periodic venting solution, $p_s^* \approx 0.4147$. We initiate the constant-pressure solution at the time of the first venting episode $t^* \approx 0.3917$.

2.F Venting period

The system tends towards a state of periodic venting, with a (dimensionless) time interval τ^* between episodes. We assume that this periodic state is achieved at late times of tectonic compression, where the sandstone pressure increases linearly with time. We note, however, that including the initial transient corresponding to tectonic compression does not affect the results of this section. Using the principle of superposition, we represent

this system as

$$p_s^* = \frac{\gamma+\nu}{1+\nu}t^* + \frac{\nu(\gamma-1)}{3(1+\nu)^2} - \sigma_T^* \sum_{n=1}^{N}\left(\frac{1}{1+\nu} + 2\nu\sum_{j=1}^{\infty}\frac{\exp\{-\xi_j^2(t^*-n\tau^*)\}}{\nu^2+\nu+\xi_j^2}\right), \tag{77}$$

for $N\tau^* < t^* < (N+1)\tau^*$. The sandstone pressure is periodic if $p_s^*(t^*+\tau^*) = p_s^*(\tau^*)$ for a constant venting period τ^*. We thus write

$$p_s^*(t^*+\tau^*) - p_s^*(t^*) = \frac{\gamma+\nu}{1+\nu}\tau^* - \frac{\sigma_T^*}{1+\nu} - 2\nu\sigma_T^*\sum_{j=1}^{\infty}\frac{\exp(-\xi_j^2 t^*)}{\nu^2+\nu+\xi_j^2}. \tag{78}$$

The right-most term in equation (78) tends to zero for large t^*, i.e., after the system has been venting for a duration that is much larger than the timescale of poroelastic pressure diffusion through the mudstone. Solving equation (78) in this large-time limit gives

$$\tau^* = \frac{\sigma_T^*}{\gamma+\nu}, \tag{79}$$

as the dimensionless venting period.

2.G Disequilibrium compaction

Disequilibrium compaction in this system will act to increase the total vertical stress σ_{zz}. We assume a constant rate of compressive vertical stress generation $-\dot{\sigma}_{zz}$ (with $\dot{\sigma}_{zz} \geq 0$) so from Terzaghi's principle,

$$\frac{\partial \sigma'_{zz}}{\partial t} = -\dot{\sigma}_{zz} + \alpha\frac{\partial p}{\partial t}. \tag{80}$$

Assuming sedimentation does not affect total stresses in the x and y directions,

$$(3\lambda+2\mu)\frac{\partial e}{\partial t} = -\dot{\sigma}_{zz} + 3\alpha\frac{\partial p}{\partial t}. \tag{81}$$

Using the storage equation and Darcy's law, we obtain

$$\frac{\mathrm{d}p_s}{\mathrm{d}t} = \frac{\alpha_s \dot{\sigma}_{zz}}{3\alpha_s^2 + S_s(3\lambda_s + 2\mu_s)} + \frac{3\lambda_s + 2\mu_s}{3\alpha_s^2 + S_s(3\lambda_s + 2\mu_s)} \frac{1}{h_s} \frac{k_m}{\eta} \frac{\partial p_m}{\partial z}\bigg|_{z=0} \qquad \text{at } z = 0, \quad (82a)$$

$$\frac{\partial p_m}{\partial t} = \frac{\alpha_m \dot{\sigma}_{zz}}{3\alpha_m^2 + S_m(3\lambda_m + 2\mu_m)} + \frac{3\lambda_m + 2\mu_m}{3\alpha_m^2 + S_m(3\lambda_m + 2\mu_m)} \frac{k_m}{\eta} \frac{\partial^2 p_m}{\partial z^2} \qquad \text{for } z \in [0, h_m]. \quad (82b)$$

In a similar way as done for tectonic compression, we introduce

$$D_m = \frac{k_m}{\eta} \frac{3\lambda_m + 2\mu_m}{3\alpha_m^2 + S_m(3\lambda_m + 2\mu_m)}, \qquad D_s = \frac{k_m}{\eta} \frac{3\lambda_s + 2\mu_s}{3\alpha_s^2 + S_s(3\lambda_s + 2\mu_s)}, \quad (83)$$

$$\Gamma_m = \frac{\alpha_m \dot{\sigma}_{zz}}{3\alpha_m^2 + S_m(3\lambda_m + 2\mu_m)}, \qquad \Gamma_s = \frac{\alpha_s \dot{\sigma}_{zz}}{3\alpha_s^2 + S_s(3\lambda_s + 2\mu_s)}. \quad (84)$$

This selection of parameters recovers the same governing equations as for tectonic compression, Eqns. (2.14) and (2.15). This allows us to provide solutions to both physical problems by solving one set of equations.

2.H Residual venting

If compression suddenly stops, venting may continue due to pressure diffusion. We take the example presented in Fig. 2.6b, and assert that compression stops at $t^* = 1.4$, plotted in Fig. 10. Five further venting episodes are observed before the mudstone and sandstone layers reach pressure equilibrium. The time interval between residual venting episodes increases exponentially as the mudstone pressure approaches p_f^*. The number of residual venting episodes will decrease by increasing the pressure drop in the mudstone per episode. This is achieved by increasing the tensile strength of the impermeable layer σ_T^* or decreasing the capacitance ratio ν. In some cases, no residual episodes are observed.

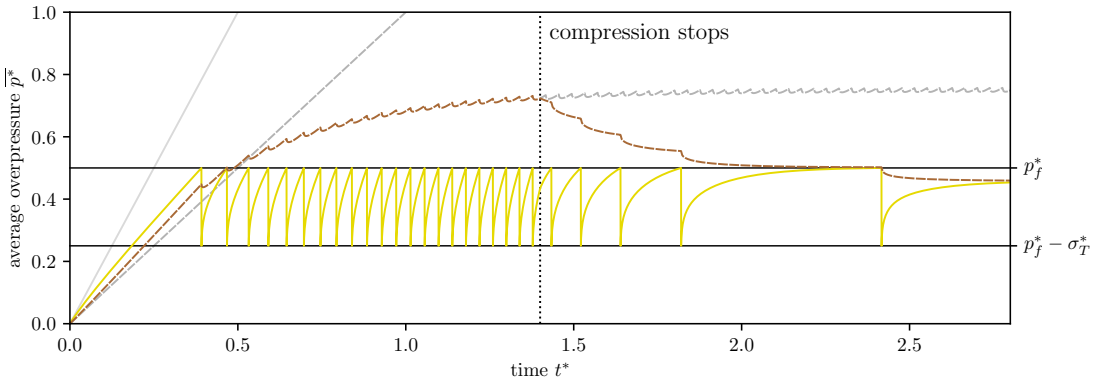

Figure 10: Average overpressure evolution of the sandstone (solid yellow) and mudstone (brown dashed) layers with compression stopping at $t^* = 1.4$. The solution for the mudstone with ongoing compression is plotted in grey. This example scenario follows Fig. 2.6b, with $\gamma = 2$, $\nu = 5$, $p_f^* = 0.5$ and $\sigma_T^* = 0.25$.

Statement of Authorship for joint/multi-authored papers for PGR thesis

To appear at the end of each thesis chapter submitted as an article/paper

The statement shall describe the candidate's and co-authors' independent research contributions in the thesis publications. For each publication there should exist a complete statement that is to be filled out and signed by the candidate and supervisor **(only required where there isn't already a statement of contribution within the paper itself).**

Title of Paper	Episodic, compression-driven fluid venting in layered sedimentary basins
Publication Status	☑Published □Accepted for Publication □Submitted for Publication □Unpublished and unsubmitted work written in a manuscript style
Publication Details	Kearney, L. M., MacMinn, C. W., Katz, R. F., Kirkham, C. & Cartwright, J. (2023), 'Episodic, compression-driven fluid venting in layered sedimentary basins', *Proceedings of the Royal Society A: Mathematical, Physical and Engineering Sciences* **479**(2274), 20220654. (doi:10.1098/rspa.2022.0654).

Student Confirmation

Student Name:	Luke Kearney		
Contribution to the Paper	Conceptualisation, data curation, formal analysis, investigation, methodology, visualisation, writing.		
Signature	L Kearney	Date	03/07/2024

Supervisor Confirmation

By signing the Statement of Authorship, you are certifying that the candidate made a substantial contribution to the publication, and that the description described above is accurate.

Supervisor name and title: Richard F Katz, Professor of Geodynamics		
Supervisor comments I confirm what Luke has written above is true. I certify that the candidate made a substantial contribution to the publication, and that the description described above is accurate.		
Signature	Date	3 July 2024

This completed form should be included in the thesis, at the end of the relevant chapter.

Chapter 3

Venting in the Levant Basin

The model, results and analysis presented in this chapter have been published in Kearney et al. (2024). This chapter constitutes a minor reformatting of that work to fit within the context of this thesis.

3.1 Introduction

Sedimentary successions often include high-permeability sandstone units enveloped by thick, low-permeability mudstone units. Because the surrounding mudstones can act as barriers to fluid leakage, these sandstones are often viewed as sealed reservoirs and therefore as targets for the large-scale sequestration of waste or storage of sustainable fuels (Krevor et al. 2023, Heinemann et al. 2021, Ringrose et al. 2021). However, fluid injection can pressurise such a reservoir to the point of triggering hydraulic fractures that breach the mudstone seal, enabling rapid depressurisation by fluid venting. This mechanism of sediment depressurisation has been recognised for several decades (Noble 1963, Cathles & Smith 1983, Roberts & Nunn 1995). It is generally believed that pressures below this failure threshold will dissipate by poroelastic diffusion through sealing

mudstones over thousands of years (Muggeridge et al. 2004, 2005, Chang et al. 2013*a*, Luo & Vasseur 2016). However, this slow depressurisation relies on the assumption that the mudstones themselves will remain at low pressure over these long timescales, whereas a variety of natural mechanisms are known to gradually pressurise the entire sedimentary column (Osborne & Swarbrick 1997). Luo & Vasseur (2016) showed that overpressured mudstones can, in theory, act as a pressure source rather than as a pressure sink, re-pressurising a sandstone reservoir after natural fluid venting. They proposed that this mechanism could fuel further episodes of venting. Kearney et al. (2023) recently developed a poroelastic model of episodic venting that supports and extends this basic concept. However, the predictions of these theoretical studies are difficult to test against observational evidence due to the long timescale associated with mudstone pressure evolution.

Here, we test the hypothesis that mudstones can act as sources of pressure, fuelling fluid venting from sedimentary basins. The geological record of episodic fluid venting in the Levant Basin (Fig. 3.1A) provides a rare opportunity to elucidate the role of mudstones in the pressure evolution of sedimentary basins. These vents release overpressure in localised fluid-expulsion events that transport fluid through kilometres of low-permeability rock via cylindrical conduits known as fluid-escape pipes (Cartwright et al. 2018). These pipes provide a high-permeability pathway to the surface, where they terminate as pockmarks, each recording a discrete episode of venting. Field observations of relict fluid-escape pipes consistently show evidence of fracturing (Huuse et al. 2005, Roberts et al. 2010, Løseth et al. 2011), suggesting that these pipes form by hydraulic fracturing (Cartwright & Santamarina 2015). Hydraulic fracturing typically requires the pore pressure to exceed the local compressive stress; indeed, drilling in a region of active venting has revealed near-lithostatic pore pressures (Reilly & Flemings 2010). Furthermore, the resulting pockmarks enable stratigraphic estimates of the time of each venting

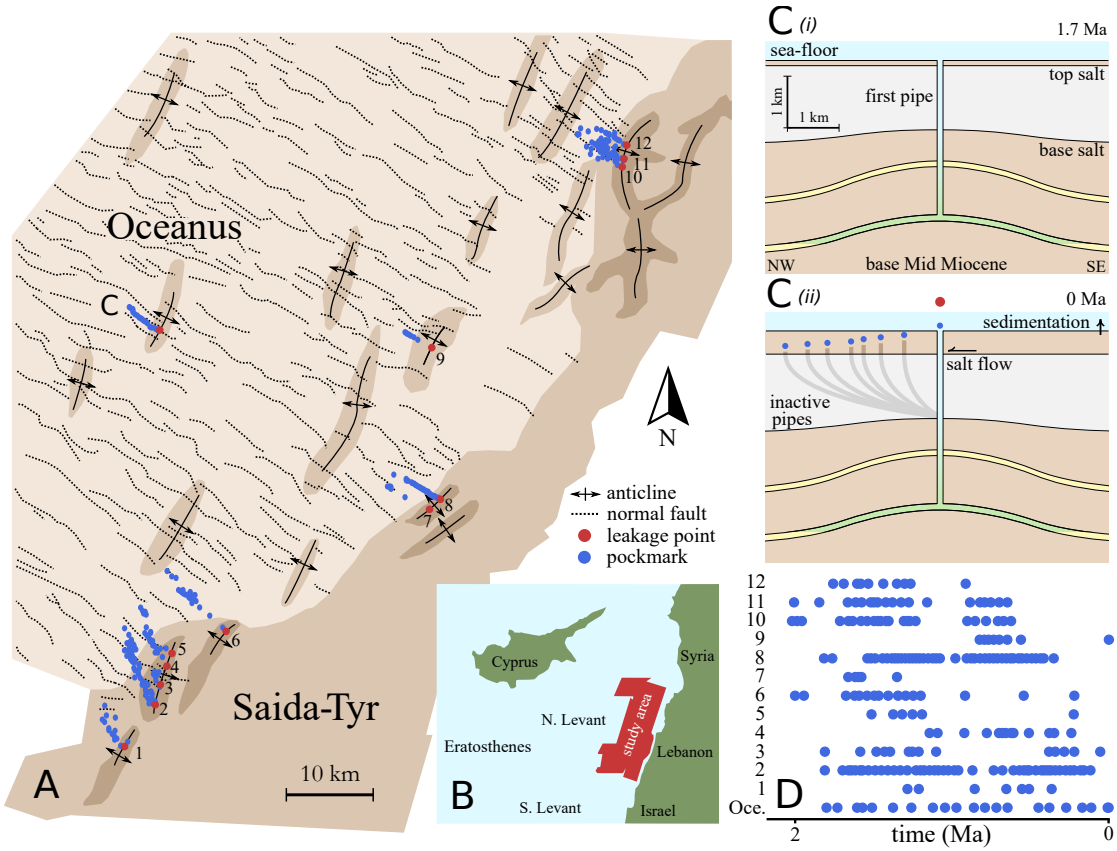

Figure 3.1: Fluid-escape pipe trails in the Levant Basin. (A) Overview of base-salt surface, showing sub-salt anticlines and the elevated margin platform, adjacent to the normally faulted deeper basin; adapted from Oppo et al. (2021), where lighter colours indicate larger depth. (B) Study area located on the North Levant Basin margin, offshore Lebanon. (C) General mechanism for fluid escape pipe trail formation, adapted from Cartwright et al. (2018), with (*i*) as the formation of the initial pipe at 1.7 Ma and (*ii*) as the present-day arrangement. (D) Pipe trails labelled 1–12 and Oceanus from panel (A) when corrected for relative salt translation rates (Oppo et al. 2021).

episode and thus constrain the rate of pressure recharge between episodes.

3.2 The Levant Basin

In the North Levant Basin, located in the Eastern Mediterranean (Fig. 3.1B), more than 300 fluid-escape pipes have been documented, recording episodic fluid venting from 13 fixed locations across the region. For one of these locations, named Oceanus (Fig. 3.1C),

Cartwright et al. (2021) calculated that the initiation of venting via hydraulic fracturing requires ∼30 MPa of overpressure. Tectonic compression and marginal uplift have been proposed as the main overpressuring mechanisms in the region (Oppo et al. 2021, Cartwright et al. 2021). The Levant Basin resides within a compressive tectonic regime stemming from the collision of the African and Eurasian plates. We estimate the strain at Oceanus to be less than 10% (Appendix 3.A). Within the Levant Basin is a ∼3 km-thick Oligo-Miocene clastic succession consisting of turbiditic sandstones of Late Oligocene to Early Miocene age that are encased by mudstone. Many of these sandstone reservoirs host biogenic methane accumulations in NE–SW trending anticlines. The Levant pipes source methane and water from these anticline reservoirs and terminate at the seafloor as pockmarks (Fig. 3.1A). The pipes penetrate through a ∼1.5 km-thick layer of salt deposited during the Messinian Salinity Crisis (Ryan 2009). Recent activity of the Levant Fracture System has been uplifting the eastern margin of the basin, leading to gravity-driven, basinward salt flow since ∼2 Ma, contemporaneous with the formation of pipes in the area.

Each pipe forms vertically but the basinward viscous flow of salt advects existing pipes away from their initial positions, such that subsequent venting from the same reservoir requires the formation of a replacement pipe (Fig. 3.1C). Repetition of this process leads to the 13 observed trails of pipes in the North Levant Basin (Cartwright et al. 2018, Oppo et al. 2021). Thus, each pipe trail records episodic fluid venting from a single reservoir, suggesting that these reservoirs are repeatedly repressurised. From the spatial distributions of pockmarks within each pipe trail, the time of formation of each pipe can be estimated (Fig. 3.1D) using the methods of Oppo et al. (2021) and Cartwright et al. (2021). These approaches reveal that for each trail, pipe formation typically occurs every ∼100 kyr. Since fluid-escape pipes record critical subsurface pressures, the Levant pipe trails enable us to distinguish between theories for pressure redistribution between

sedimentary layers. The timings of the pockmarks of the isolated Oceanus pipe trail are particularly well constrained as it is situated in a less tectonically-active region of the basin. Oceanus is therefore less susceptible to local stress changes that might affect the recharge mechanics. We thus focus our analysis on the Oceanus trail. The remaining 12 trails are distributed along the active basin margin and are used to extend our inferences from Oceanus to a more complex system.

To test the pressure-source hypothesis, we develop a novel stochastic model of reservoir pressure evolution and use it to invert the Levant pipe trail data under a Bayesian framework for model parameters such as the pressure-recharge rate. Using basic physical arguments, we then estimate recharge rates for each candidate overpressure mechanism and compare with the inferred rates. In particular, Kearney et al. (2023) showed that pressure diffusion from mudstones amplifies the rate of pressure recharge generated by tectonic compression. In mudstone-dominated basins like the Levant Basin, pressure-recharge rates can be amplified by a factor of $\sim$10. Therefore if this hypothesis is correct, then we expect that the inferred recharge rate is a factor of $\sim$10 greater than that predicted for tectonic compression alone.

3.3 Stochastic model of pressure evolution

We assume that a fluid-escape pipe forms via hydraulic fracturing when the pore pressure exceeds the critical fracture pressure p_f, which is the sum of the minimum horizontal compressive stress $\sigma_{\min}$ and tensile strength σ_T of the overlying mudstone (Price & Cosgrove 1990, Scandella et al. 2011),

$$p_f = \sigma_{\min} + \sigma_T, \tag{3.1}$$

where we take compression to be positive. Once venting begins, the pressure drops rapidly until the pathway closes, which we assume occurs when the pressure reaches $\sigma_{\min}$. Once closed, we expect fractures to self-seal via swelling and mineral precipitation (Bock et al. 2010). Roberts & Nunn (1995) predict fluid venting durations of order years, which may be considered instantaneous relative to recharge times, of order 100 kyrs. Over the latter timescale, pressure will become spatially uniform within a high-permeability reservoir. We thus assume that reservoir pressure depends on time only. For multiple venting episodes to be sourced from the same reservoir, the reservoir pressure must recharge between episodes. We consider generic pressure recharge at an average rate Γ, such that the corresponding time Δt between events is

$$\Delta t = \frac{p_f - \sigma_{\min}}{\Gamma} = \frac{\sigma_T}{\Gamma}. \tag{3.2}$$

Fractures exploit pre-existing rock weaknesses that change over geologic time, such that σ_T will vary between events. We model this variability by asserting that σ_T is a normally distributed random variable with mean $\overline{\sigma_T}$ and standard deviation s_T. Equation (3.2) then implies that $\Delta t \sim \mathcal{N}(\overline{\sigma_T}/\Gamma, s_T/\Gamma)$. Thus, the mean and standard deviation of inter-event times of a trail of pockmarks can be used to infer the underlying recharge rate.

As this is a limited dataset that has been produced by an inherently stochastic process, Bayesian inference is used to invert the pipe trail data for the full probability distribution of each parameter and quantify their uncertainty. Our prior estimates of each parameter $(\Gamma, \overline{\sigma_T}, s_T)$ are updated by evaluating the data with a likelihood function to recover the posterior probability distributions of each parameter. The likelihood function provides a statistical measure of model–data agreement by calculating the probability of observing the data given a set of model parameters. The simplicity of our physical model enables the likelihood function to be expressed analytically (Appendix 3.B). We apply a

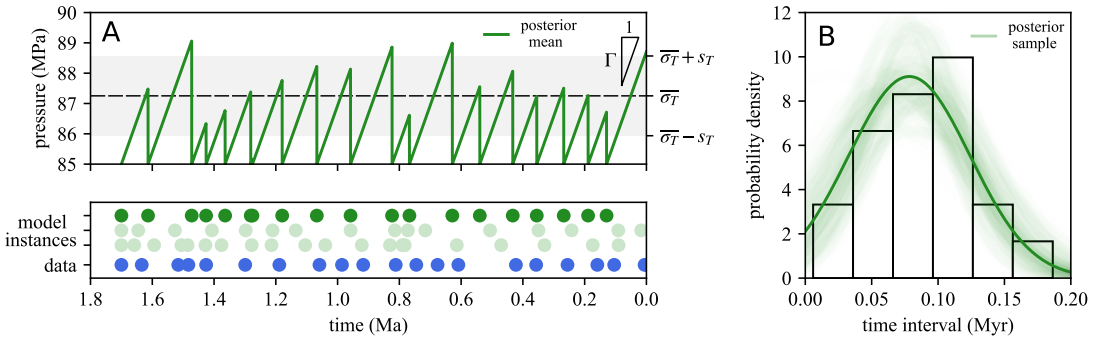

Figure 3.2: Results of Bayesian inference applied to the Oceanus pockmark trail. (a) Lower panel: Time-transformed pockmark data (blue) and stochastic model instances of venting history using inferred posterior mean (dark green) and sample parameters (translucent green). Upper panel: Stochastic instance of linearised pressure evolution using inferred posterior mean parameters (dark green), with pressures in excess of the minimum compressive stress corresponding to the mean tensile strength (dashed line) and corresponding to tensile strength values within one standard deviation of the mean (grey shaded area). (b) Posterior mean (dark green) and sample (translucent green) time interval distributions compared with Oceanus data.

conservative Gaussian prior for $\overline{\sigma_T} \sim \mathcal{N}(2.0, 1.0)$ MPa, since mudstone tensile strengths are typically a few MPa (Okland et al. 2002, Raaen et al. 2006); in particular, Roberts & Nunn (1995) predict a pressure drop of ∼2 MPa from venting. The posterior distributions of each parameter are sampled using the Metropolis-Hastings algorithm (Hastings 1970).

3.4 Oceanus pockmark trail

From the posterior distributions inferred for the isolated Oceanus trail (Appendix 3.D), we use the mean posterior parameter values as input for our stochastic model to simulate an instance of linearised pressure evolution (Fig. 3.2A). The qualitative similarity between the pockmark data and the model output is apparent (Fig. 3.2A, lower panel). For statistical comparison, we use samples from the posterior parameter distributions to calculate a range of posterior time interval distributions (Fig. 3.2B) that agree well with the data; variations between samples indicate the level of uncertainty in the inference. We note that as we have inferred the time-averaged recharge rate, this linearised pressure

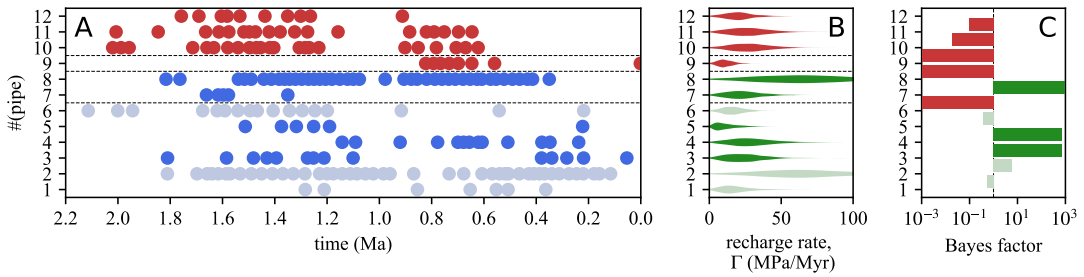

Figure 3.3: Results of Bayesian inference applied to Levant margin data. (a) Time-transformed data from Oppo et al. (2021). Dashed lines divide pipe clusters that are separated by more than 10 km. (b) Violin plot of posterior recharge rate distributions for each pipe trail. (c) Bayes factors of pairwise pipe analysis, where a value greater than one implies the coupled model is more likely.

evolution resembles the sawtooth behaviour that is predicted for recharge from tectonic compression only (Cartwright et al. 2021, Kearney et al. 2023). However, our statistical model makes no physical assumptions regarding the mechanism or dynamics of pressure recharge between venting episodes.

3.5 Levant margin pockmark trails

To the east of Oceanus are 12 other trails distributed along the basin margin (Oppo et al. 2021). Some of these trails originate from the same anticline, separated only by ∼1 km, and thus may be in hydraulic communication. To account for this possibility, we introduce pressure coupling as a feature of the model. For a coupled system of pipes, after any one pipe vents, the pressures of all pipes coupled to it reset to $\sigma_{\min}$ and a new σ_T is sampled for each. Therefore, the pipe that vents pressure temporarily inhibits any coupled pipes from venting. Consequently, the pipes in a coupled system form complementary pockmark series (Appendix 3.E). If a group of pipes are instead uncoupled, each pipe behaves independently. This contrast between independent and complementary venting behaviour is a qualitative diagnostic for pressure coupling.

To evaluate whether a pair of adjacent trails are coupled, we calculate the Bayes factor of the coupled model M_c and uncoupled model M_u (Appendix 3.B). The Bayes factor B_{cu} of two models M_c and M_u is given by the ratio of probabilities of observing the data $\mathbf{t}$ given each model, i.e.,

$$B_{cu} = \frac{\mathbb{P}(\mathbf{t} \mid M_c)}{\mathbb{P}(\mathbf{t} \mid M_u)}. \tag{3.3}$$

For example, if $B_{cu} > 1$ then M_c is preferred over M_u. Kass & Raftery (Kass & Raftery 1995) state that Bayes factors in the range 10–100 are 'strong' and above 100 are 'decisive'. We use this interpretation to assess the couplings of the pipe trails.

For the Levant margin pipe data (Fig. 3.3A), we infer similar recharge rates to those inferred for Oceanus, although mean recharge rates range up to 66 MPa/Myr for pipe trail 8 (Fig. 3.3B). Fig. 3.3C shows Bayes factors of pairwise analysis of adjacent trails. Triple-wise analysis leads to the same conclusions, but has been omitted to simplify the interpretation (Appendix 3.F). The model identifies all adjacent pipes that are greater than 10 km apart as decisively uncoupled. Furthermore, the inverted model indicates hydraulic connectivity between pipes 3, 4 and 5, each located along the same anticline, as well as trails 7 and 8 (Fig. 3.3C).

The inferences for pressure coupling are in agreement with the qualitative diagnostic behaviour. For example, the complementary venting behaviour of trails 3, 4 and 5 is visually evident. Conversely, trails 10, 11 and 12 are statistically inferred to be uncoupled and exhibit independent venting behaviour. Bayes factors with magnitudes between 0.1 and 10 exist for trail pairs {1, 2}, {2, 3} and {5, 6}, indicating a lack of preference for either coupling or not. We attribute this neutrality to features in the data that obscure the underlying recharge mechanics. These features are likely due to local stress variations caused by, for example, faulting. Nonetheless, since the majority of results

do have strong preferences to one model or another, we assert that the physical model captures the main pressure behaviour, both spatially and temporally. This result lends support to our statistical inferences of pressure-recharge rates.

3.6 Comparison of candidate overpressure mechanisms

Qualitatively, these venting observations could plausibly be explained by various overpressure mechanisms that have been previously proposed. We next show that these mechanisms, other than tectonic compression with pressure diffusion from mudstones, are inconsistent with our inferred recharge rates. Tectonic compression has been proposed as a major contributor to overpressure in the region (Cartwright et al. 2021). Previous numerical modelling of tectonic compression indicates that overpressures of 11–14 MPa in total can be generated from 10% strain (Obradors-Prats et al. 2016). At Oceanus, the strain accumulated since at least the Messinian Salinity Crisis, 5–6 Ma, is less than 10%. This implies a maximum recharge rate of ∼3 MPa/Myr from tectonic compression in isolation, which is insufficient to reproduce the observations (Fig. 3.4). However, Kearney et al. (2023) showed that pressure diffusion from mudstones amplifies the tectonic pressure-recharge rate in adjacent sandstones by a factor of $(1 + \nu/\gamma)$. This factor is termed the venting frequency multiplier and ν/γ is a ratio of dimensionless numbers that quantifies the relative effects of diffusion and compression. The dimensionless quantity γ measures the tectonic pressure-recharge rate of the sandstone relative to that of the mudstone, whereas ν is the hydraulic capacitance of the mudstone relative to that of the sandstone, where the hydraulic capacitance of a layer is the product of compressibility and thickness. Typically, $\nu/\gamma \gg 1$ in basins composed primarily of mudstone (Kearney et al. 2023), like the North Levant Basin. Due to the large uncertainty in

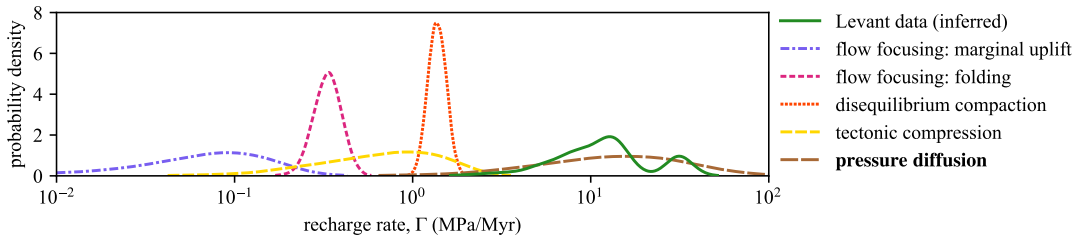

Figure 3.4: Comparison of pressure-recharge rates inferred from Levant pipe trail data with estimated recharge rates from candidate mechanisms.

mudstone permeabilities (Yang & Aplin 2007, Chang et al. 2013*a*), it might be expected that the uncertainty in the recharge rate from mudstone pressure diffusion would span many orders of magnitude. However, the venting frequency multiplier is independent of the mudstone permeability (Kearney et al. 2023). This result enables us to calculate the recharge rate from the combined effect of diffusion and compression using prior distributions of each constituent parameter, giving a probability distribution that largely overlaps with inferred recharge rates (Fig. 3.4).

Other candidate mechanisms predict much lower recharge rates than those inferred from the data (Fig. 3.4). The details of how we estimate the pressure-recharge rates from each mechanism can be found in Appendix 3.G. Oppo et al. (2021) proposed that marginal uplift generates significant overpressures at the basin margin by driving lateral fluid migration from the highly overpressured deep basin. If pressure is transferred laterally along a connected, high-permeability sandstone unit, the venting periods would be several orders of magnitude lower than are observed. However, it is likely that there is poor lateral reservoir connectivity in the area (Cartwright et al. 2021) and our analysis above supports this idea, indicating that many relatively nearby pipes are likely to be hydraulically independent (Fig. 3.3C). As a result, the only pathway for lateral fluid migration is via mudstones, thus implicitly requiring pressure diffusion from mudstones for reservoir recharge. Marginal uplift may also generate overpressure by flow focusing

(Flemings et al. 2002), though this mechanism likely produces insufficient recharge rates (Fig. 3.4). Flow focusing due to fold amplification (Flemings et al. 2002) generates overpressures at a rate of less than ∼1 MPa/Myr. Furthermore, hydrocarbon generation likely cannot generate the required recharge rate since the additional head required from buoyancy is greater than ∼1 km/Myr and most thermogenic gas generation was likely complete by 5–6 Ma (Al-Balushi et al. 2016). We cannot rule out the possibility of weak pressure recharge from biogenic gas generation, though petroleum systems modelling of the region favours biogenic gas accumulation via lateral migration from the deep basin (Bou Daher et al. 2016, Ghalayini et al. 2018, Nader et al. 2018). However, due to poor lateral reservoir connectivity, lateral gas migration is rate-limited by pressure diffusion (as for the case of marginal uplift). While lateral transfer produces insufficient recharge rates, vertical pressure transfer from a deeper reservoir along faults or fractures has been associated with fluid venting in other regions (see Grauls & Baleix 1994, Tingay et al. 2007, Cathles 2019). In the Levant Basin, however, there is no evidence to support vertical fluid migration. Moreover, vertical transfer cannot explain the observed regular periodicity of venting. Disequilibrium compaction due to the small, post-salt sediment accumulation of ∼300 m (Cartwright et al. 2021) creates a negligible pressurisation rate of ∼1 MPa/Myr. Sea-level fluctuations may trigger venting episodes (see Scandella et al. 2011), though this mechanism alone provides no net pressure recharge.

The venting observations from the Levant fluid-escape pipe trails are consistent with predictions deriving from the hypothesis that pressure diffusion from mudstones fuels episodic venting in the region. Therefore, the Levant pipe trails provide strong spatiotemporal evidence supporting this hypothesis. In doing so, the pipe trails support the more general idea that pressure diffusion from mudstones plays an important role in pressure redistribution between sedimentary layers and provide observational evidence that was previously lacking from the theoretical literature (e.g., Muggeridge et al. 2004,

2005, Luo & Vasseur 2016, Kearney et al. 2023). It is likely that tectonic compression and marginal uplift were the main mechanisms for slowly pressurising the basin to near-lithostatic by ∼2 Ma. This pressurisation initiated basin-wide fluid venting by hydraulic fracturing, sourced by high-permeability, pre-salt sandstone reservoirs. Tectonic compression continued to slowly pressurise (∼3 MPa/Myr) the entire sedimentary succession while poroelastic pressure diffusion from mudstones recharged the sandstone reservoirs back to failure at a rate of ∼30 MPa/Myr. This combination of pressure diffusion and tectonic compression, with minor contributions from hydrocarbon generation and disequilibrium compaction, led to episodic fluid venting with a typical venting period of ∼100 kyr. While this is not a universal result for pipes in any basin, pressure diffusion exists wherever the corresponding reservoir unit is encased by highly overpressured, low-permeability rocks. Furthermore, the effect of pressure diffusion is intensified in sedimentary basins composed mostly of mudstone (Kearney et al. 2023), where fluid venting phenomena are commonly observed (Cartwright & Santamarina 2015). In many cases, liquefied mudstone is vented in addition to basinal fluids (e.g., Cartwright et al. 2023). The diverse roles of mudstones in pressure-driven, focused fluid venting provides an impetus to improve our mechanistic models of such venting phenomena.

3.7 Broader implications

Because understanding subsurface pressure is crucial to prevent unwanted fluid leakage, these results have wider implications for risk assessment during borehole drilling and the sequestration of waste such as CO_2. Fluid leakage resulting from reservoir pressurisation by mudstones may be a risk in a broad range of geological settings, requiring only that the mudstones are overpressured relative to the reservoir. This overpressure can be retained even after several episodes of fluid venting (Kearney et al. 2023), and can be

generated by various means, not limited to horizontal compression. Indeed, Kearney et al. (2023) show that disequilibrium compaction (i.e., vertical compression) leads to mathematically equivalent behaviour. Therefore, even tectonically inactive regions like passive margins are prone to episodic venting if they are subjected to, for example, high sedimentation rates. Indeed, fluid-escape pipes are commonly observed in passive margin settings (Cartwright & Santamarina 2015). Passive margins also provide the largest and likely most cost-effective large-scale CO_2 storage resource (Ringrose & Meckel 2019). Therefore, fluid-escape pipes may pose a significant threat to offshore storage projects.

This work highlights the importance of considering pressure diffusion from mudstones when assessing reservoir overpressures. This is especially true for sequestration sites with evidence of previous fluid venting, like the Sleipner field (Arts et al. 2004, Cavanagh & Haszeldine 2014). While the relict fluid-escape pipes at Sleipner are unlikely to be a result of CO_2 injection (Cavanagh & Haszeldine 2014), they serve as an example of the risks to containment associated with fluid venting. Although the dissolution of injected CO_2 can act to depressurise a storage reservoir (Akhbari & Hesse 2017), evidence from a natural CO_2 reservoir suggests that the rate of depressurisation from CO_2 dissolution is $\sim$1 MPa/Myr (Sathaye et al. 2014). This is much less than the recharge rates from pressure diffusion that we infer in the Levant Basin, suggesting that CO_2 dissolution is unlikely to prevent leakage in regions where pressure diffusion from mudstones is active. Thus, for storage projects in regions with pressurised mudstones, our results indicate that reservoir pressure monitoring over several millenia may be required to ensure containment.

Appendices

3.A Oceanus strain

We estimate the horizontal strain at the Oceanus pipe trail from the depth-converted cross-section in Cartwright et al. (2021). We do this by measuring the arc length of one of the folded Mid-Miocene sandstone layers (Fig. 5). We assume that this layer was initially horizontal, such that the arc length of the layer measures the initial horizontal extent of this section L_0. We calculate the horizontal strain by comparing this initial horizontal extent to the present-day horizontal extent of this layer L, using

$$e_{xx} = -\frac{L - L_0}{L_0}, \tag{4}$$

where compressive strains are taken to be positive. This gives a horizontal strain of 2% at Oceanus. While the majority of strain in the region is accommodated by folding, we recognise that this calculation does not account for strain accommodated by faulting or volumetric compression. Further uncertainty in this calculation stems from potential errors in the depth migration of the seismic data. Accounting for this uncertainty conservatively, we assert that the maximum possible horizontal strain at Oceanus is 10%.

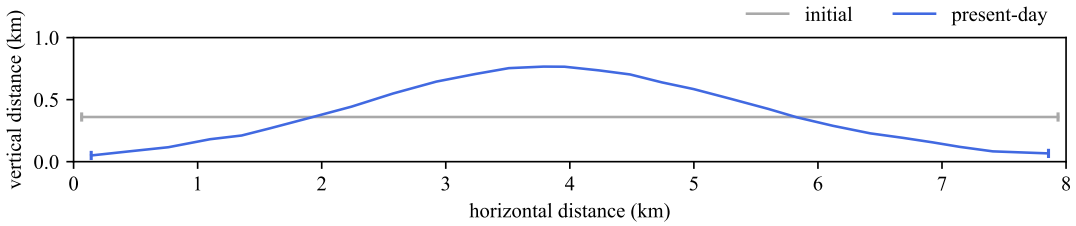

Figure 5: Comparison of the present-day geometry of the folded sandstone layer at Oceanus (blue curve) with its likely initial state (grey curve), i.e., before the onset of tectonic compression. The horizontal strain at Oceanus can be calculated by comparing the horizontal extent of the present-day fold L with the horizontal extent of its initial unfolded state L_0.

3.B Bayesian inference

One can use a Bayesian framework to invert for the parameters. Bayes' theorem is given by

$$\mathbb{P}(\theta \,|\, \mathbf{x}) = \frac{\mathbb{P}(\mathbf{x} \,|\, \theta)\mathbb{P}(\theta)}{\mathbb{P}(\mathbf{x})} = \frac{\mathbb{P}(\mathbf{x} \,|\, \theta)\mathbb{P}(\theta)}{\int_\Theta \mathbb{P}(\mathbf{x} \,|\, \theta)\mathbb{P}(\theta)\mathrm{d}\theta}, \tag{5}$$

or in words,

$$\text{posterior} = \frac{\text{likelihood} \times \text{prior}}{\text{evidence}}. \tag{6}$$

Maximum-likelihood estimation methods such as ordinary least-squares aim to maximise the likelihood, the probability that the model generates the data. This is equivalent to maximising the posterior under the assumption of a uniformly distributed prior. However, Bayesian methods place a prior distribution on the parameters and calculates the posterior distribution using the observed data. We achieve the statistical equivalent to regularisation by enforcing these prior distributions.

3.B.1 Likelihood function

Given a model, the likelihood function is the joint probability of the observed data. Here, the observed data is the set of all venting times $\mathbf{t} = \{t_n\}_{n=1}^N$. The likelihood function can be decomposed in the following way:

$$f(\{t_n\}_{n=1}^N) = \prod_{n=1}^{N} f(t_n \,|\, \mathcal{H}_{t_n}), \tag{7}$$

where f is the probability density and the history $\mathcal{H}_{t_n}$ is the set of all event times until (but not including) t_n. Since the proposed model asserts that the pressure resets to $\sigma_{\min}$ after each event, the pressure 'memory' of the system extends only from the most recent event so $\mathcal{H}_{t_n} = t_{n-1}$. We can therefore write

$$f(\{t_n\}_{n=1}^N) = \prod_{n=1}^{N} f(\Delta t_n), \tag{8}$$

where $\Delta t_n = t_n - t_{n-1}$. For coupled systems we must additionally consider the mark of each pipe κ, denoting where each event originated. It can be shown that for a set of K coupled pipes,

$$f(\{t_n, \kappa_n\}_{n=1}^N) = \prod_{n=1}^{N} f_{\kappa_n}(\Delta t_n) \prod_{k=1}^{K} \Big[1 - F_k(\Delta t_n)\Big]^{1-\delta_{\kappa_n,k}}, \tag{9}$$

where f_k and F_k are the uncoupled probability and cumulative density functions of pipe $\kappa = k$, respectively, and δ is the Kronecker delta. We utilise these likelihood functions to model the probability density of any coupling configuration of pipes.

3.B.2 Bayes factor

To evaluate whether a pair of adjacent trails are coupled, we calculate the Bayes factor of the coupled model M_c and the uncoupled model M_u. The Bayes factor B_{cu} of two models M_c and M_u is given by the ratio of probabilities of observing the data $\mathbf{t}$ given each model, i.e,

$$B_{cu} = \frac{\mathbb{P}(\mathbf{t} \mid M_c)}{\mathbb{P}(\mathbf{t} \mid M_u)}. \tag{10}$$

For example, if $B_{cu} > 1$ then M_c is preferred over M_u. Here, M_c is the coupled model and M_u is the uncoupled model. Kass & Raftery (1995) state that Bayes factor magnitudes between 10-100 are 'strong' and above 100 are 'decisive'. We define a new parameter $\phi \in \{0, 1\}$ such that $\phi = 1$ indicates the coupled model M_c and $\phi = 0$ indicates the uncoupled model M_u. The Bayes factor can be rewritten in terms of ϕ as

$$B_{cu} = \frac{\mathbb{P}(\mathbf{t} \mid \phi = 1)}{\mathbb{P}(\mathbf{t} \mid \phi = 0)}. \tag{11}$$

In this form, the Bayes factor can be calculated with MCMC methods. We assume a prior distribution for $\phi \sim \text{Bernoulli}(\frac{1}{2})$. Using the likelihood functions of the coupled and uncoupled models, the posterior distribution $\mathbb{P}(\mathbf{t} \mid \phi)$ can be sampled (using e.g., the Metropolis-Hastings algorithm) from which the Bayes factor can be calculated.

3.C Inversion tests

Inversions are performed on synthetic data to test the accuracy and sensitivity of our inversion method. Here, we apply uniform prior distributions to assess the effectiveness of the likelihood function alone. We nondimensionalise the parameters $(\Gamma, \overline{\sigma_T}, s_T)$ to $\Gamma^* = \Gamma/\overline{\sigma_T}$ and $s_T^* = s_T/\overline{\sigma_T}$.

3.C.1 One pipe

Inversions of a single pipe trail perform well if the true $s_T^* < 1$. When $s_T^* > 1$, the distribution of Δt begins to be significantly truncated for $\Delta t < 0$ and tends towards a uniform distribution for larger s_T^*. Henceforth, we analyse simulations with $s_T^* < 1$.

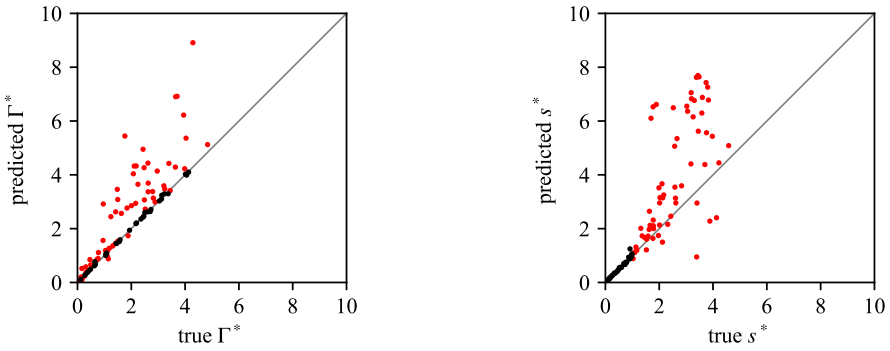

Figure 6: Showing inversion results for simulated synthetic data. Each simulation uses a pair of values for Γ^* and s_T^* to generate a sequence of 1000 venting times. (a) Predicted mean Γ^* versus the true assigned Γ^* for that simulation. (b) Predicted mean s_T^* versus the true assigned s_T^* for that simulation. Black points represent inversion results from simulations with true $s^* < 1$ and red points with true $s^* > 1$.

3.C.2 Two pipes

We similarly perform inversions on synthetic data from simulations of two uncoupled pipes, shown in Fig. 7, and two coupled pipes, shown in Fig. 8. In these figures, each point represents results from Bayesian inversion applied to a simulated sequence of 40 venting times from two pipes. The number of venting times was chosen to investigate the level of uncertainty in the inversion for a pair of Levant pipe trails, which each typically comprise ∼20 venting times. In each case, the predicted Γ^* is in agreement with the true value; the uncertainty in the inference of s^* increases with increasing true s^*.

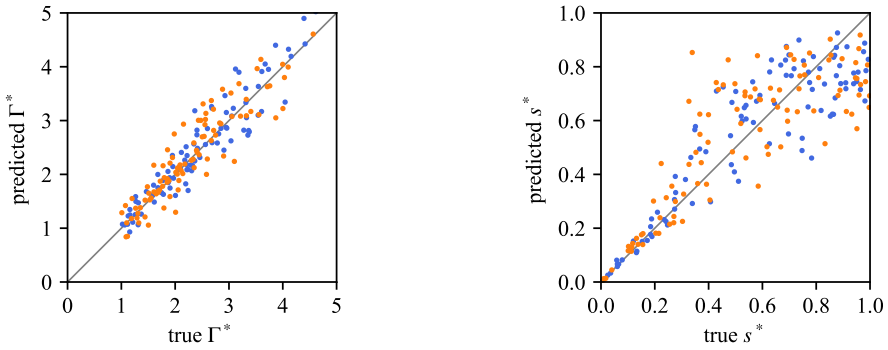

Figure 7: Showing inversion results for simulated synthetic data of two uncoupled pipes. Each simulation uses a pair of values for Γ^* and s_T^* to generate 40 events in total. The inversion of each simulation generates two points, one for pipe 1 (blue) and one for pipe 2 (orange). (a) Predicted mean Γ^* versus the true assigned Γ^* for that simulation. (b) Predicted mean s_T^* versus the true assigned s_T^* for that simulation.

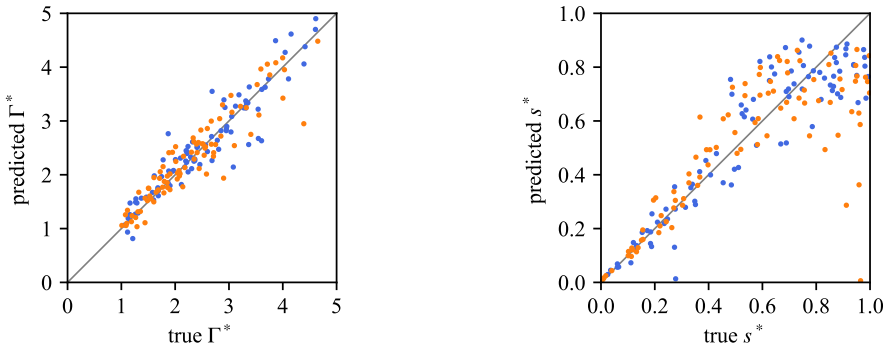

Figure 8: Showing inversion results for simulated synthetic data of two coupled pipes. Each simulation uses a pair of values for Γ^* and s_T^* to generate 40 events in total. The inversion of each simulation generates two points, one for pipe 1 (blue) and one for pipe 2 (orange). (a) Predicted mean Γ^* versus the true assigned Γ^* for that simulation. (b) Predicted mean s_T^* versus the true assigned s_T^* for that simulation.

3.D Oceanus posterior distributions

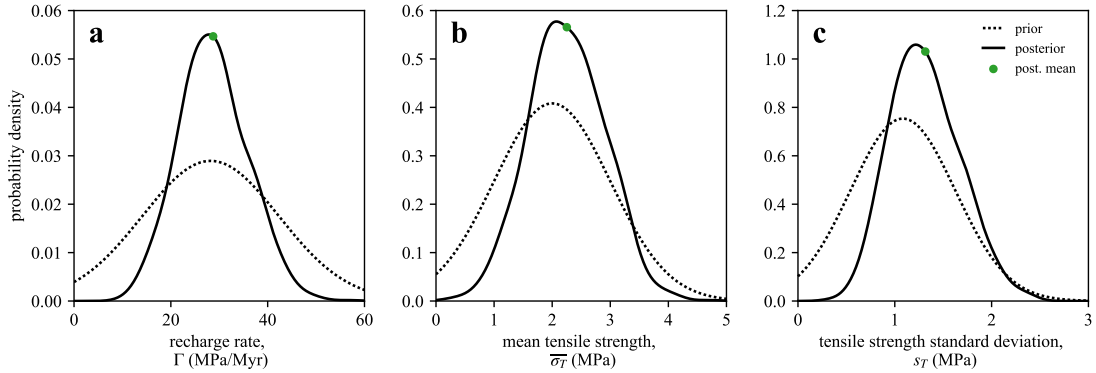

Figure 9: Results of Bayesian inference applied to Oceanus trail. (a) Prior and posterior distributions of the recharge rate, Γ, with posterior mean 28 MPa/Myr. (b) Prior and posterior distributions of the mean tensile strength, $\overline{\sigma_T}$ with posterior mean 2.3 MPa. (c) Prior and posterior distributions of the tensile strength standard deviation, s_T with posterior mean 1.3 MPa.

3.E Pressure coupling

Whether pipe trails are coupled or not leads to profound changes in the resulting pattern of pockmarks. Fig. 10 demonstrates this clearly with a pair of pipes in each scenario. The uncoupled pipes have independent pressure histories hence the pattern of pockmarks leads to an alternation between each pipe venting. In contrast, for a system of two coupled pipes, after either pipe vents both pressures reset to $\Delta p = 0$ and sample new tensile strengths. Therefore, if one pipe vents, the other is temporarily inhibited from venting. This leads to a complementary pockmark series, where the periods of quiescence of one pipe correspond to activity in the second pipe. In comparison to the field data (Fig. 3.1d), uncoupled behaviour is exhibited by pipe trails 10, 11 and 12, while coupled behaviour is most pronounced in trails 3, 4 and 5.

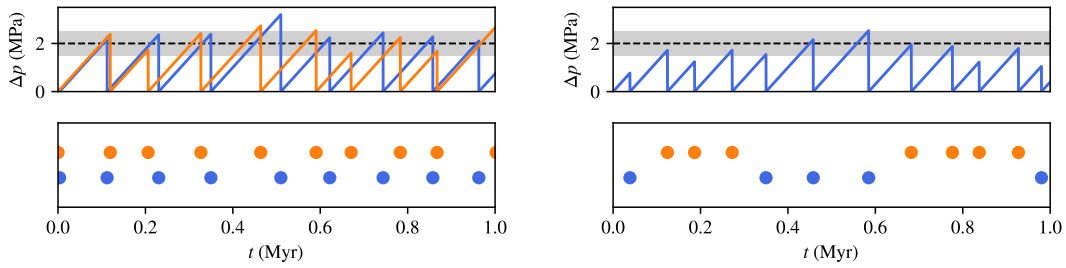

Figure 10: Stochastic realisations of two pipes, each with $\Gamma = 20$ MPa/Myr, $s = 0.5$ MPa and $\overline{\sigma_T} = 2$ MPa. Top plots show pressure evolution, where $\Delta p = p - \sigma_{\min}$ and bottom plots show the corresponding pockmark patterns. Left: uncoupled, right: coupled. Dashed horizontal lines indicate the mean tensile strength $\overline{\sigma_T}$; grey bars contain tensile strengths within one standard deviation of the mean ($\overline{\sigma_T} \pm s_T$).

3.F Triple-wise inference

Figure 11 shows the results of Bayesian inference applied to each adjacent triple of pipes, e.g., $\{1, 2, 3\}$, $\{2, 3, 4\}$, etc. Recharge rates and Bayes factors for each pipe are obtained by averaging the results from each associated triple.

For a given triple of pipes, there are four possible combinations of hydraulic coupling (excluding non-adjacent couplings) and thus four models to consider. Given these four models, there are six possible Bayes factors. To simplify our analysis, and to more directly compare with the results from the pair-wise analysis, we desire the Bayes factor given by equation (3.3) for each pair of pipe trails. As an example, for the coupling between pipes 2 and 3, denoted by $\phi_{23} \in \{0, 1\}$, we therefore seek to calculate

$$B_{cu} = \frac{\mathbb{P}(\mathbf{t} \mid \phi_{23} = 1)}{\mathbb{P}(\mathbf{t} \mid \phi_{23} = 0)}. \tag{12}$$

To calculate this Bayes factor from the triple of pipes $\{1, 2, 3\}$, we marginalise over the coupling between pipes 1 and 2, denoted as ϕ_{12}, to give

$$\begin{aligned} \mathbb{P}(\mathbf{t}_{123} \mid \phi_{23} = 1) = \mathbb{P}(\mathbf{t}_{123} \mid \phi_{12} = 0, \phi_{23} = 1)\mathbb{P}(\phi_{12} = 0) \\ + \mathbb{P}(\mathbf{t}_{123} \mid \phi_{12} = 1, \phi_{23} = 1)\mathbb{P}(\phi_{12} = 1), \end{aligned} \tag{13}$$

where $\mathbf{t}_{ijk}$ denotes the venting data of pipes i, j, k. We enforce unbiased prior probabilities for each model, i.e., $\mathbb{P}(\phi_{12} = 0) = \mathbb{P}(\phi_{12} = 1) = \frac{1}{2}$. Therefore by considering the triple of pipes $\{1, 2, 3\}$, the Bayes factor is

$$B_{cu}^{\{1,2,3\}} = \frac{\mathbb{P}(\mathbf{t}_{123} \mid \phi_{12} = 0, \phi_{23} = 1) + \mathbb{P}(\mathbf{t}_{123} \mid \phi_{12} = 1, \phi_{23} = 1)}{\mathbb{P}(\mathbf{t}_{123} \mid \phi_{12} = 0, \phi_{23} = 0) + \mathbb{P}(\mathbf{t}_{123} \mid \phi_{12} = 1, \phi_{23} = 0)}. \tag{14}$$

Similar results to equations (13), (14) for the coupling ϕ_{23} are obtained from the data $\mathbf{t}_{234}$. We then approximate the Bayes factor that considers all four relevant trails $\{1, 2, 3, 4\}$ by averaging the Bayes factors from triples $\{1, 2, 3\}$ and $\{2, 3, 4\}$ using the geometric mean

$$\log B_{cu}^{\{1,2,3,4\}} \approx \tfrac{1}{2}(\log B_{cu}^{\{1,2,3\}} + \log B_{cu}^{\{2,3,4\}}). \tag{15}$$

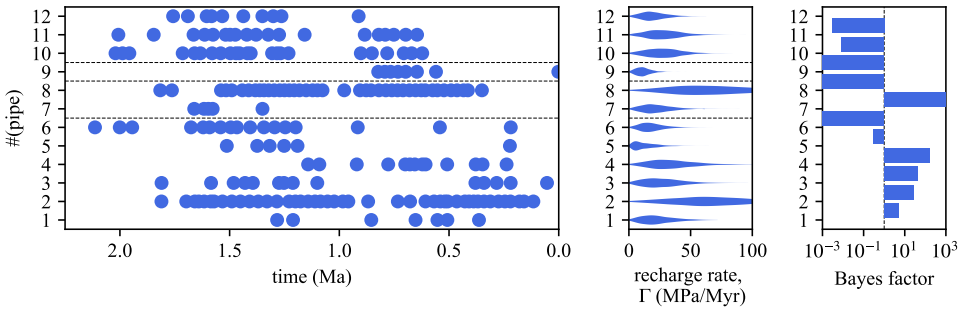

Figure 11: Results of triple-wise Bayesian inference applied to Levant margin data. (a) Time-transformed data from Oppo et al. (2021). Dashed lines divide pipe clusters that are separated by more than 10 km. (b) Violin plot of posterior recharge rate distributions for each pipe trail. (c) Bayes factors of pairwise pipe analysis, where a positive value implies the coupled model is more likely.

3.G Candidate overpressure mechanisms

3.G.1 Tectonic compression

The model for tectonic compression developed by Kearney et al. (2023) is highly simplified; to ensure an accurate estimation of Γ_s we use results from previous numerical modelling of tectonic compression (Obradors-Prats et al. 2016). Obradors-Prats et al. (2016) estimate overpressures between 11–14.2 MPa from 10% strain at different rates, implying that 1.1–1.4 MPa of overpressure is generated per % strain. Using seismic imaging, we estimate the strain at Oceanus to range from 1% to 10%, which we assume has been accumulating since the Messinian Salinity Crisis, between 5 Ma to 6 Ma.

Parameter	**Description**	**mean**	**std. dev.**	**min.**	**max.**	**Reference**
$\Delta P/\Delta e_{xx}$ (MPa)	overpressure per % strain	1.2	0.2	0.5	2.0	Obradors-Prats et al. (2016)
Δe_{xx}	horizontal strain	5	2	1	10	
Δt_e (Myr)	strain duration	5.5	0.5	5	6	Cartwright et al. (2021)

Parameter	**Description**	**mean**	**std. dev.**	**min.**	**max.**	**Reference**
h_s (m)	sandstone thickness	150	50	50	200	Cartwright et al. (2021),
h_m (m)	mudstone thickness	2500	250	2000	3000	
α_s	sandstone Biot coefficient	0.62	0.17	0.38	0.83	Ge & Garven (1992)
α_m	mudstone Biot coefficient	0.68	0.35	0.30	0.98	
v_s	sandstone Poisson ratio	0.24	0.04	0.20	0.30	
v_m	mudstone Poisson ratio	0.25	0.05	0.15	0.30	
K_s (GPa)	sandstone bulk modulus	18	8	8	30	
K_m (GPa)	mudstone bulk modulus	15	17	5	33	
ϕ_s	sandstone porosity	0.22	0.01	0.19	0.24	Ortega et al. (2018)
ϕ_m	mudstone porosity	0.20	0.05	0.05	0.30	Yang & Aplin (2007)
$\log_{10} k_m$ ($\log_{10}$ m^2)	(log) mudstone permeability	-19	0.5	-22	-18	
η (mPa s)	water viscosity	0.3	0.1	0.1	0.5	Abramson (2007)
c_ℓ (10^{-11} Pa^{-1})	water compressibility	4.0	0.1	3.7	4.3	Fine & Millero (1973)

Parameter	**Description**	**mean**	**std. dev.**	**min.**	**max.**	**Reference**
θ (°)	tilt angle	3	1	0	5	Cartwright et al. (2021)
ρ_m (kg/m^3)	mudstone density	2350	100	2200	2600	
ρ_ℓ (kg/m^3)	water density	1060	100	1000	1200	
L_s (m)	sandstone length	5000	1000	500	10000	
Δt_u (Myr)	uplift duration	2	0.5	1	3	Oppo et al. (2021)

3.G.2 Pressure diffusion

3.G.3 Flow focusing: marginal uplift

Flow focusing due to marginal uplift can lead to overpressure generation. For a flat sandstone of length L_s in a mudstone with pressure gradient $\rho_m g$, uplifting one side by $\mathrm{d}z$ leads to an equilibration of pressures at the new sandstone centroid, $\mathrm{d}z/2$ (Flemings et al. 2002). Therefore, tilting the sandstone by an angle θ gives an overpressure of

$$\Delta p = \tfrac{1}{2}(\rho_m - \rho_\ell) g L_s \sin\theta, \tag{16}$$

at the top of the reservoir. The corresponding overpressure rate is

$$\frac{\partial p}{\partial t} = \tfrac{1}{2}(\rho_m - \rho_\ell) g L_s \dot{\theta} \cos\dot{\theta} t, \tag{17}$$

where $\dot{\theta}$ is the angular tilting rate. For simplicity of interpretation, we take the time-average of this overpressure rate, given by

$$\Gamma = \frac{(\rho_m - \rho_\ell) g L_s \sin\theta}{2\Delta t_u}. \tag{18}$$

3.G.4 Flow focusing: folding

If the sandstone reservoir has a growing parabolic profile, then the overpressure rate generated at the crest by flow focusing is given by (Flemings et al. 2002)

$$\Gamma = \frac{2(\rho_m - \rho_\ell) g \Delta h_f}{3\Delta t_f} \tag{19}$$

Parameter	**Description**	**mean**	**std. dev.**	**min.**	**max.**	**Reference**
ρ_m (kg/m^3)	mudstone density	2350	100	2200	2600	Cartwright et al. (2021)
ρ_ℓ (kg/m^3)	water density	1060	100	1000	1200	
h_s (m)	sandstone thickness	150	50	50	200	
Δt_f (Myr)	folding duration	5.5	0.5	5	6	

where the factor of 2/3 appears because the sandstone and mudstone pressures equilibrate at $\Delta h/3$.

3.G.5 Disequilibrium compaction

Disequilibrium compaction due to post-salt sedimentation contributes to overpressure in the North Levant Basin. For a change in post-salt sediment thickness Δh_{ps} over a time Δt_c with density ρ_{ps}, the maximum overpressure rate is given by the change in total stress,

$$\Gamma = \frac{\rho_{ps} g \Delta h_{ps}}{\Delta t_c} \tag{20}$$

Parameter	Description	mean	std. dev.	min.	max.	Reference
ρ_{ps} (kg/m^3)	post-salt sediment density	2000	100	1800	2500	Cartwright et al. (2021)
h_{ps} (m)	post-salt sediment thickness	355	25	300	400	
Δt_c (Myr)	duration	5	0.5	4	6	

Statement of Authorship for joint/multi-authored papers for PGR thesis

To appear at the end of each thesis chapter submitted as an article/paper

The statement shall describe the candidate's and co-authors' independent research contributions in the thesis publications. For each publication there should exist a complete statement that is to be filled out and signed by the candidate and supervisor **(only required where there isn't already a statement of contribution within the paper itself).**

Title of Paper	Episodic fluid venting from sedimentary basins fueled by pressurized mudstones
Publication Status	☑Published □Accepted for Publication □Submitted for Publication □Unpublished and unsubmitted work written in a manuscript style
Publication Details	Kearney, L. M., Katz, R. F., MacMinn, C. W., Kirkham, C. & Cartwright, J. (2024), 'Episodic fluid venting from sedimentary basins fueled by pressurized mudstones', *Proceedings of the National Academy of Sciences* **121**(8), e2312152121. (doi: 10.1073/pnas.2312152121).

Student Confirmation

Student Name:	Luke Kearney		
Contribution to the Paper	Designed research, performed research (developed model, wrote code), analysed data, wrote manuscript.		
Signature	L Kearney	Date	03/07/2024

Supervisor Confirmation

By signing the Statement of Authorship, you are certifying that the candidate made a substantial contribution to the publication, and that the description described above is accurate.

Supervisor name and title: Richard F Katz, Professor of Geodynamics		
Supervisor comments I confirm what Luke has written above is true. I certify that the candidate made a substantial contribution to the publication, and that the description described above is accurate.		
Signature	Date	3 July 2024

This completed form should be included in the thesis, at the end of the relevant chapter.

Chapter 4

Subsurface sediment remobilisation during venting

4.1 Introduction

Mud volcanoes are a key avenue for the natural relief of pressure and emission of greenhouse gases from sedimentary basins globally. They produce massive effusions of hydrocarbon-rich mud, and the resulting mud edifice can present a significant hazard to people and infrastructure. This hazard is most strikingly exemplified by the Lusi eruption in Indonesia, which has been ongoing since 2006 at an economic cost of billions of USD (Tingay et al. 2015, 2018). Estimates of the degree of hazard depend on the quantitative forecasting of the rate and duration of eruption. Current forecasts carry significant uncertainty as long-term measurements of eruption rates and durations are scarce (Davies et al. 2011, Rudolph et al. 2011); however, they are a direct consequence of the evolution of the sources of fluid and mud at depth.

In many cases, the fluids are sourced from a separate, deeper stratigraphic layer than

the mud (Bristow et al. 2000, Kopf et al. 2003, Planke et al. 2003, Deville et al. 2010, Davies et al. 2011). As a simple example, the Lusi mud volcano comprises a deep source of overpressured fluid that drives upward flow through a mudstone unit, remobilising it (Davies et al. 2011). In other regions, however, mud and fluids are extracted from multiple separate stratigraphic layers. This may include the cannibalisation of buried mud edifices to form later extrusions (Planke et al. 2003, Deville et al. 2010). This distributed nature of the source region—and the lack of information about the source of fluids in particular—makes it difficult to constrain the mechanisms by which these materials are remobilised and expelled.

A recent high-resolution, three-dimensional seismic survey in the Nile Deep Sea Fan provides statistically robust observations of hundreds of mud volcanoes that source mud, water and gas from a single mudstone layer (Cartwright et al. 2023). The assertion of a single source layer is consistently evidenced by direct sampling at the sea-floor from mud volcanoes in the region (Giresse et al. 2010, Prinzhofer & Deville 2013, Pierre et al. 2014, Dupré et al. 2014, Mascle et al. 2014). Because the fluids and the sediment are both sourced from the same stratigraphic layer, the geologic record preserves qualitative and quantitative information about both the driver for the eruption and the source of the erupted material. And because the mud volcanoes are from a single basin, these observations do not have the structural and geological variability of a global dataset, enabling a focus on fundamental processes. Therefore, these observations constitute an unprecedented opportunity for studying the mechanisms of subsurface sediment mobilisation during mud volcano eruptions.

In the Nile Deep Sea Fan, the mudstone source layer is overlain by a laterally extensive impermeable salt layer. This salt layer enables large overpressures to accumulate in the mudstone layer by preventing pressure dissipation via vertical fluid flow. Sedimentation and hydrocarbon generation are thought to be the main mechanisms pressurising the

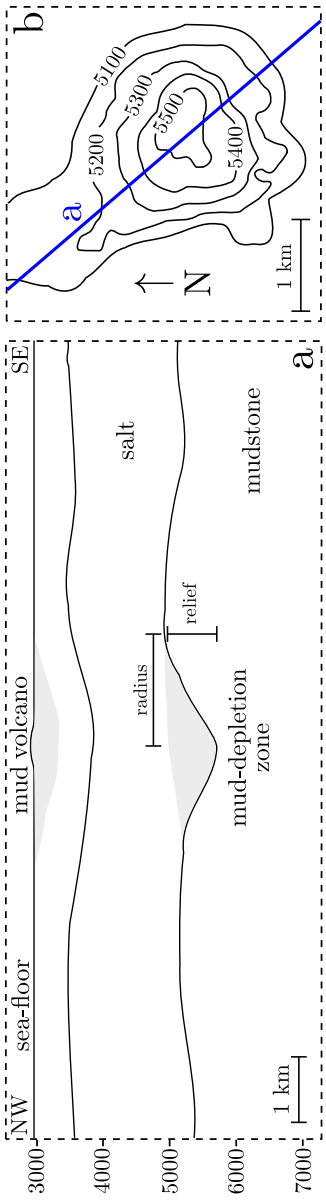

Figure 4.1: Example of a mud volcano from the Nile Deep Sea Fan, adapted from Cartwright et al. (2023). (a) Cross sectional view, showing a zone of localised depletion of the mudstone layer beneath the mud volcano corresponding to depression of the salt layer. Grey shaded areas show the mud-depletion zone (bottom), commensurate in volume with the zone of extruded mud (top). (b) Plan view of base-salt surface, with depth contours labelled in metres (black curves).

region (Kirkham et al. 2022). Mud volcanoes enable the release of this overpressure by venting through cylindrical conduits that penetrate the salt layer; it is widely interpreted that these conduits are formed by hydraulic fracturing (Huuse et al. 2005, Roberts et al. 2010, Løseth et al. 2011). Across the Nile Deep Sea Fan, seismic data reveals that the expulsion of remobilised mudstone leads to localised thinning of the mudstone source layer (Cartwright et al. 2023); these regions of localised thinning are known as mud-depletion zones (Graue 2000, Stewart & Davies 2006). These mud-depletion zones are consistently bowl-shaped with a squat aspect ratio, with 340 ± 150 m reliefs and 790 ± 240 m radii (Figure 4.1; Cartwright et al. 2023). However, no existing quantitative theory of mud volcanoes can explain the consistent morphometrics of these depletion zones.

The closest existing quantitative model was proposed for the Lusi eruption (Rudolph et al. 2011). This model takes the depletion zone to be a disc that grows laterally as the elastic stresses in the intact (and impermeable) surrounding mudstone reach a yield condition. This model is likely to be inappropriate for the Nile Deep Sea Fan since the model ignores any role of fluids in the remobilisation of the mudstone or the evolution of pressure within the mudstone. Indeed, the accepted theory for pressure evolution in sedimentary basins is poroelastic dynamics (Muggeridge et al. 2004, 2005). In this case, a lava-fragmentation theory is a helpful analogue. Fowler et al. (2010) demonstrates how a low-pressure front propagating into a poroelastic medium can progressively disaggregate and carry away the material. Furthermore, experiments on gassy sediments demonstrate how gas exsolution and expansion promote disaggregation and loss of strength (Blouin et al. 2019). The presence of natural gas is highly correlated with mud volcanism (Kopf 2002, Mazzini & Etiope 2017) and is well documented in the Nile Deep Sea Fan (Loncke et al. 2004, Prinzhofer & Deville 2013, Pryce et al. 2023). There, seismic observations suggest that gas expansion and exsolution play the additional role of supporting the base of the salt during mud volcanism prior to the viscous flow of salt into the depletion zone

(Cartwright et al. 2023).

Previous core analyses have shown that the initial phase of mud volcanism is typically a vigorous eruption of fluids, principally water and methane (Robertson 1996, Kopf et al. 1998, Deville & Guerlais 2009). This is in contrast to the slow venting of mostly fluids observed during majority of their lifetimes (Deville & Guerlais 2009). These core analyses are supported by eyewitness accounts of newly erupting mud volcanoes in Trinidad (Barr & Bolli 1953, Higgins 1974). Furthermore, seismic observations from the Nile Deep Sea Fan reveal the formation of craters at the onset of mud volcanism, which are best explained by an initial phase of vigorous fluid venting (Pryce et al. 2023). Fluidisation, whereby consolidated sediments can be mobilised by migrating pore fluids of a sufficient velocity, has previously been proposed as a mechanism to explain mud volcano formation (e.g., Brown 1990, Nermoen et al. 2010). In particular, experiments by Rocha (1993) reveal that fluid venting from a conduit through an impermeable layer leads to spherical flow that converges towards the base of the conduit. He suggests that this converging flow initiates radially spreading fluidisation at the conduit. Indeed, using a similar experimental setup, Nichols et al. (1994) show that rapid fluid venting induces localised fluidisation beneath the conduit and, consequently, sedimentary volcanism.

In spite of extensive research, no previous quantitative theory of mud volcanism has combined the poroelastic dynamics of the source region with sediment remobilisation by fluidisation. As noted above, the model proposed by Rudolph et al. (2011) assumes that the mudstone source is impermeable and that remobilisation occurs by plastic failure. Davies et al. (2011) assume poroelastic dynamics in the fluid source, but they neglect the mudstone source from their model. An exception is Nermoen et al. (2010), who model the fluidisation of poroelastic sediments above an active venting conduit, but they neglect the dynamics of the source region feeding the conduit. A theory coupling the poroelastic dynamics and fluidisation of the source regions of mud volcanoes is needed in order to

describe the evolution of their eruptions and explain observations of their mud-depletion zones.

Here, we develop a poroelastic model of the mudstone source region coupled to a model of mudstone fluidisation. We solve the governing equations to elucidate the parametric controls on fluidisation during venting and the associated pressure dynamics. We show in particular that the characteristic size of a mud-depletion zone is given by $\sigma_T/\mathcal{G}$, where σ_T is the tensile strength of the sealing rock (salt in the case of the Nile Deep Sea Fan) and $\mathcal{G}$ is the critical pressure gradient required to fluidise the mudstone. We show that this critical pressure gradient can be estimated using the material properties of the mudstone. We provide supporting evidence for this theory by showing that the predicted size of mud-depletion zones is consistent with observed sizes from the Nile Deep Sea Fan.

The remainder of the chapter is organised as follows. In §4.2, we derive a poroelastic model of fluid venting with dynamic fluidisation; we then solve the model numerically and use asymptotics to glean analytical solutions. In §4.3, we compare analytical solutions with observations from the Nile Deep Sea Fan and discuss the wider implications of this work and the limitations of the model. In §4.4, we conclude with a summary.

4.2 Model

Poroelasticity describes the two-way coupling between the hydrological and mechanical behaviour of a porous medium. Therefore, a poroelastic model of the flow through and the fluidisation of a mudstone is fully coupled. To elucidate these coupled dynamics, in §4.2.1, we first exclude fluidisation from the problem and consider the poroelastic problem of fluid venting. Then in §4.2.2, we use this solution to inform the derivation of a fully coupled model of venting with dynamic fluidisation.

4.2.1 Fluid venting

We consider two horizontal layers of rock, salt overlying mudstone, as illustrated in Figure 4.2. Motivated by observations from the Nile Deep Sea Fan, we assume that that the mudstone has a semi-infinite vertical extent and both layers have an infinite lateral extent. We assume that the salt layer is impermeable, consistent with its behaviour over geological timescales (though see Ghanbarzadeh et al. 2015). This model configuration thus prohibits vertical pressure diffusion across the salt. However, we allow for fluid venting via hydraulic fracturing.

4.2.1.1 Initial and boundary conditions

A vertical hydraulic fracture forms at the base of the salt when the mudstone pressure exceeds the critical pressure for fracturing P_f, which is the sum of the minimum horizontal compressive stress Σ_{min} and tensile strength σ_T of the overlying salt seal, i.e.,

$$P_f = \Sigma_{\text{min}} + \sigma_T. \tag{4.1}$$

This hydraulic fracture propagates towards the surface, driven by gas buoyancy, exsolution and expansion. When the fracture breaches the seafloor, it then serves as a high-permeability pathway, i.e., a conduit, that connects the mudstone to the surface.

Conduit dynamics have been considered by few quantitative models of mud volcanoes. Zoporowski & Miller (2009) assume a constant flow rate into the conduit, predicting oscillatory venting behaviour with an hourly frequency; this is consistent with observations of mud volcanoes in Trinidad (Deville & Guerlais 2009). This oscillatory venting arises from the inclusion of inertial forces in their model. Oscillatory venting from mud volcanoes may also be a consequence of the non-linear dynamics of bubble formation

and segregation during the ascent of the gas-rich slurry in the conduit (see Pereira & Fowler 2020). Over longer timescales, however, the time-averaged flow rate will decline as pressure within the mudstone equilibrates with that of the conduit. Davies et al. (2011) study long-term venting behaviour by assuming a constant pressure at the conduit. We adopt the latter assumption in the interest of studying the long-term evolution of mud-depletion zones. In particular, the conduit will remain open while the mudstone pressure exceeds the minimum compressive stress $\Sigma_{\min}$. We therefore expect that, over long timescales, the pressure at the base of the conduit obeys

$$P = \begin{cases} P_f & \text{if } t < 0, \\ P_f - \sigma_T & \text{if } t \geq 0, \end{cases} \tag{4.2}$$

where we have chosen our time variable t such that the conduit forms at time $t = 0$.

Conduit formation requires the prior generation of near-lithostatic pore pressures in the mudstone. Sedimentary basins are usually pressurised over geological timescales (Osborne & Swarbrick 1997). In particular, the Nile Deep Sea Fan has been regionally pressurised by sedimentation and hydrocarbon generation since ∼6 Ma (Kirkham et al. 2017). We assume that this regional pressurisation is spatially uniform and sufficiently slow to neglect active pressurisation during venting in the model (Kirkham et al. 2022, Kearney et al. 2024). We therefore expect that, prior to venting, the pressure in the mudstone is hydrostatic and the vertical component of the total stress in the mudstone Σ_{zz} is lithostatic, i.e.,

$$\left.\begin{aligned} P &= P_f + \rho_f g z, \\ \Sigma_{zz} &= -\Sigma_{\min} - [\phi\rho_f + (1-\phi)\rho_s] g z, \end{aligned}\right\} \tag{4.3}$$

where tension is taken to be positive, ϕ is the porosity of the mudstone, which is assumed

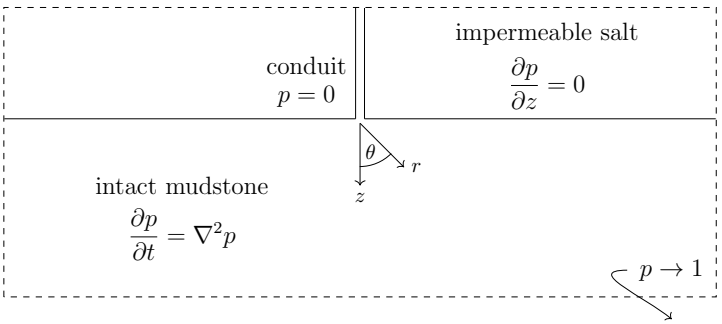

Figure 4.2: Schematic cross-section of fluid venting problem. We consider two regions of the problem, the sub-salt intact mudstone region and the trans-salt conduit region. The origin of our axisymmetric spherical coordinate system is at the centre of the base of the conduit.

to be constant with depth, ρ_f is the density of the pore fluid of the mudstone, ρ_s is the density of the solid grains of the mudstone and z is the depth from the base of the salt layer. Rocks in sedimentary basins are laterally confined, so lithostatic vertical stresses generate horizontal stresses via the Poisson effect (Lazebnik & Tsinker 1998). For fine-grained sediments like mudstones with near-lithostatic pore pressures, these horizontal stresses are approximately lithostatic (Jones 1994, Casey 2014). Therefore we assume that, initially, the total stress tensor in the mudstone $\mathbf{\Sigma} = -\Sigma_{\text{min}}\mathbf{I} - [\phi\rho_f + (1-\phi)\rho_s]gz\mathbf{I}$, where $\mathbf{I}$ is the identity tensor. Furthermore, as these initial conditions for the semi-infinite mudstone persist at large distances from disturbances at the conduit, they also act as far-field boundary conditions.

In the remainder of this chapter, for simplicity, we use pressures and stresses that are defined relative to these initial hydrostatic and lithostatic gradients. Specifically, we henceforth use the overpressure p, defined as the pressure in excess of hydrostatic: $p \equiv P - \rho_f gz$, where where g is the body force per unit mass due to gravity. Additionally, we use the total stress tensor in excess of lithostatic: $\boldsymbol{\sigma} \equiv \mathbf{\Sigma} + [\phi\rho_f + (1-\phi)\rho_s]gz\mathbf{I}$.

4.2.1.2 Intact mudstone

The initial drop in pressure at the conduit will drive flow through and deformation of the intact mudstone. We assume that the solid skeleton of the mudstone obeys linear elasticity and such that, taking tension to be positive, the effective stress tensor $\boldsymbol{\sigma}'$ (in excess of its lithostatic and hydrostatic components) is related to the strain tensor $\boldsymbol{e}$ via

$$\boldsymbol{\sigma}' = \lambda \mathrm{tr}\,(\boldsymbol{e})\,\mathbf{I} + 2\mu\boldsymbol{e}, \tag{4.4}$$

where λ and μ are the drained Lamé parameters and $\boldsymbol{e} \equiv \frac{1}{2}[\boldsymbol{\nabla u} + (\boldsymbol{\nabla u})^{\mathrm{T}}]$ with $\boldsymbol{u}$ denoting the solid displacement relative to the initial state of the mudstone. The effective stress is related to the total stress $\boldsymbol{\sigma}$ and overpressure p by Terzaghi's principle,

$$\boldsymbol{\sigma} = \boldsymbol{\sigma}' - p\mathbf{I}, \tag{4.5}$$

where we have taken the solid grains to be incompressible. We assume that the pore space of the mudstone is filled with methane-saturated water and small, isolated bubbles of methane that travel with the same velocity as the water. The lack of segregation between the water and methane enables us to treat the bulk fluid in the mudstone as a single phase. We also assume that, in the mudstone, there is negligible exsolution of methane from the water (Duan & Mao 2006). Mass conservation leads to the storage equation,

$$\frac{\partial e}{\partial t} + S\frac{\partial p}{\partial t} = -\boldsymbol{\nabla} \cdot \boldsymbol{q}, \tag{4.6}$$

where $e \equiv \mathrm{tr}\,(\boldsymbol{e})$ is the volumetric strain and $S \equiv \phi c_f$ is the storativity, with porosity ϕ and fluid compressibility c_f. The segregation flux between the fluid and solid phases $\boldsymbol{q}$ is governed by Darcy's law,

$$\boldsymbol{q} = -\frac{k}{\eta}\boldsymbol{\nabla} p, \tag{4.7}$$

where k is the permeability and η is the dynamic viscosity of the fluid. Neglecting inertia, momentum conservation reads

$$\boldsymbol{\nabla} \cdot \boldsymbol{\sigma} = 0. \tag{4.8}$$

Combining equations (4.4), (4.5) and (4.8) gives

$$\lambda \boldsymbol{\nabla}[\mathrm{tr}\,(\boldsymbol{e})] + 2\mu \boldsymbol{\nabla} \cdot \boldsymbol{e} = \boldsymbol{\nabla} p. \tag{4.9}$$

In general, the storage equation (4.6) must be solved simultaneously with equation (4.9) because the pore pressure and the strain tensor are fully coupled. However, these quantities can be decoupled with an additional constraint on the geometry of deformations.

The geometry of this system is similar to that of a partially penetrating well in an aquifer (Muskat 1938); such geometries give rise to hemispherical fluid flow towards the well. This hemispherical flow has also been observed in experiments of mud volcanoes (Rocha 1993). We thus hypothesise that this geometrical effect produces the approximate hemispherical and axisymmetric morphologies of the mud-depletion zones in the Nile Deep Sea Fan. Consequently, we use a spherical coordinate system, where a given point is parameterised using the radial distance from a fixed point of origin to the point r and the angle between a fixed reference direction and the line connecting the point to the origin θ. We orient our coordinates such that the origin is located at the centre of the base of the conduit and the reference direction is vertically downwards, as shown in Figure 4.2. Therefore, applying the assumption of spherically symmetric deformations to equation (4.9) gives

$$(\lambda + 2\mu)\frac{\partial e}{\partial r} = \frac{\partial p}{\partial r}. \tag{4.10}$$

where the volumetric strain is $e \equiv \mathrm{tr}\,(\boldsymbol{e})$. Equation (4.10) can be solved by integrating and applying the far-field conditions $p(r \to \infty, t) \to p_f$ and $e(r \to \infty, t) \to \sigma_T(\lambda + \frac{2}{3}\mu)^{-1}$,

giving

$$(\lambda + 2\mu)\left(e - \frac{\sigma_T}{\lambda + \frac{2}{3}\mu}\right) = p - p_f. \tag{4.11}$$

Combining this solution with equations (4.6) and (4.7) gives

$$\frac{\partial p}{\partial t} = \frac{k}{\eta}\frac{\lambda + 2\mu}{1 + S(\lambda + 2\mu)}\nabla^2 p. \tag{4.12}$$

Equation (4.12) is a partial differential equation describing the poroelastic diffusion of pressure through the mudstone. The diffusivity of pressure (i.e., the pre-factor on the right-hand side) depends on both the elastic moduli of the solid skeleton and the compressibility of the fluid in the pore space. Clearly, a highly compressible pore fluid, such as natural gas, can significantly reduce this diffusivity. In this case, which is common to mud volcanoes (Kopf 2002), solid deformation is negligible and the assumption of radial symmetry is not required to obtain a decoupled equation for the diffusion of pressure. Though to preserve the possibility of solid deformation in the model, we proceed with the assumption of spherical symmetry. Therefore, the model can be written in terms of r only,

$$\frac{\partial p}{\partial t} = \frac{k}{\eta}\frac{\lambda + 2\mu}{1 + S(\lambda + 2\mu)}\frac{1}{r^2}\frac{\partial}{\partial r}\left(r^2\frac{\partial p}{\partial r}\right) \quad \text{for } r \in [R, \infty), \tag{4.13}$$

where R is the radius of the conduit and the boundary conditions are given by

$$\left.\begin{aligned} p &= p_f - \sigma_T && \text{at } r = R, \\ p &\to p_f && \text{as } r \to \infty, \end{aligned}\right\} \tag{4.14}$$

and the mudstone is initially uniformly overpressured (i.e., hydrostatically pressured) $p(r, t < 0) = p_f$.

4.2.1.3 Nondimensionalisation

We non-dimensionalise this system of equations using mudstone properties, introducing a dimensionless radial distance from the conduit r^*, mudstone overpressure p^*, and time t^*, defined as

$$r \equiv R\, r^*, \qquad \frac{p - (p_f - \sigma_T)}{\sigma_T} \equiv p^*, \qquad t \equiv \frac{R^2}{D} t^*. \tag{4.15}$$

The radial distance is scaled by the radius of the conduit, which is typically of order metres to tens of metres (Cartwright & Santamarina 2015). Time is scaled by the characteristic time for a pressure perturbation to diffuse over a length equal to the radius of the conduit. Due to the low diffusivities of mudstones, this poroelastic process typically requires years and thus we scale time accordingly to study the pressure behaviour over these timescales. The dimensionless system of equations is then

$$\frac{\partial p^*}{\partial t^*} = \frac{1}{r^{*2}} \frac{\partial}{\partial r} \left(r^{*2} \frac{\partial p^*}{\partial r^*} \right) \quad \text{for } r^* \in [1, \infty), \tag{4.16}$$

with boundary conditions,

$$\left.\begin{aligned} p^* &= 0 \qquad \text{at } r^* = 1, \\ p^* &\to 1 \qquad \text{as } r^* \to \infty, \end{aligned}\right\} \tag{4.17}$$

and initial condition $p^*(r^*, t^* < 0) = 1$. The solution to this system of equations is well known (see, e.g., Carslaw & Jaeger 1959):

$$p^* = 1 - \frac{1}{r^*} \mathrm{erfc}\left(\frac{r^* - 1}{2\sqrt{t^*}} \right), \tag{4.18}$$

which has the steady-state solution $p^*(r^*, t^* \to \infty) \to 1 - 1/r^*$. Fig. 4.3 shows that the pressure gradient in the mudstone is always maximum at the conduit. Differentiating equation (4.18) with respect to r^* and setting $r^* = 1$ yields the pressure gradient at the

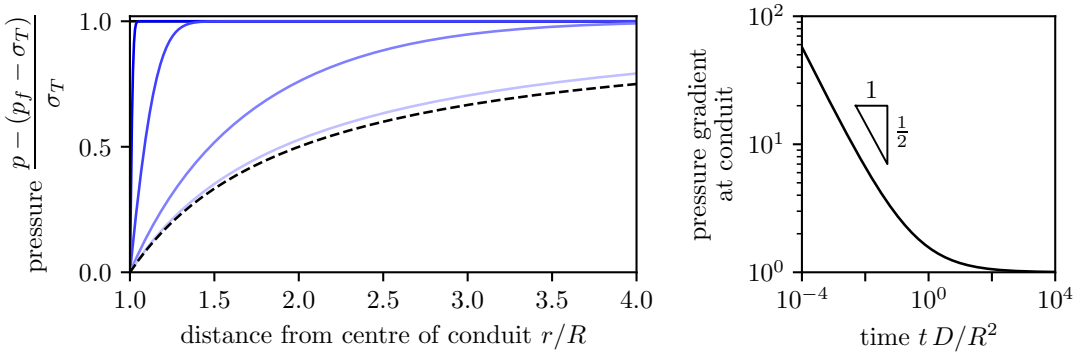

Figure 4.3: Fluid venting solution. Left: Dimensionless overpressure versus dimensionless distance from the centre of the base of the conduit at times $t^* = (10^{-4}, 10^{-2}, 10^0, 10^2)$ (dark to light blue). We also show the corresponding late-time solution (black dashed). Right: Time evolution of the overpressure gradient at the conduit.

conduit (Fig. 4.3),

$$\left.\frac{\partial p^*}{\partial r^*}\right|_{r^*=1} = 1 + \frac{1}{\sqrt{\pi t^*}}. \tag{4.19}$$

Equation (4.19) predicts that at early times $t^* \to 0$, the pressure gradient becomes arbitrarily large. This is due to the sudden opening of the conduit enforced by equation (4.2). Indeed, seismic evidence from the Nile Deep Sea Fan reveals that the earliest phase of mud volcanism is vigorous fluid venting (Pryce et al. 2023).

Such large pressure gradients imply that large drag forces are exerted on the solid grains in the mudstone. If these drag forces exceed the resistive forces from the grains, the grains can become mobilised. This process of sediment mobilisation is known as fluidisation. Fluidisation initiates at a critical pressure gradient. Since our model predicts that the maximum pressure gradient is at the conduit, fluidisation is expected to initiate at the conduit. We anticipate that fluidisation will then spread radially outwards from the conduit at a rate set by poroelastic pressure diffusion. We show in the following sections that fluidisation transforms the dynamic behaviour of the venting system.

4.2.2 Fluidisation

4.2.2.1 Critical force

Fluidisation is assumed to initiate when the drag (i.e., the net force) exerted by the fluid on the solid grains exceeds a critical interaction force (Richardson 1971). We assume that the component of force in the direction of flow is effective in driving fluidisation; that is, fluidisation occurs when $\boldsymbol{F} \cdot \hat{\mathbf{n}} > \boldsymbol{\mathcal{F}} \cdot \hat{\mathbf{n}}$, where $\boldsymbol{F}$ is the interaction force per unit volume, $\boldsymbol{\mathcal{F}}$ is the critical value of the interaction force per unit volume, and $\hat{\mathbf{n}} \equiv -\boldsymbol{\nabla} p/|\boldsymbol{\nabla} p|$ is the flow direction. Conservation of momentum for the fluid phase leads to an expression for the interaction force (Appendix 4.A; Katz 2022),

$$\boldsymbol{F} = \phi \boldsymbol{\nabla} p + (p + \rho_f \boldsymbol{g}) \boldsymbol{\nabla} \phi. \tag{4.20}$$

Common to mud-volcanic systems, natural gas is much more deformable than mudstones. Thus, we assume that gradients in porosity are small, such that $\boldsymbol{F} \sim \phi \boldsymbol{\nabla} p$. For a cohesionless sediment, it is typically assumed that fluidisation will occur when the divergence of the effective stress vanishes (e.g., Vardoulakis 2004). This occurs when the interaction force exceeds the negative buoyancy force per unit volume of the fluid, equal to $\phi(1-\phi)(\rho_s - \rho_f)\boldsymbol{g}$. However, fine-grained sediments like mudstones typically exhibit cohesive forces between grains that can resist fluidisation. Therefore, we can write that the critical interaction force for fluidisation $\boldsymbol{\mathcal{F}}$ is given by

$$\boldsymbol{\mathcal{F}} \sim \phi \boldsymbol{\mathcal{G}} = \boldsymbol{\mathcal{C}} + \phi(1-\phi)(\rho_s - \rho_f)\boldsymbol{g}, \tag{4.21}$$

where $\boldsymbol{\mathcal{G}}$ is the corresponding critical pressure gradient for fluidisation. The cohesive force opposes drag and thus always acts in the direction opposite to flow. Therefore, the maximum cohesive force that must be overcome by drag can be expressed as $\boldsymbol{\mathcal{C}} = \mathcal{C}\,\hat{\mathbf{n}}$,

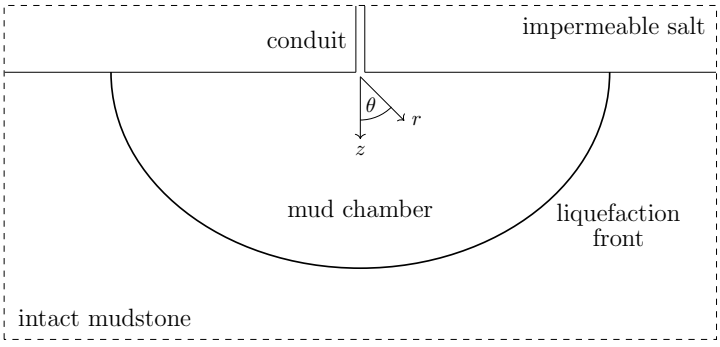

Figure 4.4: Schematic cross-section of fluidisation problem. We consider three regions: the sub-salt intact mudstone region, the sub-salt mud chamber region, and the trans-salt conduit region. The intact mudstone and mud chamber regions are separated by a dynamic interface termed the fluidisation front (thick curved line). As in Figure 4.2, the origin of the axisymmetric spherical coordinate system is at the centre of the base of the conduit.

where $\mathcal{C} \geq 0$.

Solid grains in consolidated rocks are held in place by forces from neighbouring grains. At an interface, however, one side is exposed, so there are approximately half as many grain–grain contacts. As such, there is an imbalance between such cohesive forces and the viscous forces driving fluidisation. Furthermore, the solution in §4.2.1 suggests that fluidisation initiates at the interface between the conduit and the mudstone, where the pressure gradient is largest. Therefore, we assume that fluidisation of the intact mudstone is localised to a discrete interface, which we term the fluidisation front. The fluidisation front is a moving interface at which intact mudstone is transformed to fluidised mud. The advance of the front thus generates a region of fluidised mud, which we term the mud chamber (Figure 4.4). During this transformation to a fluidised state, the solid grains of the mudstone are broken apart at this interface and, as such, the intact mudstone is eroded.

Prior to fluidisation, the mudstone is critically overpressured and the solid grains are initially in a tensile effective-stress state. Fluidisation breaks apart the solid grains; the pressure energy in the fluid is transferred to the solid grains in order to disaggregate

them. We assume that the energy required to disaggregate a given volume of grains is a constant material property; therefore, the pressure drop across the front is constant, denoted as Δp. Experiments have shown that gas expansion and exsolution promotes the disaggregation of porous materials (Blouin et al. 2019). Indeed, the gas expansion and exsolution corresponding to this drop in pressure will both localise deformation and moderate the advance of the front. While the presence of gas is not essential to the model (Appendix 4.C), we include it in the model due to its presence in the Nile Deep Sea Fan (and other mud volcano provinces) and its demonstrated role in sediment disaggregation. However, additional physics is required to constrain the rate of advance of the front, i.e., the rate of fluidisation of the intact mudstone.

4.2.2.2 Rate of fluidisation

The intensity of fluidisation typically increases with the amount by which the interaction force exceeds the critical value (Bell 1983). We thus expect that if the interaction force is below the critical value, the rate of fluidisation is zero and if the interaction force is above the critical value, the rate of fluidisation increases with the excess interaction force. We assume a linear relationship between the rate of fluidisation (i.e., the rate of erosion of the intact mudstone), and the excess force. Since we expect that the normal component of force is effective in driving fluidisation, we write that

$$v_n = \begin{cases} -\alpha(\boldsymbol{F} - \boldsymbol{\mathcal{F}}) \cdot \hat{\mathbf{n}} & \text{if } \boldsymbol{F} \cdot \hat{\mathbf{n}} \geq \boldsymbol{\mathcal{F}} \cdot \hat{\mathbf{n}}, \\ 0 & \text{if } \boldsymbol{F} \cdot \hat{\mathbf{n}} < \boldsymbol{\mathcal{F}} \cdot \hat{\mathbf{n}}, \end{cases} \tag{4.22}$$

where v_n is the rate of fluidisation in the flow direction and the constant of proportionality $\alpha \geq 0$ is a kinetic coefficient. Therefore, the front advances into the intact mudstone as

fluid is expelled. Since $\boldsymbol{F} \sim \phi \boldsymbol{\nabla} p$, we can rewrite equation (4.22) as,

$$v_n = \begin{cases} -\phi\alpha(\boldsymbol{\nabla} p - \boldsymbol{\mathcal{G}}) \cdot \hat{\mathbf{n}} & \text{if } \boldsymbol{\nabla} p \cdot \hat{\mathbf{n}} \geq \boldsymbol{\mathcal{G}} \cdot \hat{\mathbf{n}}, \\ 0 & \text{if } \boldsymbol{\nabla} p \cdot \hat{\mathbf{n}} < \boldsymbol{\mathcal{G}} \cdot \hat{\mathbf{n}}, \end{cases} \tag{4.23}$$

where the factor $\phi\alpha$ is then the effective mobility of the fluidisation front. Experiments on the erosion of mudstones by tangential viscous flow viscous shear stresses (i.e., by flow that is tangential to the front) suggest an analogous linear relationship between the erosion rate and the excess shear stress (Shaikh et al. 1988). Moreover, similar linear erosion relationships are used to predict the equilibrium shapes of river channels (e.g., Abramian et al. 2020). In the context of viscous flow, shear stresses and pressure gradients are closely related. For example, during Poiseuille flow through a pipe, the shear stresses experienced by the solid walls are linearly related to the pressure gradient driving flow (Bird et al. 2002). Considering these similarities to established laws, we assert that Equation (4.23) is valid for predicting the dynamics of fluidisation.

Equation (4.23) effectively couples the rate of fluidisation with the process of poroelastic diffusion through the mudstone via the pressure gradient at the front. The solution for pressure diffusion during fluid venting (e.g., equation (4.19)) implies that, during a mud volcano eruption, fluidisation will slow as pressure diffuses radially. This radial spreading of the fluidisation front generates a region of fluidised mud, which we term the mud chamber. In the mud chamber, we envision that the solid grains that have been disaggregated by fluidisation form a suspension in the fluid. While accurate rheological models of granular suspensions exist (e.g., Jerolmack & Daniels 2019), such models carry significant complexity and computational expense. Henceforth, we assume a uniform poro-viscous rheology to show that the behaviour of the mud chamber does not significantly impact the dynamics of the system.

4.2.2.3 Mud chamber

In the mud chamber, we envision that the disaggregated solid phase flows as well as the water and gas bubbles. As in the intact mudstone, we assume that there is no segregation between the water and the gas bubbles and no gas exsolution. We assume that the disaggregated solid phase behaves as a Newtonian fluid, allowing us to relate the effective stress tensor $\boldsymbol{\sigma}'$ to the strain-rate tensor $\dot{\boldsymbol{e}}$ via

$$\boldsymbol{\sigma}' = \Lambda \mathrm{tr}\,(\dot{\boldsymbol{e}})\,\mathbf{I} + 2M\dot{\boldsymbol{e}}, \tag{4.24}$$

where Λ is the volume viscosity (related to the bulk viscosity $\zeta \equiv \Lambda + \frac{2}{3}M$) and M is the dynamic shear viscosity of the disaggregated solid. Following the same approach as in §2.1.2, momentum conservation under spherically symmetric conditions gives

$$\frac{\partial p}{\partial r} = (\Lambda + 2M)\frac{\partial \dot{e}}{\partial r}, \tag{4.25}$$

where $\dot{e} \equiv \mathrm{tr}\,(\dot{\boldsymbol{e}})$. As we are interested in modelling the long-term dynamics of mud volcano eruptions, we consider the case of the mud chamber becoming large. In this case, we expect that the strain-rate tends to zero at the conduit ($r = 0$). Then integrating equation (4.25), applying mass conservation (4.6) and Darcy's law (2.9), we obtain

$$\frac{\partial p}{\partial t} = \frac{k}{\eta}\frac{1}{S}\nabla^2 p - \frac{p - (p_f - \sigma_T)}{S(\Lambda + 2M)}. \tag{4.26}$$

where $S(\Lambda + 2\mathrm{M})$ emerges as a characteristic timescale of pressure relaxation. This timescale is analogous to the Maxwell timescale of viscoelastic materials. This effective viscoelastic rheology of the slurry is produced by a viscous component from the solid phase and an elastic component from the compressibility of the fluid phase. Equation (4.26) suggests that pressures in the mud chamber exceeding the pressure at the

conduit $p_f - \sigma_T$ decay exponentially over this timescale. The viscoelastic timescale is likely less than seconds since $S = \phi c_f \sim 10^{-8}$ Pa^{-1}, and we expect that the viscosity of the mud is much less than 10^8 Pa s (Manga et al. 2009). Therefore, viscous pressure losses are generally only significant at times of order seconds or less. This allows us to assume that the pressure is hydrostatic throughout the mud chamber during the majority of an eruption. From Darcy's law, this assumption implies that segregation between the solid and fluid phases is negligible in the mud chamber.

Since the overpressure throughout the mud chamber equals $p_f - \sigma_T$ and the pressure jump across the fluidisation front is a constant Δp, it follows that the pressure in the mudstone at the fluidisation front is constant, equal to

$$p = p - \sigma_T + \Delta p. \tag{4.27}$$

4.2.2.4 Intact mudstone

The equations governing the intact mudstone can then be written,

$$\frac{\partial p}{\partial t} = \frac{k}{\eta} \frac{\lambda + 2\mu}{1 + S(\lambda + 2\mu)} \nabla^2 p, \tag{4.28}$$

where at the fluidisation front (on the mudstone side),

$$p = p_f - \sigma_T + \Delta p, \tag{4.29a}$$

$$v_n = -\phi\alpha \max\Big(0, (\boldsymbol{\nabla} p - \boldsymbol{\mathcal{G}}) \cdot \hat{\mathbf{n}}\Big), \tag{4.29b}$$

and, initially, $p = p_f$ and the fluidisation front grows from the centre of the base of the conduit. Since the fluidisation front is a surface of constant pressure, flow is always perpendicular to the front. Therefore at the fluidisation front, the flow direction $\hat{\mathbf{n}}$ is

equivalent to the inward normal direction to the front. As such, v_n can equivalently be interpreted as the normal velocity of the front.

In the absence of fluidisation, the pressure field has spherical symmetry (see §4.2.1). Thus, it will prove useful to recast the system of equations using the spherical coordinate system defined in §4.2.1. To do so, we define the position of the fluidisation front using the radial distance of the front from the origin $r = s(\theta, t)$. Therefore, equation (4.28) becomes

$$\frac{\partial p}{\partial t} = \frac{k}{\eta}\frac{\lambda + 2\mu}{1 + S(\lambda + 2\mu)}\left[\frac{1}{r^2}\frac{\partial}{\partial r}\left(r^2\frac{\partial p}{\partial r}\right) + \frac{1}{r^2\sin\theta}\frac{\partial}{\partial\theta}\left(\sin\theta\frac{\partial p}{\partial\theta}\right)\right] \quad \text{for } r \in [s(\theta,t), \infty). \tag{4.30}$$

and we can use equation (4.21) to rewrite equation (4.29b) as

$$\frac{\partial s}{\partial t} = \overbrace{\phi\alpha\left(\frac{\partial p}{\partial r} - (1-\phi)(\rho_s - \rho_f)g\cos\theta - \frac{\mathcal{C}}{\phi}\frac{1}{\sqrt{1 + {s_\theta}^2/s^2}}\right)}^{\text{excess force in radial direction}} \underbrace{- \phi\alpha\frac{s_\theta}{s}\left(\frac{1}{s}\frac{\partial p}{\partial\theta} + (1-\phi)(\rho_s - \rho_f)g\sin\theta + \frac{\mathcal{C}}{\phi}\frac{s_\theta/s}{\sqrt{1 + {s_\theta}^2/s^2}}\right)}_{\text{excess force in hoop direction}}, \tag{4.31}$$

where we have expressed the critical pressure gradient using equation (4.21) and $s_\theta \equiv \partial s/\partial\theta$. Equation (4.31) shows the contributions to fluidisation from components of excess force in the radial and hoop directions, labelled accordingly. The excess force in the hoop direction is modulated by a factor s_θ/s, which quantifies the deviation of the fluidisation front from a sphere. Thus, fluidisation will be primarily driven by forces in the radial direction if the front is near-spherical. Note that, the gravitational force resisting fluidisation acts downwards and thus varies with θ; gravity provides no resistance against horizontal fluidisation ($\theta = \pi/2$). To generate further insight into the dominant physical mechanisms, we nondimensionalise this system of equations.

4.2.2.5 Nondimensionalisation

We non-dimensionalise this system of equations by introducing a dimensionless radius r^*, mudstone overpressure p^* and time t^*:

$$r \equiv \frac{\sigma_T - \Delta p}{(1-\phi)(\rho_s - \rho_f)g} r^*, \qquad \frac{p - (p_f - \sigma_T + \Delta p)}{\sigma_T - \Delta p} \equiv p^*, \qquad t \equiv \frac{(\sigma_T - \Delta p)^2}{(1-\phi)^2(\rho_s - \rho_f)^2 g^2 D} t^*. \tag{4.32}$$

The radius is scaled by the length of a characteristic pressure disturbance in the mudstone. Namely, if the pressure gradient at the front were at the critical value for a cohesionless mudstone. Time is scaled by the time for pressure to diffuse across this characteristic length. Poroelastic pressure diffusion through mudstones typically occurs over thousands of years and thus we scale time to study the pressure behaviour over these geological timescales. Pressure is scaled by the initial pressure drop at the conduit. This formulation helps to highlight the differences in behaviour from fluidisation. The dimensionless system of equations is then

$$\frac{\partial p^*}{\partial t^*} = \frac{1}{r^{*2}} \frac{\partial}{\partial r} \left(r^{*2} \frac{\partial p^*}{\partial r^*} \right) + \frac{1}{r^{*2} \sin\theta} \frac{\partial}{\partial \theta} \left(\sin\theta \frac{\partial p^*}{\partial \theta} \right) \quad \text{for } r^* \in [s^*(\theta, t^*), \infty), \tag{4.33}$$

where, at the fluidisation front,

$$\left.\begin{aligned} & p^* = 0 && \text{at } r^* = s^*(\theta, t^*), \\ & \mathrm{St} \frac{\partial s^*}{\partial t^*} = \frac{\partial p^*}{\partial r^*} - \cos\theta - \mathrm{Co} \frac{1}{\sqrt{1 + s_\theta^{*2}/s^{*2}}} && \\ & -\frac{s_\theta^*}{s^*} \left(\frac{1}{s^*} \frac{\partial p^*}{\partial \theta} + \sin\theta + \mathrm{Co} \frac{s_\theta^*/s^*}{\sqrt{1 + s_\theta^{*2}/s^{*2}}} \right) && \text{at } r^* = s^*(\theta, t^*), \end{aligned}\right\} \tag{4.34}$$

with initial conditions $s^*(\theta, 0) = 0$ and $p^*(r^*, \theta, 0) = 1$. Two dimensionless parameters Co and St emerge to characterise the system,

$$\mathrm{Co} \equiv \frac{\mathcal{C}/\phi}{(1-\phi)(\rho_s - \rho_f)g} \quad \text{and} \quad \mathrm{St} \equiv \frac{D}{\phi\alpha(\sigma_T - \Delta p)}. \tag{4.35}$$

The cohesion number Co measures the resistance to fluidisation from cohesive forces relative to the resistance from the buoyant weight of the solid phase. The cohesion number has been previously used to classify the fluidisation behaviours of different powders (Mutsers & Rietema 1977, Rietema 1984). For example, fine-grained powders tend to exhibit significant cohesion and are generally difficult to fluidise. This suggests that fine-grained sediments like mudstones have strong cohesion. However, the mudstones that feed mud volcanoes tend to be highly overpressured and thus are generally underconsolidated (Yassir 1989); this is the case in the Nile Deep Sea Fan (Kirkham et al. 2017). Therefore, cohesion may be approximately as strong as gravity $\mathrm{Co} \sim 1$. The Stefan number St measures the diffusivity of pressure through the mudstone relative to the diffusivity of the fluidisation front, which depends on the material properties of the mudstone and the excess force required to propagate the front at a given rate. If pressure diffuses through the mudstone faster than the fluidisation front, then $\mathrm{St} > 1$.

The Stefan number is named by analogy with the classical Stefan problem, which describes the evolution of the boundary between two phases of the same material undergoing a phase change. More specifically, our model of the fluidisation of an overpressured mudstone has many similarities to classical models of the melting of a superheated solid. This superheated Stefan problem describes the diffusion of temperature away from the melting front, where the temperature at the melting front is fixed at the melting temperature. The rate of melting is governed by an energy balance between the heat flowing into the front and the latent heat consumed for melting. The various melting behaviours

that arise from this energy balance are characterised by the Stefan number, the ratio of the latent heat for melting to the sensible superheat initially contained in the solid. This initial superheat is analogous to the quantity $(\sigma_T - \Delta p)$, which is the extent that the effective stress initially exceeds the effective-stress requirement for fluidisation. The analogy to the latent heat is less clear, though equation (4.35) suggests that the analogous quantity is the characteristic pressure $D/(\phi\alpha)$. To further demonstrate the connection between our model and a Stefan problem, we consider the behaviour of the model at early times.

At early times $t^* \to 0^+$, the sudden opening of the conduit (4.2) implies that the pressure gradient at the fluidisation front is much larger than the resistance to fluidisation. Moreover, the initial condition for the fluidisation front implies that $s^*_\theta \sim 0$ at early times. Therefore,

$$\mathrm{St}\frac{\mathrm{d}s^*}{\mathrm{d}t^*} \sim \frac{\partial p^*}{\partial r^*} \quad \text{at } r^* = s^*(t^*) \quad \text{for } t^* \to 0^+. \tag{4.36}$$

In this limit, the problem exactly reduces to a spherically-symmetric Stefan problem. This problem admits the classical Neumann solution for the self-similar growth of the mud chamber,

$$p^* = 1 - \frac{\Phi(\xi^*)}{\Phi(\beta)}, \qquad s^* = \beta\sqrt{t^*}, \tag{4.37}$$

where the self-similar variable $\xi^* \equiv r^*/\sqrt{t^*}$, the fundamental solution to the spherical diffusion equation Φ is given by

$$\Phi(\xi^*) = \frac{\exp(-\xi^{*2}/4)}{\xi^*} - \frac{\sqrt{\pi}}{2}\mathrm{erfc}\frac{\xi^*}{2}. \tag{4.38}$$

and the growth rate β is set implicitly by

$$\beta^3\Phi(\beta)\exp\left(\frac{\beta^2}{4}\right) = \frac{2}{\mathrm{St}}. \tag{4.39}$$

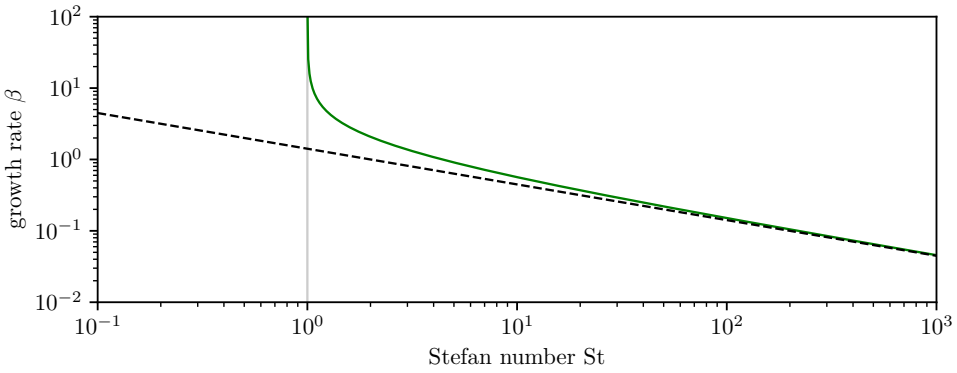

Figure 4.5: Solution for growth rate β as a function of the dimensionless Stefan number St.

Figure 4.6 shows how the growth rate β depends on the parameter St; the fluidisation front tends to grow more slowly with larger values of St. Indeed, for $\mathrm{St} \to \infty$, i.e., when the diffusivity of the fluidisation front is arbitrarily slow, equation (4.39) reduces to $\beta \to \sqrt{2/\mathrm{St}}$. In contrast, the growth rate diverges as $\mathrm{St} \to 1^+$ and there are no real solutions to equation (4.39) for $\mathrm{St} \leq 1$ (Fig. 4.6). This $\mathrm{St} \leq 1$ regime corresponds to the diffusivity of the fluidisation front being faster than the diffusivity of pressure through the mudstone. If pressure cannot diffuse faster than the fluidisation front, then pressure locally builds up. From equation (4.36), this local build-up of pressure drives motion of the fluidisation front; this positive feedback loop can lead to blow-up of the solution (i.e., $\mathrm{d}s^*/\mathrm{d}t^* \to \infty$). Blow-up can be avoided under different initial conditions, where, for example, travelling-wave solutions $s^* \sim t^*$ can be obtained (see Dewynne et al. 1989, Dewynne 1990). However in general, this result is clearly unphysical and conflicts with observations of mud volcanoes. As mud volcanoes erupt mostly fluids for the majority of their lifetimes (Deville & Guerlais 2009), the rate of fluid flow is typically larger than the rate of fluidisation $\mathrm{St} > 1$. Thus we do not consider the regime $\mathrm{St} \leq 1$ to be relevant to mud volcanism.

Superheated and supercooled Stefan problems have been studied extensively, mainly

due to their ill-posedness (Mullins & Sekerka 1963, Sherman 1970, Fasano & Primicerio 1981, Howison et al. 1985, Fasano et al. 1989, 1990). Not only does this ill-posedness lead to blow-up of solutions, the melting front also suffers from the Mullins–Sekerka instability (Mullins & Sekerka 1963), which is closely related to the Saffman–Taylor instability responsible for viscous fingering (Saffman & Taylor 1958). In the context of melting, this instability is physically acceptable as it is consistent with observations of dendritic growth in supercooled melts (e.g., snowflakes). However, there is generally a lack of observational evidence for a similar instability during mud volcanism (though see §4.3), despite the many similarities with our model. Indeed, our model predicts that the fluidisation front is unstable to perturbations (Appendix 4.D). Such instabilities typically necessitate complex numerical methods (e.g., phase-field, level-set) for solution. Furthermore, additional physics must be incorporated into the model since the isobaric boundary condition does not provide any mechanism for mode selection. We wish to avoid such complications, as we are interested in developing models that can be tested against observations. To this end, we simplify the model by considering the approximate spherical symmetry of the fluidisation front that is observed both in the field and in experiments. The directional dependence on θ in equations (4.33) and (4.34) originates from the anisotropy in the critical pressure gradient for fluidisation. Thus spherical symmetry can be achieved by assuming that the critical pressure gradient is isotropic, i.e., $\boldsymbol{\mathcal{G}} = \mathcal{G}\,\hat{\mathbf{n}}$, where $\mathcal{G} \equiv \mathcal{C}/\phi + (1-\phi)(\rho_s - \rho_f)g$ is a constant. The dimensionless system of equations becomes

$$\frac{\partial p^*}{\partial t^*} = \frac{1}{r^{*2}}\frac{\partial}{\partial r}\left(r^{*2}\frac{\partial p^*}{\partial r^*}\right) \quad \text{for } r^* \in [s^*(t^*), \infty), \tag{4.40}$$

where at the fluidisation front,

$$\left.\begin{aligned} p^* &= 0 && \text{at } r^* = s^*(t^*), \\ \mathrm{St}\frac{\mathrm{d}s^*}{\mathrm{d}t^*} &= \frac{\partial p^*}{\partial r^*} - (1 + \mathrm{Co}) && \text{at } r^* = s^*(t^*), \end{aligned}\right\} \tag{4.41}$$

with initial conditions $s^*(0) = 0$ and $p^*(r^*, 0) = 1$. We solve this system of equations numerically using a standard finite difference scheme (Appendix 4.E), shown in Figure 4.6. Figure 4.6 illustrates the impact of St on the pressure and the growth of the mud chamber at various times for a cohesionless mudstone $\mathrm{Co} = 0$. For each value of St, the mud chamber initially grows rapidly, slowing down as pressure diffuses into the mudstone in accordance with the early-time solution (4.37). The numerical solution begins to deviate from the early-time solution when the pressure gradient at the fluidisation front becomes comparable to the critical pressure gradient; front advance ceases when the pressure gradient is subcritical. At $\mathrm{St} = 1.1$, the diffusivity of the fluidisation front is slightly less than the diffusivity of pressure through the mudstone. Therefore, the corresponding timescale of mud chamber growth is similar to that of poroelastic pressure diffusion $t^* \sim 1$. However for $\mathrm{St} = 10$, the diffusivity of the fluidisation front is small compared to the mudstone pressure, and growth instead ceases much later $t^* \sim \mathrm{St}$.

Furthermore, at large values of St, the mudstone pressure will not vary significantly from a quasi-steady state due to this disparity in diffusivities. Taking the limit of $\mathrm{St} \to \infty$ implies that pressure field instantaneously reaches an equilibrium with the position of the interface (King & Riley 2000), characterised by

$$p^* = 1 - \frac{s^*}{r^*}. \tag{4.42}$$

Combining equation (4.42) with the Stefan condition (4.41) gives an ordinary differential

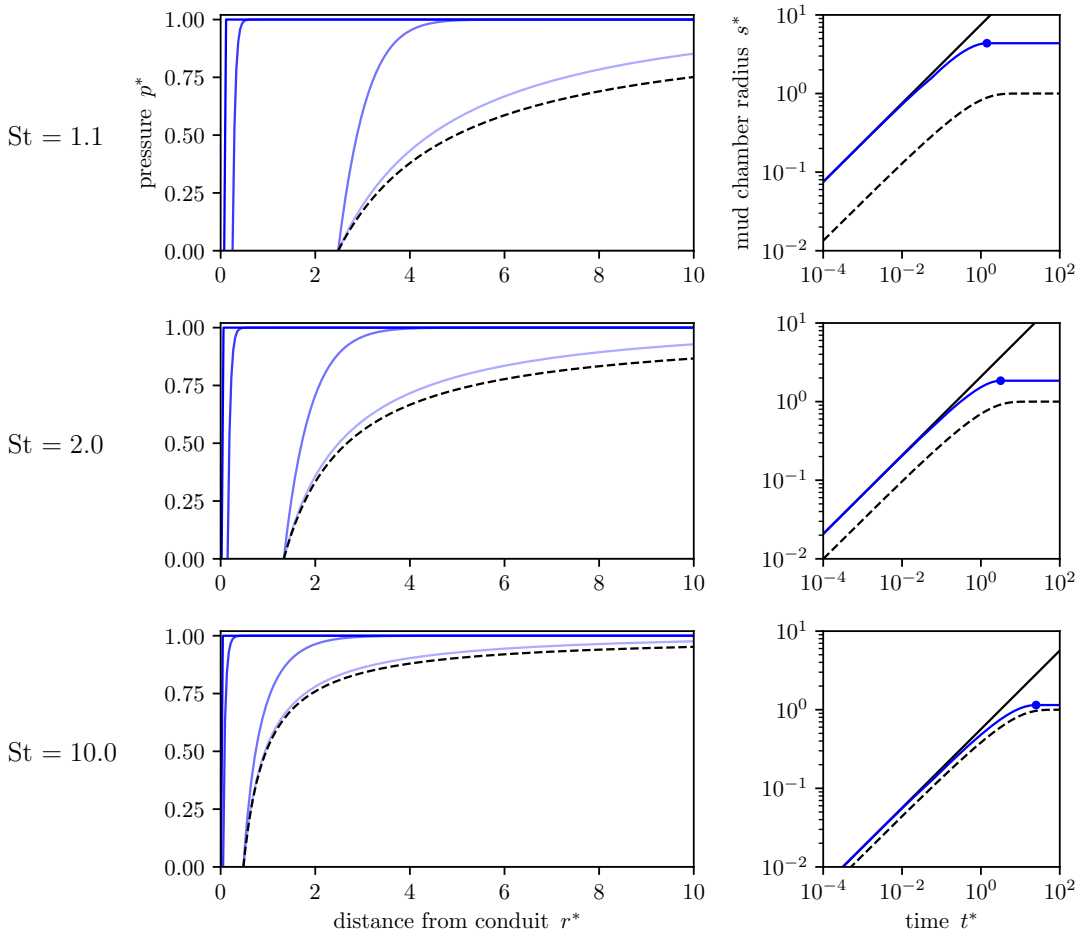

Figure 4.6: Numerical solution. Left: Dimensionless overpressure versus dimensionless distance from the centre of the base of the conduit at times $t^* = (10^{-4}, 10^{-2}, 10^{0}, 10^{2})$ (dark to light blue). We also show the corresponding late-time solution (black dashed). Right: Time evolution of the overpressure gradient at the conduit.

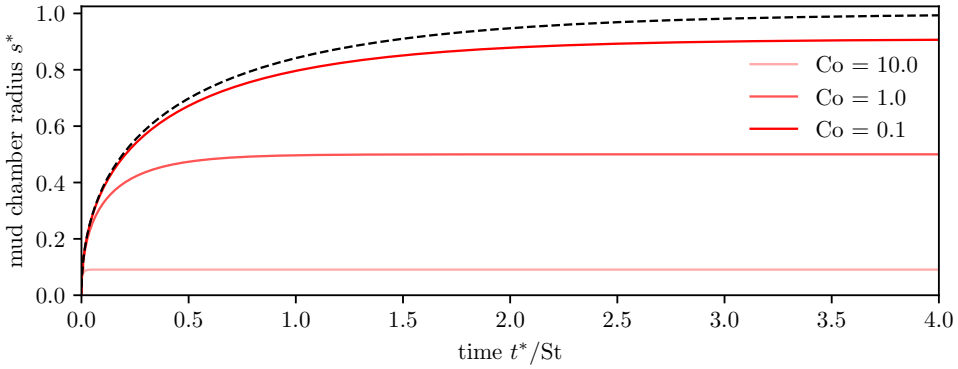

Figure 4.7: Solutions for growth of mud chamber as $\mathrm{St} \to \infty$ for various values of the cohesion number Co.

equation for the time evolution of the radius of the mud chamber,

$$\mathrm{St}\frac{\mathrm{d}s^*}{\mathrm{d}t^*} = \frac{1}{s^*} - (1 + \mathrm{Co}), \tag{4.43}$$

which, when combined with the initial condition $s^*(0) = 0$, has the solution

$$s^* = \frac{1}{1+\mathrm{Co}}\left\{1 + W\left[-\exp\left(-(1+\mathrm{Co})^2\frac{t^*}{\mathrm{St}} - 1\right)\right]\right\}, \tag{4.44}$$

where W is the Lambert W function. Figure 4.7 shows how the growth of the mud chamber depends on the cohesion number. Equation (4.44) shows that a cohesive mudstone fluidises over a shorter timescale by a factor of $(1+\mathrm{Co})^2$. At times much larger than this fluidisation timescale $t^* \gg \mathrm{St}/(1+\mathrm{Co})^2$, the mud chamber tends asymptotically towards a final size of

$$s^* \to \frac{1}{1+\mathrm{Co}} \quad \text{for } t^* \gg \frac{\mathrm{St}}{(1+\mathrm{Co})^2}. \tag{4.45}$$

Therefore if $\mathrm{Co} \ll 1$, then the final size of the mud chamber $s^* \sim 1$ is set by the resistance to fluidisation from gravity. Conversely if $\mathrm{Co} \gg 1$, then the final size $s^* \sim 1/\mathrm{Co}$ is controlled by the resistance to fluidisation from cohesion. In any case, we can write in

dimensional terms,

$$s \to \frac{\sigma_T - \Delta p}{\mathcal{C}/\phi + (1-\phi)(\rho_s - \rho_f)g}. \tag{4.46}$$

Equation (4.46) allows us to predict the final size of the mud chamber, and thus the size of the corresponding mud-depletion zone, using estimates of basin properties.

4.3 Discussion

The expression (4.46) derived above for the final size of the mud chamber has been obtained via a number of simplifying assumptions. We assume that the initial phase of vigorous fluid venting during mud volcanism drives rapid porous flow through a poroelastic mudstone. This rapid porous flow overcomes resistance from gravity and cohesion to fluidise the mudstone; we assume that a large rate of fluid flow is required for a given rate of fluidisation. Finally, we assume that this fluid flow and thus the fluidisation of the mudstone are spherically symmetric.

Equation (4.46) can be used to validate our model of mud volcanoes by comparing the estimated final size of a mud-depletion zone with field observations. For observations, we consider a set of 86 particularly well-constrained mud-depletion zones from the Nile Deep Sea Fan located in the Eastern Mediterranean (Cartwright et al. 2023). Most of the parameters required for estimation using equation (4.46) are known with minor uncertainty (see Table 4.1). For example, extended leak-off tests suggest that the tensile strength of salt is in the range 2 ± 1 MPa (Bérest et al. 2015). However, cohesive forces in mudstones have not been studied directly, especially in the context of fluidisation. Some studies characterise cohesive forces using the cohesive strength (i.e., the shear strength at zero effective stress) normalised by the grain size (Rietema 1984). Rietema (1984) state that the cohesive strength of fluidised fine-grained materials with grain sizes less than ~ 100 μm is typically ~ 4 Pa. Therefore, the corresponding value of cohesion is

Parameter	**Description**	**mean**	**std. dev.**	**min.**	**max.**	**Reference**
σ_T (MPa)	salt tensile strength	2	1	0.5	4	Bérest et al. (2015)
ϕ	mudstone porosity	0.20	0.05	0.05	0.30	Yang & Aplin (2007)
ρ_s (kg m^{-3})	mudstone grain density	2500	250	2000	3000	De Wit & Arens (1950)
ρ_ℓ (kg m^{-3})	water density	950	900	1000	20	Kell & Whalley (1975)
ρ_g (kg m^{-3})	methane density	400	200	500	100	Friend et al. (1989)
S_g	methane saturation	0.30	0.10	0.70	0.20	Chen et al. (2022)
$\log_{10}\mathcal{C}$ ($\log_{10}$ Pa/m)	(log) mudstone cohesion	4	3	5	0.5	Rietema (1984)

Table 4.1: Mudstone properties used in estimating the vertical extent of the mud depletion zones at the Nile Deep Sea Fan. We assign a truncated normal distribution for each parameter, taking all parameters to be uncorrelated. The mean and standard deviation of each distribution, as well as the minimum and maximum values at which the distributions are truncated, are given by the values presented in the table. From these distributions, we use the model under a Monte Carlo framework to calculate a distribution for the vertical extent of the mud depletion zones.

typically $\sim 10^4$ Pa/m.

Figure 4.8 shows histograms of the reliefs and radii of 86 mud-depletion zones from the Nile Deep Sea Fan, with probability distributions estimated using our model and Table 4.1. In the horizontal direction, only cohesion resists fluidisation. Thus we can assume that, to leading order, the horizontal radius of depletion zones is set by $\sigma_T/(\mathcal{C}/\phi)$; doing so, we estimate a mean horizontal radius of 700 m. This agrees with measurements of the horizontal radii of mud-depletion zones in the Nile Deep Sea Fan (Figure 4.8). In the vertical direction, both cohesion and gravity resist fluidisation. By substituting estimated values into equation (4.46), we calculate a mean vertical extent of 150 m (Figure 4.8). This somewhat agrees with observations (Figure 4.8), but underestimates some of the larger observed vertical extents, which range up to 1000 m. This underestimation of the vertical extent may be explained by the common anisotropy in the permeability of mudstones due to their strong layering. Measurements of mudstones find that the permeability to flow in the direction parallel to layering, typically horizontal, is usually a factor of 2–3 times larger than for the direction perpendicular to layering, typically vertical (Yang & Aplin 2007). Flow in the less-permeable vertical direction exerts stronger drag forces on the mudstone and thus may enhance vertical fluidisation by a similar factor of 2–3, resolving the discrepancy between our prediction and the observations. However, without solving the full two-dimensional problem, we may only speculate on the relative importance of these effects on the shapes of mud-depletion zones.

Solving the full two-dimensional model numerically may be difficult due to the instability of the fluidisation front. There is no observational evidence from the Nile Deep Sea Fan to suggest unstable, dendritic growth of the mud chamber. However, for example, earthen dams are known to fail by 'piping' (Richards & Reddy 2007), which describes the formation of an erosive channel beneath a dam, triggered by sufficiently large pressure gradients. Furthermore, experiments with fluidised beds suggest that highly cohesive

materials tend to fluidise via a network of fractures that form tangential to the front and are connected by channels that are oriented normal to the front (Geldart 1973). Rietema (1984) state that sufficiently strong viscous forces can stabilise this channelling behaviour towards uniform fluidisation. In the current model we have neglected viscous dissipation in the mud chamber, justified by the low viscosity of mud in comparison to the long timescale of poroelastic diffusion through mudstones. But close to the moving fluidisation front, viscous losses in the mud chamber could provide an important stabilising mechanism that may be similar to kinetic undercooling in melting and solidification problems. Moreover, the disruption of intergranular bonds that occurs when a surface is created is energetically costly. Rigorously including this energetic cost in the model (using, e.g., the strain energy release rate concept in fracture mechanics; see Rice & Budiansky 1973) will likely stabilise the front to high-frequency perturbations.

We have assumed that the salt behaves as a rigid, impermeable layer throughout the eruption despite the viscoelastic rheology of salt. Depending on the relative timescales of viscoelastic stress relaxation in the salt and poroelastic diffusion through the mudstone, the salt may flow into the mud-depletion zone during the eruption. It is currently unclear how incorporating the flow of salt may affect the predicted final shape of the mud chamber. Moreover, the resulting local increase in total stress caused by the local increase in salt thickness may drive further fluidisation than the model currently predicts.

The model may further underpredict the extent of fluidisation due to the simplified boundary condition applied at the conduit. In reality, the pressure at the conduit is not fixed open for all time at a constant pressure, but may open and shut periodically, as suggested by Zoporowski & Miller (2009). This periodic opening may drive additional fluidisation. It is likely that once the flow rate into the conduit becomes lower than a critical value, the conduit will seal by viscous creep of the salt. However, we expect that the time-averaged behaviour of the model is accurate. For example, the model predicts

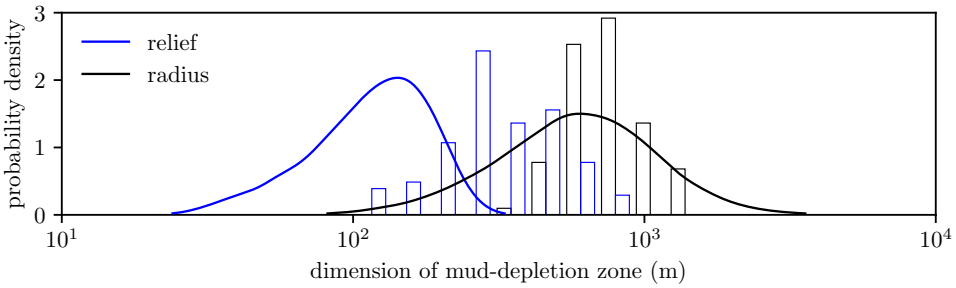

Figure 4.8: Comparison of model predictions (probability distributions) and observations (histograms) of mud-depletion zone radii (black) and reliefs (blue).

that mature mud volcanoes erupt mostly fluids; this is supported by observations of mud volcanoes from Trinidad (Deville & Guerlais 2009). The model also predicts that the composition of the extruded material is most sediment-rich at earliest times. This is in conflict with eye-witness accounts of the first hours of mud volcanism from Trinidad, which suggest that mud volcanoes initially erupt fluids. This may be explained by the formation of a fluid-rich layer at the base of the salt prior to eruption, as suggested by experiments (Nichols et al. 1994). Another explanation for this may be the thixotropic (i.e., time-dependent shear thinning) property of mud. The model could capture the initial fluid-rich eruption by incorporating thixotropy; this could be done by, for example, following the approach of Hewitt & Balmforth (2013) and introducing a time-dependent parameter that quantifies the extent to which the mudstone has been fluidised.

In contrast, the assumption of a semi-infinite mudstone layer may overpredict the extent of fluidisation. Indeed, Cartwright et al. (2023) hypothesise that the size of the mud-depletion zones in the Nile Deep Sea Fan may be limited by the vertical extent of the mudstone source unit. In this hypothesis, fluidisation progresses vertically until the base of the mudstone, later forming a 'mud weld' between the base of the salt and the layer beneath the mudstone. The term 'mud weld' was first used by Dupuis et al. (2019), who document mud-depletion zones from offshore Nigeria which have similar sizes to those

from the Nile Deep Sea Fan. Cartwright et al. (2023) base their mud-weld hypothesis with seismic data, by interpreting that the base of the mudstone source unit lies at the boundary between two major seismic facies. While we cannot rule out their hypothesis, both seismic facies consist primarily of mudstones and thus the difference in fluidisation behaviour across the boundary is not expected to be significant.

Our model invokes a variety of further simplifying assumptions. These assumptions make the model tractable and transparent, but also carry limitations. The equation for the rate of fluidisation (4.22) assumed in our model determines the dynamic growth of the mud chamber. Though, in the large-St limit, the final size of mud chamber (4.46) is independent of these dynamics. Basin stratigraphies seldom consist of uniform, horizontal layers; layer topography and heterogeneity will affect the spatial distribution of overpressure and fracture pressure, and thus also of venting loci. The sedimentary layers themselves are composed of rocks with porosity-dependent and anisotropic permeability that do not behave perfectly poro-elastically. However, we do not expect any of these features to change the key qualitative implications of our model.

The model is readily generalisable to other settings, scenarios and geometries (Appendix 4.F). For many mud volcanoes (including the Lusi mud volcano) the source of mud and the source of fluids are separate. Thus, a pressurised fluid reservoir could be placed below the mudstone unit to study the extent of fluidisation from separate source regions. Moreover, the subsurface remobilisation of sediment is not limited to mudstones; many geological features have been attributed to the fluidisation of sandstones. Sandstones are generally easier to fluidise due to their larger grain sizes and thus lower cohesive forces. Sand volcanoes have been observed globally (Obermeier 1996), though they are less frequently documented than mud volcanoes as the remobilisation of sand typically produces intrusive features known as injectites (Huuse et al. 2010). The remobilisation of sand is highly problematic for industrial processes involving the extraction of fluids

from poorly consolidated sandstone reservoirs. The production of sand can lead to the catastrophic collapse of the well and damage to equipment such as valves and pipelines by erosion. Furthermore, the uncontrolled release (i.e., blow out) of fluids from a well can fluidise the surrounding geological formations. For example, this can lead to the formation of craters around the wellbore; many such cases have been compiled by Rocha (1993).

Many open questions remain regarding mud volcanoes that are not addressed by this work. We assume in our model that mud volcanism initiates due to rapid fluid expulsion. It remains unclear, however, how a low-permeability mudstone can initially provide a rapid supply of fluids to the conduit. Moreover, there is no evidence from the Nile Deep Sea Fan to suggest the existence of high-permeability reservoirs that could enable such rapid venting (see Kearney et al. 2023). Experiments by Nichols et al. (1994) suggest that, prior to eruption, fluids may accumulate in conical voids at the base of the salt. Though this lack of clarity in the conditions for mud volcanism motivates further experimental and theoretical studies of the source regions of mud volcanoes. Furthermore, since we have assumed in our model that the depletion zones are spherically symmetric, we may only provide rough estimates for explaining their observed non-spherical morphometrics. These morphometrics motivate the solution of the full two-dimensional, axisymmetric model.

4.4 Conclusion

We have developed and solved a model of rapid fluid expulsion from an overpressured mudstone, leading to mudstone fluidisation and mud volcanism. Our main goal was to elucidate the mechanism of subsurface sediment mobilisation during mud volcano eruptions. The main conclusions from the study are as follows.

- In the absence of fluidisation, the sudden opening of the venting conduit drives hemi-spherical porous flow through the mudstone to the conduit. This porous flow is initially rapid, but slows towards a steady state over the poroelastic timescale of the mudstone as pressure diffuses radially outwards from the conduit.

- This rapid porous flow exerts drag forces, i.e., pressure gradients, on the solid grains that are sufficient to fluidise the mudstone by overcoming the resistance from cohesive and gravitational forces. The highest flow velocities are encountered at the conduit, thus fluidisation initiates at the conduit and spreads radially to create a hemi-spherical region of fluidised mud, the mud chamber.

- Two time-regimes emerge in the growth of the mud chamber. At early times, the resistance to fluidisation is negligible and the mud chamber exhibits self-similar growth; the radius scales with square-root time. At timescales corresponding to mudstone fluid flow, the mudstone pressure relaxes by pressure diffusion. The resistance to fluidisation becomes important, slowing and eventually stopping the growth of the mud chamber.

- In the limit of slow fluidisation relative to pressure diffusion, the mud chamber grows asymptotically towards a final radius of $(\sigma_T - \Delta p)/\mathcal{G}$, where σ_T is the tensile strength of the seal, Δp is the pressure jump across the fluidisation front and $\mathcal{G}$ is the critical pressure gradient for fluidisation.

- Using estimates of mudstone properties, we calculate mud chamber sizes that are comparable to the sizes of zones of mud depletion beneath mud volcanoes in the Nile Deep Sea Fan. We thus provide supporting evidence for this theory of flow-driven fluidisation during mud volcano eruptions.

Appendices

4.A Momentum conservation

Neglecting inertia, momentum conservation reads

$$\boldsymbol{\nabla} \cdot \phi_s \boldsymbol{\Sigma}^s + \phi_s \rho_s \boldsymbol{g} + \boldsymbol{F}_{s\ell} + \boldsymbol{F}_{sg} = 0, \tag{47a}$$

$$\boldsymbol{\nabla} \cdot \phi_\ell \boldsymbol{\Sigma}^\ell + \phi_\ell \rho_\ell \boldsymbol{g} + \boldsymbol{F}_{\ell s} + \boldsymbol{F}_{\ell g} = 0, \tag{47b}$$

$$\boldsymbol{\nabla} \cdot \phi_g \boldsymbol{\Sigma}^g + \phi_g \rho_g \boldsymbol{g} + \boldsymbol{F}_{gs} + \boldsymbol{F}_{g\ell} = 0, \tag{47c}$$

where ϕ_α is the volume fraction of phase α, $\boldsymbol{\Sigma}^\alpha$ is the total stress in phase α per unit area of phase α, and $\boldsymbol{F}_{\alpha\beta}$ is the interaction force of phase β on phase α. The interaction forces $\boldsymbol{F}_{\alpha\beta}$ must satisfy $\boldsymbol{F}_{\alpha\beta} = -\boldsymbol{F}_{\beta\alpha}$ and $\sum_{\alpha,\beta} \boldsymbol{F}_{\alpha\beta} = 0$. Momentum conservation for the bulk mixture then the sum of equations (47a)–(47c),

$$\boldsymbol{\nabla} \cdot \boldsymbol{\Sigma} + \overline{\rho} \boldsymbol{g} = 0, \tag{48}$$

where $\boldsymbol{\Sigma} = \phi_s \boldsymbol{\Sigma}^s + \phi_\ell \boldsymbol{\Sigma}^\ell + \phi_g \boldsymbol{\Sigma}^g$ is the bulk stress tensor and $\overline{\rho} = \phi_s \rho_s + \phi_\ell \rho_\ell + \phi_g \rho_g$ is the bulk density. We assume that the gas phase consists of small bubbles of methane that are distributed uniformly throughout the pore space and we therefore neglect segregation between the gas and liquid phases such that the two fluids can be treated as a single

phase f with averaged properties. Therefore, momentum conservation reduces to

$$\boldsymbol{\nabla} \cdot (1-\phi)\boldsymbol{\Sigma}^s + (1-\phi)\rho_s \boldsymbol{g} + \boldsymbol{F} = 0, \tag{49a}$$

$$\boldsymbol{\nabla} \cdot \phi\boldsymbol{\Sigma}^f + \phi\rho_f \boldsymbol{g} - \boldsymbol{F} = 0, \tag{49b}$$

where $\boldsymbol{F} \equiv \boldsymbol{F}_{s\ell} + \boldsymbol{F}_{sg}$. We assume that the fluid stress tensor can be approximated as

$$\boldsymbol{\Sigma}^f \approx -P\mathbf{I}, \tag{50}$$

where P is the pressure in the fluid and $\mathbf{I}$ is the identity tensor. Substituting the expression for pressure into momentum conservation of the fluid phase gives

$$\boldsymbol{F} = -\phi(\boldsymbol{\nabla} P - \rho_f \boldsymbol{g}) - P\boldsymbol{\nabla}\phi. \tag{51}$$

4.B Mass conservation

Starting from conservation of mass of the gas g, liquid ℓ and solid s phases,

$$\frac{\partial \phi_s \rho_s}{\partial t} + \boldsymbol{\nabla} \cdot \phi_s \rho_s \boldsymbol{v}_s = 0, \tag{52a}$$

$$\frac{\partial \phi_\ell \rho_\ell}{\partial t} + \boldsymbol{\nabla} \cdot \phi_\ell \rho_\ell \boldsymbol{v}_\ell = -\Gamma_m, \tag{52b}$$

$$\frac{\partial \phi_g \rho_g}{\partial t} + \boldsymbol{\nabla} \cdot \phi_g \rho_g \boldsymbol{v}_g = \Gamma_m, \tag{52c}$$

where Γ_m is the mass rate of exsolution of methane per unit volume. Symbols $\boldsymbol{v}^\alpha$ and ϕ_α represent the velocity and volume fraction of phase $\alpha = s, \ell, g$. Similar to Appendix 4.A, we assume that the two fluids can be treated as a single fluid phase with effective prop-

erties; mass conservation for this composite fluid phase f is then

$$\frac{\partial \phi \rho_f}{\partial t} + \boldsymbol{\nabla} \cdot \phi \rho_f \boldsymbol{v}_f = 0. \tag{53}$$

where $\phi = \phi_\ell + \phi_g$ and

$$\rho_f = \frac{\phi_\ell \rho_\ell + \phi_g \rho_g}{\phi}. \tag{54}$$

We assume that the liquid and the gas are linearly compressible, with the compressibility of the liquid given by $c_\ell \equiv \rho_\ell^{-1} \partial \rho_\ell / \partial p$ and the compressibility of the gas given by $c_g \equiv \rho_g^{-1} \partial \rho_g / \partial p$. It follows that, for the fluid phase,

$$\frac{\partial \phi}{\partial t} + \phi c_f \frac{\partial P}{\partial t} + \boldsymbol{\nabla} \cdot \phi_f \boldsymbol{v}_f = 0, \tag{55}$$

where

$$c_f = \frac{\phi_\ell c_\ell + \phi_g c_g}{\phi_\ell + \phi_g}. \tag{56}$$

We further assume that the solid grains are incompressible, giving

$$-\frac{\partial \phi}{\partial t} + \boldsymbol{\nabla} \cdot (1 - \phi) \boldsymbol{v}_s = 0. \tag{57}$$

Summing equations (55) and (57) results in

$$\frac{\partial E}{\partial t} + S \frac{\partial P}{\partial t} = -\boldsymbol{\nabla} \cdot \boldsymbol{q}, \tag{58}$$

where the segregation flux $\boldsymbol{q} \equiv \phi(\boldsymbol{v}_f - \boldsymbol{v}_s)$, the volumetric strain-rate $\partial E / \partial t \equiv \boldsymbol{\nabla} \cdot \boldsymbol{v}_s$ and the storativity $S \equiv \phi c_f$.

4.C Fluidisation front

4.C.1 Jump conditions

Mass conservation across the fluidisation front cannot be expressed using the storage equation due to discontinuities in the solution. In integral form, mass conservation of the solid and fluid phases read

$$\frac{\partial}{\partial t}\int_V \phi_s \rho_s \,\mathrm{d}V + \int_V \boldsymbol{\nabla}\cdot\phi_s\rho_s\boldsymbol{v}_s \,\mathrm{d}V = 0, \tag{59a}$$

$$\frac{\partial}{\partial t}\int_V \phi_f \rho_f \,\mathrm{d}V + \int_V \boldsymbol{\nabla}\cdot\phi_f\rho_f\boldsymbol{v}_f \,\mathrm{d}V = 0. \tag{59b}$$

For a hemi-spherical fluidisation front, $\mathrm{d}V = 2\pi r^2 \mathrm{d}r$. Substituting reduces the mass conservation equations to

$$\frac{\partial}{\partial t}\int_{r_1}^{r_2} \phi_s \rho_s \,\mathrm{d}r + [\phi_s\rho_s v_s]_{r_1}^{r_2} = 0, \tag{60a}$$

$$\frac{\partial}{\partial t}\int_{r_1}^{r_2} \phi_f \rho_f \,\mathrm{d}r + [\phi_f\rho_f v_f]_{r_1}^{r_2} = 0, \tag{60b}$$

where subscripts 1 and 2 indicate conditions upstream and downstream of the front respectively. Let the solution exhibit a shock at the front $r = s(t)$, therefore

$$\frac{\partial}{\partial t}\left(\int_{r_1}^{s^-} \phi_s \rho_s \,\mathrm{d}r + \int_{s^+}^{r_2} \phi_s \rho_s \,\mathrm{d}r\right) + [\phi_s\rho_s v_s]_{r_1}^{r_2} = 0, \tag{61a}$$

$$\frac{\partial}{\partial t}\left(\int_{r_1}^{s^-} \phi_f \rho_f \,\mathrm{d}r + \int_{s^+}^{r_2} \phi_f \rho_f \,\mathrm{d}r\right) + [\phi_f\rho_f v_f]_{r_1}^{r_2} = 0. \tag{61b}$$

Using Leibniz's integral rule, noting that $\partial r_1/\partial t = \partial r_2/\partial t = 0$ and $\partial s^-/\partial t = \partial s^+/\partial t = \partial s/\partial t$, and taking the limits of $r_1 \to s^-$ and $r_2 \to s^+$, gives the Rankine-Hugoniot-type

jump conditions

$$[\phi_s \rho_s] \frac{\mathrm{d}s}{\mathrm{d}t} = [\phi_s \rho_s v_s], \tag{62a}$$

$$[\phi_f \rho_f] \frac{\mathrm{d}s}{\mathrm{d}t} = [\phi_f \rho_f v_f]. \tag{62b}$$

It can be shown that these jump conditions also hold in one-dimensional Cartesian and cylindrical systems.

4.C.2 Incompressible phases

To demonstrate a simple case of the model, we assume incompressible phases and no gas exsolution. In this case, $[\rho_s] = [\rho_f] = 0$, giving

$$[1 - \phi] \frac{\mathrm{d}s}{\mathrm{d}t} = [(1 - \phi) v_s], \tag{63a}$$

$$[\phi] \frac{\mathrm{d}s}{\mathrm{d}t} = [\phi v_f], \tag{63b}$$

where we have introduced the porosity ϕ. In the mudstone, the velocity of the solid is negligible $v_s^- = 0$. Conversely in the mud chamber, the mud slurry is expected to move as a single phase, i.e., $v_s^+ = v_f^+$. This allows us to write that

$$\frac{[\phi]}{1 - \phi^-} \frac{\mathrm{d}s}{\mathrm{d}t} = \phi^+ v_f^+. \tag{64}$$

Substituting Darcy's law gives,

$$\frac{[\phi]}{1 - \phi^-} \frac{\mathrm{d}s}{\mathrm{d}t} = -\frac{k}{\eta} \frac{\partial p}{\partial r}\bigg|_{s^+}. \tag{65}$$

Then substituting the erosion law and rearranging yields

$$\left(\frac{[\phi]}{1-\phi^-}+\frac{k}{\eta}\frac{1}{\phi^+\alpha}\right)\frac{\mathrm{d}s}{\mathrm{d}t}=-\frac{k}{\eta}\mathcal{G}. \tag{66}$$

At late times when $\mathrm{d}s/\mathrm{d}t \to 0$, this equation requires that the factor on the left-hand side becomes arbitrarily large. It follows that $\phi^- \to 1$ at these late times.

At early times when $\mathrm{d}s/\mathrm{d}t$ is large, this equation requires that the factor on the left-hand side is small. Therefore,

$$\frac{[\phi]}{1-\phi^-}\sim-\frac{k}{\eta}\frac{1}{\phi^+\alpha}. \tag{67}$$

This equation implies that the jump in porosity is negative, i.e., the porosity in the mud chamber is larger than in the mudstone. In an incompressible system, the quantity on the right-hand side is related to the Stefan number by

$$\frac{k}{\eta}\frac{1}{\phi^+\alpha}=\mathrm{St}\,\frac{\sigma_T}{\lambda+2\mu}, \tag{68}$$

where since there is no gas expansion and exsolution in this case, we have set $\Delta p = 0$. This dimensionless quantity depends on the Stefan number, which we typically expect to be much greater than unity. However, the factor $\sigma_T/(\lambda+2\mu)$ is typically much less than unity, since for many rocks $\sigma_T \sim 10^6$ Pa and $(\lambda+2\mu) \sim 10^{10}$ Pa. Consequently, it is not clear what the value of this dimensionless quantity is. With this in mind, we rearrange for the porosity in the mud chamber and substitute the dimensionless quantity to give

$$\phi^-=\frac{\phi^+ + \mathrm{St}\,\sigma_T/(\lambda+2\mu)}{1+\mathrm{St}\,\sigma_T/(\lambda+2\mu)}. \tag{69}$$

If the dimensionless quantity $\mathrm{St}\,\sigma_T/(\lambda+2\mu) \gg 1$, then $\phi^- \sim 1$. If instead $\mathrm{St}\,\sigma_T/(\lambda+$

$2\mu) \ll \phi^+$, then $\phi^- \sim \phi^+$. Therefore even in this highly simplified system, there are a wide range of potential behaviours at the fluidisation front.

4.D Linear stability analysis

Here, we study the stability of the growth of a spherically symmetric mud chamber, which is governed by the diffusion of pressure through the mudstone,

$$\frac{\partial p^*}{\partial t^*} = \nabla^{*2} p^* \quad \text{for } r^* \in [s^*, \infty), \tag{70}$$

and at the fluidisation front,

$$\left.\begin{aligned} p^* &= 0 && \text{at } r^* = s^*, \\ \mathrm{St} v_n^* &= \boldsymbol{\nabla}^* p^* \cdot \hat{\mathbf{n}} - (1 + \mathrm{Co}) && \text{at } r^* = s^*. \end{aligned}\right\} \tag{71}$$

The growth of the mud chamber depends on gradients in pressure in the mudstone, while the pressure in the mudstone depends on the position and velocity of the fluidisation front. Therefore, the pressure diffusion problem and the free boundary problem must be solved simultaneously. The following stability analysis follows the same approach as Mullins & Sekerka (1963); they make this analysis tractable by taking the limit of $\mathrm{St} \to \infty$ (though see Tribelsky & Anisimov 2014). We make the same assumption, which implies that pressure in the mudstone evolves in a quasi-steady-state and thus obeys Laplace's equation $\nabla^{*2} p^* = 0$.

We firstly consider an infinitesimally small perturbation to the interface caused by a single spherical harmonic. The response to an infinitesimal perturbation of arbitrary shape can then be obtained by superposition as the system of equations is linear. We

position of the perturbed fluidisation front is given by

$$r^* = s^*(t^*, \theta, \varphi) = s_0^*(t^*) + \epsilon\, s_1^*(t^*) Y_\ell^m(\theta, \varphi), \tag{72}$$

where Y_ℓ^m is the spherical harmonic function of degree ℓ and order m and the dimensionless magnitude of the perturbation $\epsilon \ll 1$, such that terms that are higher order in ϵ can be neglected. The normal velocity of the interface is then approximately given by the radial velocity,

$$v_n^* = \frac{\mathrm{d}s_0^*}{\mathrm{d}t^*} + \epsilon\, \frac{\mathrm{d}s_1^*}{\mathrm{d}t^*}\, Y_\ell^m(\theta, \varphi) + O(\epsilon^2), \tag{73}$$

and the particular solution of Laplace's equation is

$$p^* = 1 - \frac{s_0^*}{r^*} - \epsilon\, \frac{s_1^* s_0^{*\ell}}{r^{*\ell+1}} Y_\ell^m(\theta, \varphi) + O(\epsilon^2). \tag{74}$$

where s_1^* is determined by

$$\mathrm{St} \frac{\mathrm{d}s_1^*}{\mathrm{d}t^*} = (\ell - 1) \frac{s_1^*}{s_0^{*2}}, \tag{75}$$

Equation (75) states that all harmonics $\ell \geq 2$ are unstable (harmonics with degree $\ell = 1$ merely translate the sphere).

4.E Numerical method

For improved accuracy, we first apply the transformation $w^* \equiv r^* p^*$, which transforms spherical diffusion into Cartesian diffusion,

$$\frac{\partial w^*}{\partial t^*} = \frac{\partial^2 w^*}{\partial r^{*2}} \quad \text{for } r^* \in [s^*, \infty), \tag{76}$$

and the conditions at the fluidisation front become

$$\left.\begin{aligned} w^* &= 0 && \text{at } r^* = s^*(t^*), \\ \mathrm{St}\frac{\mathrm{d}s^*}{\mathrm{d}t^*} &= \frac{1}{s^*}\frac{\partial w^*}{\partial r^*} - \frac{w^*}{s^{*2}} - (1+\mathrm{Co}) && \text{at } r^* = s^*(t^*), \end{aligned}\right\} \tag{77}$$

with initial conditions $s^*(0) = 0$ and $w^*(r^*, 0) = r^*$. We then fix the moving front with the transformation $\xi^* \equiv r^* - s^*$, giving

$$\frac{\partial w^*}{\partial t^*} = \frac{\mathrm{d}s^*}{\mathrm{d}t^*}\frac{\partial w^*}{\partial \xi^*} + \frac{\partial^2 w^*}{\partial \xi^{*2}} \quad \text{for } \xi^* \in [0, \infty), \tag{78}$$

and

$$\left.\begin{aligned} w^* &= 0 && \text{at } \xi^* = 0, \\ \mathrm{St}\frac{\mathrm{d}s^*}{\mathrm{d}t^*} &= \frac{1}{s^*}\frac{\partial w^*}{\partial \xi^*} - \frac{w^*}{s^{*2}} - (1+\mathrm{Co}) && \text{at } \xi^* = 0, \end{aligned}\right\} \tag{79}$$

with initial conditions $s^*(0) = 0$ and $w^*(\xi^*, 0) = \xi^*$. We apply standard finite differences on a uniformly spaced mesh to discretise this system of equations in space. The resulting set of time-dependent ordinary differential equations are solved by the method-of-lines approach using the SciPy (Python) solver `solve_ivp`.

4.F Quasi-steady-state asymptotics

4.F.1 Cartesian system

In a Cartesian coordinate system, the dimensionless system of equations is

$$\frac{\partial p^*}{\partial t^*} = \frac{\partial^2 p^*}{\partial x^{*2}} \quad \text{for } x^* \in [s^*(t^*), \infty), \tag{80}$$

where at the interface,

$$\left.\begin{aligned} p^* &= 0 && \text{at } x^* = s^*(t^*), \\ \mathrm{St}\frac{\mathrm{d}s^*}{\mathrm{d}t^*} &= \frac{\partial p^*}{\partial x^*} - 1 && \text{at } x^* = s^*(t^*), \end{aligned}\right\} \tag{81}$$

and the initial condition is

$$p^*(x^*, 0) = 1. \tag{82}$$

At times $t^* = O(1)$ we use the outer solution for pressure, given by

$$p^* \sim \mathrm{erf}(x^*/2\sqrt{t^*}) \tag{83}$$

which corresponds to negligible motion of the boundary, $s^* = \hat{s}/\mathrm{St} = O(\mathrm{St}^{-1})$. For the inner region, the appropriate rescalings are $x^* = \hat{x}/\mathrm{St}$ and $p^* = \hat{p}/\mathrm{St}$, such that

$$\frac{\partial^2 \hat{p}}{\partial \hat{x}^2} \sim 0, \tag{84}$$

and at the interface,

$$\left.\begin{aligned} \hat{p} &= 0 && \text{at } \hat{x} = \hat{s}, \\ \frac{\mathrm{d}\hat{s}}{\mathrm{d}t^*} &= \frac{\partial \hat{p}}{\partial \hat{x}} - 1 && \text{at } \hat{x} = \hat{s}, \end{aligned}\right\} \tag{85}$$

Using the outer solution, the leading-order inner solution is given by

$$\hat{p}_0 = \frac{\hat{x} - \hat{s}_0}{\sqrt{\pi t^*}}. \tag{86}$$

so that

$$\frac{\mathrm{d}\hat{s}_0}{\mathrm{d}t^*} = \frac{1}{\sqrt{\pi t^*}} - 1, \qquad \hat{s}_0 = 2\sqrt{\frac{t^*}{\pi}} - t^*. \tag{87}$$

Therefore, the maximum size of the mud chamber is approximately $s^*(1/\pi) = (\pi\mathrm{St})^{-1}$,

4.F.2 Cylindrical system

The dimensionless system of equations is

$$\frac{\partial p^*}{\partial t^*} = \frac{1}{\rho^*}\frac{\partial}{\partial \rho^*}\left(\rho^* \frac{\partial p^*}{\partial \rho^*}\right) \quad \text{for } \rho^* \in [s^*(t^*), \infty), \tag{88}$$

where at the interface,

$$\left.\begin{aligned} p^* &= 0 && \text{at } \rho^* = s^*(t^*), \\ \mathrm{St}\frac{\mathrm{d}s^*}{\mathrm{d}t^*} &= \frac{\partial p^*}{\partial \rho^*} - 1 && \text{at } \rho^* = s^*(t^*), \end{aligned}\right\} \tag{89}$$

and the initial condition is

$$p^*(\rho^*, 0) = 1. \tag{90}$$

The outer solution for pressure can be obtained using Laplace transforms, where

$$q^*\mathbb{P}^*(\rho^*, q^*) - 1 = \frac{1}{\rho^*}\frac{\partial}{\partial \rho^*}\left(\rho^* \frac{\partial \mathbb{P}^*}{\partial \rho^*}\right) \quad \text{for } \rho^* \in [s^*(q^*), \infty), \tag{91}$$

and the initial condition is

$$\mathbb{P}^*(\rho^*, 0) = \frac{1}{q^*}. \tag{92}$$

We must specify that fluidisation initiates from the conduit, which has a finite dimensionless radius R^*. Therefore, this system of equations has the solution

$$\mathbb{P}^*(q^*) = \frac{1}{q^*} - \frac{1}{q^*}\frac{K_0(\rho^*\sqrt{q^*})}{K_0(R^*\sqrt{q^*})}. \tag{93}$$

where K_n is the order n modified Bessel function of the second kind. The inverse transform of equation (93) is given by (Goldstein 1932)

$$p^*(\rho^*, t^*) = \frac{2}{\pi}\int_0^\infty \frac{J_0(uR^*)Y_0(u\rho^*) - J_0(u\rho^*)Y_0(uR^*)}{J_0^2(uR^*) + Y_0^2(uR^*)}\frac{\exp(-u^2t^*)}{u}\,\mathrm{d}u. \tag{94}$$

where J_n is the order n Bessel function of the first kind and Y_n is the order n Bessel function of the second kind. Thus, the pressure gradient at the conduit is

$$\left.\frac{\partial p^*}{\partial \rho^*}\right|_{r^*=R^*} = \frac{4}{\pi^2 R^*}\int_0^\infty \frac{\exp(-u^2t^*)}{J_0^2(uR^*) + Y_0^2(uR^*)}\frac{\mathrm{d}u}{u}. \tag{95}$$

As in the Cartesian system, the appropriate rescalings in the inner region are $\rho^* = \hat{\rho}/\mathrm{St}$ and $p^* = \hat{p}/\mathrm{St}$. Thus

$$\hat{p}_0 = \frac{4}{\pi^2}\ln\frac{\hat{\rho}}{\hat{s}_0}\int_0^\infty \frac{\exp(-u^2t^*)}{J_0^2(u\hat{s}_0) + Y_0^2(u\hat{s}_0)}\frac{\mathrm{d}u}{u}. \tag{96}$$

so that

$$\frac{\mathrm{d}\hat{s}_0}{\mathrm{d}t^*} = \frac{4}{\pi^2\hat{s}_0}\int_0^\infty \frac{\exp(-u^2t^*)}{J_0^2(u\hat{s}_0) + Y_0^2(u\hat{s}_0)}\frac{\mathrm{d}u}{u} - 1. \tag{97}$$

The growth of the mud chamber in this cylindrical system is noticeably more complex than the Cartesian and spherical systems. This additional complexity stems from the coupling of the pressure gradient at the front with the radius of the mud chamber and the lack of a steady state solution for pressure. Consequently, the growth of the mud chamber differs from the square-root-time scalings of the Cartesian and spherical systems. In cylindrical systems, numerical methods are generally required to solve for the growth of the mud chamber. However, analytical solutions can be readily obtained for a constant-flow-rate condition at the front (Carslaw & Jaeger 1959).

Chapter 5

Conclusion

5.1 Summary of results

Fluid venting phenomena ubiquitously enable the rapid leakage of fluids from the subsurface, yet remain poorly understood. This thesis has aimed to elucidate the fundamental physical processes governing fluid venting from sedimentary basins. To do so, I have developed theories of fluid venting and validated them using the geological record of venting from the Eastern Mediterranean. This work lays the foundations for various exciting future developments, as detailed in §5.2 below.

In Chapter 2, I developed and solved a model of pressure evolution of sedimentary layers subject to horizontal tectonic compression, leading to episodic fluid venting. I showed that sustained tectonic compression will generate extreme overpressures required for hydraulic fracturing of the sealing layer. Once hydraulic fracturing initiates, the sandstone pressure drops rapidly due to fluid venting. After venting ceases, the sandstone pressure is then slowly recharged by tectonic compression and pressure diffusion from the mudstone layer, leading to repeated venting episodes.

During episodic venting, the time interval between episodes is shown to tend towards a fixed period, given by $\tau = \sigma_T/\Gamma_s/(1+\nu/\gamma)$, where σ_T is the tensile strength of the seal, Γ_s is the pressure build-up rate in the sandstone layer due to tectonic compression, and $(1+\nu/\gamma)$ is the venting frequency multiplier. The venting frequency multiplier $(1+\nu/\gamma)$ is determined by the dimensionless ratio ν/γ, which is independent of strain rate and permeability. Based on estimates of sandstone and mudstone elastic properties, ν/γ is typically controlled by the ratio of thicknesses of the mudstone and sandstone layers. Fluid venting phenomena are commonly found in mudstone-dominated basins; in these settings, pressure recharge will be dominated by diffusion.

In Chapter 3, I provided evidence for the theory developed in Chapter 2. In particular, I tested the hypothesis that mudstones can act as sources of pressure, fueling fluid venting from subsurface reservoirs. To test the pressure-source hypothesis, I used empirical evidence from the geological record of episodic fluid venting in the Levant Basin, where the times of each venting episode have been previously estimated. I gleaned further information from these venting times by developing a stochastic model of reservoir pressure evolution and using it to invert the venting times for parameters such as the rate of pressure recharge between venting episodes. I then quantified and compared various candidate mechanisms of pressure recharge, which revealed that poroelastic pressure diffusion from mudstones provides the most plausible explanation for these observations. Therefore, the Levant fluid vents provide strong spatiotemporal evidence supporting the pressure-source hypothesis.

This evidence relies on the accuracy of the inferences deriving from the stochastic model. I used Bayesian inference to invert the venting data for the full probability distribution of each parameter and quantify their uncertainty. I showed that this method of inference is effective on synthetic data produced by the model. I then demonstrated the accuracy of inferences made from real data by analysing the fluid vents at Oceanus,

which is situated in a less tectonically active region of the basin. This lack of tectonic activity makes the timings of venting episodes at Oceanus particularly well constrained. From the Oceanus data, I inferred a mean rate of pressure recharge of 28 MPa/Myr; this inference produces model outputs with striking similarities to the data.

I then extended the inferences from Oceanus to a more complex system—the 12 venting sites distributed along the Levant margin. Due to their close proximities, I introduced the possibility of pressure coupling into the model. I showed that vents in a coupled system form complementary pockmark series, whereas uncoupled vents behave independently. This contrast between independent and complementary venting behaviour is a qualitative diagnostic for pressure coupling. The model identifies all adjacent venting sites that are greater than 10 km apart as decisively uncoupled and indicates pressure coupling between sites labelled 3, 4, and 5, each located along the same anticline. Furthermore, the inferences for pressure coupling are in agreement with the qualitative diagnostic behaviour. I thus asserted that the stochastic model captures the main pressure behavior, both spatially and temporally. This result lends support to the accuracy of these inferences and, therefore, to the theory of fluid venting developed in Chapter 2.

In Chapter 4, I modified this theory of fluid venting to include mudstone remobilisation, i.e., mud volcanism. I showed that the sudden opening of the venting conduit drives rapid porous flow through the mudstone to the base of the conduit. This rapid porous flow exerts drag forces on the solid grains that are sufficient to fluidise the mudstone by overcoming the resistance from cohesive and gravitational forces. I demonstrated that fluidisation initiates at the conduit and spreads radially to create a hemi-spherical region of fluidised mud, termed the mud chamber. At early times, the resistance to fluidisation is negligible and the mud chamber exhibits self-similar growth; the radius scales with square-root time. At timescales corresponding to large-scale fluid flow through the mud-

stone, the drag forces on the solid grains relax by pressure diffusion. It follows that the resistive forces to fluidisation become important, slowing and eventually stopping the growth of the mud chamber.

In the limit of slow fluidisation relative to pressure diffusion, the mud chamber grows asymptotically towards a final radius of $(\sigma_T - \Delta p)/\mathcal{G}$, where σ_T is the tensile strength of the seal, Δp is the pressure jump across the fluidisation front and $\mathcal{G}$ is the critical pressure gradient for fluidisation. Using estimates of mudstone properties, I calculated mud chamber sizes that are comparable to the sizes of mud-depletion zones beneath mud volcanoes in the Nile Deep Sea Fan. I therefore provided supporting evidence for this theory of fluidisation during mud volcano eruptions.

5.2 Future work

The models of fluid venting developed in this thesis constitute tractable tools for understanding the general dynamics of venting. By only including the dominant physical processes, these models allow for the systematic exploration of the parameter space. Accordingly, through relatively simple extensions, these models can be tailored to investigate a wide range of settings. In this section, I propose a number of potential model extensions and promising avenues of future work.

5.2.1 Dynamics of the venting conduit

In this thesis, I have investigated how fluid flow in the source region influences the dynamics of fluid venting. However, there is a two-way coupling between the flow in the source region and the flow in the venting conduit. Venting conduits commonly transport overpressured hydrocarbons, especially natural gas, from depths of kilometres. For the high pressures in the source region at depth, gas may be dissolved in liquid

hydrocarbons (if they are present) or in the resident brine. But the pressure decreases as the fluid mixture travels up the conduit, allowing for the exsolution of the dissolved gas (Collignon et al. 2018). This process is similar to exsolving flows in igneous-volcanic conduits (Fowler & Robinson 2018) and occurs in hydrocarbon-extraction wells (Shoham 2006). Past models of multiphase flow in extraction wells have mainly relied on empirical correlations (Poettman & Carpenter 1952, Hagedorn & Brown 1965, Beggs & Brill 1973), which are restricted to the systems where the correlations were made. However, more recent mechanical models have reduced these restrictions (Cazarez-Candia & Vásquez-Cruz 2005, Shoham 2006). In particular, Pereira & Fowler (2020) propose a simple mathematical model of flow in extraction wells that explicitly accounts for the kinetics of gas bubble nucleation and growth. This tractable well model could be combined with the models derived in this thesis to investigate the coupled physics of the conduit and the source region. This combined model may, for example, help to explain the observed nonlinear venting behaviour of mud volcanoes (Deville & Guerlais 2009).

In the Eastern Mediterranean, venting conduits transport fluids through a thick, viscous salt layer. Over long timescales, salt flows towards regions of low pressure. Therefore, pressure losses in the venting conduit will promote the closure of the conduit by viscous creep. However, this viscous creep is opposed by the dissolution of the conduit walls (Dupré et al. 2014) and, potentially, the erosive fluidisation of the conduit walls (Cartwright & Santamarina 2015). A model of venting conduits that considers these effects may shed light on their radii and the flow rates through them, as well as their conditions for closure. Such a model may be similar to models of the closure of open wellbores in salt (Weijermars et al. 2014), englacial meltwater conduits (Dallaston & Hewitt 2014) and igneous-volcanic conduits (Quareni & Mulargia 1993, Macedonio et al. 1994). Indeed, like igneous-volcanic conduits, fluid venting conduits may close by brittle collapse; mud volcanoes can form structures analogous to calderas (Evans et al. 2008).

5.2.2 Extensions to theory of mud volcanism

The results of Chapter 4 provide evidence to suggest that the final size of mud-depletion zones is governed by the cohesion and buoyant weight of the sediments. These resistive forces also determine the shapes of mud-depletion zones, though this feature of depletion zones is only briefly explored in this work. A systematic investigation of the shapes of depletion zones likely requires the solution of the full two-dimensional model derived in Chapter 4. However in this two-dimensional model, the growth of the fluidisation front is unstable to any frequency of perturbation. To correct this non-physical behaviour in the model, I suggest a rigorous treatment of the energetic cost of breaking intergranular bonds during fluidisation. This treatment may be derived using analogous concepts from fracture mechanics and capillarity. For example, a capillary energy suggests that the pressure jump across the fluidisation front is dependent on the local curvature; this is analogous to the Gibbs-Thomson effect that is encountered during melting and solidification. It follows that below a critical mud-chamber radius, all perturbations to the fluidisation front are suppressed; beyond this radius a preferred frequency of perturbation grows (see Mullins & Sekerka 1963). Complementary experiments for these two-dimensional simulations could involve the rapid extraction of fluid from a pressurised packing of hydrogel beads.

The earliest stage of mud volcanism is typically observed to be a vigorous fluid-rich eruption. The theory of mud volcanism developed in this thesis shows that this initial fluid-rich eruption drives mudstone remobilisation. However, it remains unclear how a low-permeability mudstone can initially provide a rapid supply of fluids to the venting conduit. Experiments by Nichols et al. (1994) suggest that, prior to eruption, fluids may accumulate in a conical void at the base of the sealing layer. The possibility of prior voids suggests that fluidisation may initiate from a distributed region at the base of the

sealing layer, rather than from a point at the base of the venting conduit, as is assumed in this work. This lack of clarity in the earliest stage of mud volcanism motivates further experimental and theoretical studies of the source regions of mud volcanoes.

The extrusion of mud from the subsurface reduces the pressure exerted by the source region on the overlying layer. This pressure reduction drives the subsidence of the overlying layer into the source region. Dupuis et al. (2019) propose that the subsidence of the overlying layer drove the eruptions of a suite of mud volcanoes in offshore Nigeria by an analogous process to the brittle collapse of magmatic calderas. This brittle collapse is unlikely in the Nile Deep Sea Fan as the overlying layer is a viscous salt sheet; instead, subsidence likely occurred by the viscous flow of salt. Cartwright et al. (2023) argue that the rate of extrusion from mud volcanoes is likely faster than the corresponding salt flow in the Nile Deep Sea Fan. This justifies our assumption of a rigid salt layer in Chapter 4 if the extrusion of mud is continuous over long timescales. However, seismic evidence suggests that mud extrusion in the Nile Deep Sea Fan may be episodic (Cartwright et al. 2023). In this case, the salt is able to flow into the mud chamber during long periods of quiescence. This process has implications for the shapes of mud-depletion zones and may set the frequency of mud volcano eruptions. An extended model that considers salt flow would allow the dynamics of mud volcanism in the Eastern Mediterranean to be more thoroughly investigated.

The model derived in this thesis can be readily tailored for the study of mud volcanoes in other sedimentary basins. In contrast to the mud volcanoes in the Nile Deep Sea Fan, other mud volcanoes typically source fluids from a separate stratigraphic layer to the mudstone. This is the case for the Lusi mud volcano, which has displaced thousands of nearby families since it began erupting in 2006 (Davies et al. 2011). Management of this disaster is difficult without an understanding of the likely evolution of the eruption. Davies et al. (2011) estimate the duration of the Lusi eruption by modelling the evolution

of the fluid source, but they neglect the evolution of the mud source. Therefore, their estimates could be improved by modifying the model developed in this thesis to add a separate fluid source.

A final area of unexplored curiosity is that of sediment production during industrial processes such as the production of subsurface fluids from a well. At high rates of production, the fluids are often accompanied by fluidised sediment sourced from the reservoir rock (Vardoulakis et al. 1996). This fluidised sediment can impede fluid production by filling and blocking the wellbore and eroding the production equipment (Subbiah et al. 2021). To understand this risk, numerous models have been developed to predict the onset and evolution of sediment production (see Rahmati et al. 2013). Many such models carry considerable numerical complexity, which may delay the determination of an optimised production strategy and thus its execution. For a much reduced computational cost, the model developed in this work can be easily adapted to predict the dynamics of sediment production from wells.

Bibliography

Abramian, A., Devauchelle, O. & Lajeunesse, E. (2020), 'Laboratory rivers adjust their shape to sediment transport', *Physical Review E* **102**(5), 053101.

Abramson, E. H. (2007), 'Viscosity of water measured to pressures of 6 GPa and temperatures of 300°C', *Physical Review E* **76**(5), 051203.

Akhbari, D. & Hesse, M. A. (2017), 'Causes of underpressure in natural CO_2 reservoirs and implications for geological storage', *Geology* **45**(1), 47–50.

Al-Balushi, A. N., Neumaier, M., Fraser, A. J. & Jackson, C. A. (2016), 'The impact of the Messinian salinity crisis on the petroleum system of the Eastern Mediterranean: a critical assessment using 2D petroleum system modelling', *Petroleum Geoscience* **22**(4), 357–379.

Andresen, K. J. & Huuse, M. (2011), 'Bulls-eye pockmarks and polygonal faulting in the Lower Congo Basin: Relative timing and implications for fluid expulsion during shallow burial', *Marine Geology* **279**(1-4), 111–127.

Arts, R., Eiken, O., Chadwick, A., Zweigel, P., van der Meer, B. & Kirby, G. (2004), 'Seismic monitoring at the Sleipner underground CO_2 storage site (North Sea)', *Geological Society, London, Special Publications* **233**(1), 181–191.

Barr, K. & Bolli, H. (1953), 'The mud volcanoes of Trinidad', *Caribbean Quarterly* **3**(2), 80–85.

Beggs, D. H. & Brill, J. P. (1973), 'A study of two-phase flow in inclined pipes', *Journal of Petroleum technology* **25**(05), 607–617.

Bell, F. G. (1983), *Engineering Properties of Soils and Rocks*, Elsevier.

Bérest, P., Brouard, B., Favret, F., Hévin, G. & Karimi-Jafari, M. (2015), Maximum pressure in gas storage caverns, *in* 'Proceedings of the SMRI Spring 2015 Technical Conference', SMRI, Rochester, NY.

Bertoni, C., Kirkham, C., Cartwright, J., Hodgson, N. & Rodriguez, K. (2017), 'Seismic indicators of focused fluid flow and cross-evaporitic seepage in the Eastern Mediterranean', *Marine and Petroleum Geology* **88**, 472–488.

Biot, M. A. (1941), 'General theory of three-dimensional consolidation', *Journal of Applied Physics* **12**(2), 155–164.

Bird, B. R., Stewart, W. E. & Lightfoot, E. N. (2002), *Transport phenomena*, John Wiley & Sons.

Blouin, A., Sultan, N., Callot, J.-P. & Imbert, P. (2019), 'Sediment damage caused by gas exsolution: A key mechanism for mud volcano formation', *Engineering Geology* **263**, 105313.

Bock, H., Dehandschutter, B., Martin, C. D., Mazurek, M., De Haller, A., Skoczylas, F. & Davy, C. (2010), 'Self-sealing of fractures in argillaceous formations in the context of geological disposal of radioactive waste', *OECD/NEA Report* **6184**, 310.

Bou Daher, S., Ducros, M., Michel, P., Hawie, N., Nader, F. H. & Littke, R. (2016), '3D thermal history and maturity modelling of the Levant Basin and its eastern margin, offshore–onshore Lebanon', *Arabian Journal of Geosciences* **9**, 1–26.

Bredehoeft, J. & Hanshaw, B. (1968), 'On the maintenance of anomalous fluid pressures: I. Thick sedimentary sequences', *Geological Society of America Bulletin* **79**(9), 1097–1106.

Bristow, C., Gale, I., Fellman, E., Cox, B., Wilkinson, I. & Riding, J. (2000), 'The lithostratigraphy, biostratigraphy and hydrogeological significance of the mud springs at Templars Firs, Wootton Bassett, Wiltshire', *Proceedings of the Geologists' Association* **111**(3), 231–245.

Brown, K. M. (1990), 'The nature and hydrogeologic significance of mud diapirs and diatremes for accretionary systems', *Journal of Geophysical Research: Solid Earth* **95**(B6), 8969–8982.

Byrne, D. E., Wang, W.-h. & Davis, D. M. (1993), 'Mechanical role of backstops in the growth of forearcs', *Tectonics* **12**(1), 123–144.

Carslaw, H. S. & Jaeger, J. C. (1959), *Conduction of heat in solids*, Clarendon Press.

Cartwright, J., Kirkham, C., Bertoni, C., Hodgson, N. & Rodriguez, K. (2018), 'Direct calibration of salt sheet kinematics during gravity-driven deformation', *Geology* **46**(7), 623–626.

Cartwright, J., Kirkham, C., Espinoza, D. N., James, D. & Hodgson, N. (2023), 'The evolution of depletion zones beneath mud volcanoes', *Marine and Petroleum Geology* **155**, 106351.

Cartwright, J., Kirkham, C., Foschi, M., Hodgson, N., Rodriguez, K. & James, D. (2021), 'Quantitative reconstruction of pore-pressure history in sedimentary basins using fluid escape pipes', *Geology* **49**(5), 576–580.

Cartwright, J. & Santamarina, C. (2015), 'Seismic characteristics of fluid escape pipes in sedimentary basins: implications for pipe genesis', *Marine and Petroleum Geology* **65**, 126–140.

Casey, B. B. A. (2014), The consolidation and strength behavior of mechanically compressed fine-grained sediments, PhD thesis, Massachusetts Institute of Technology.

Cathles, L. (2019), 'On the processes that produce hydrocarbon and mineral resources in sedimentary basins', *Geosciences* **9**(12), 520.

Cathles, L. & Smith, A. (1983), 'Thermal constraints on the formation of Mississippi Valley-type lead-zinc deposits and their implications for episodic basin dewatering and deposit genesis', *Economic Geology* **78**(5), 983–1002.

Cavanagh, A. J. & Haszeldine, R. S. (2014), 'The Sleipner storage site: Capillary flow modeling of a layered CO_2 plume requires fractured shale barriers within the Utsira Formation', *International Journal of Greenhouse Gas Control* **21**, 101–112.

Cazarez-Candia, O. & Vásquez-Cruz, M. A. (2005), 'Prediction of pressure, temperature, and velocity distribution of two-phase flow in oil wells', *Journal of Petroleum Science and Engineering* **46**(3), 195–208.

Chang, K. W., Hesse, M. A. & Nicot, J.-P. (2013*a*), 'Dissipation of overpressure into ambient mudrocks during geological carbon dioxide storage', *Energy Procedia* **37**, 4457–4464.

Chang, K. W., Hesse, M. A. & Nicot, J.-P. (2013*b*), 'Reduction of lateral pressure propagation due to dissipation into ambient mudrocks during geological carbon dioxide storage', *Water Resources Research* **49**(5), 2573–2588.

Chen, J., Ren, S., Yang, C., Jiang, D. & Li, L. (2013), 'Self-healing characteristics of damaged rock salt under different healing conditions', *Materials* **6**(8), 3438–3450.

Chen, S., Yu, H., Lu, M., Lebedev, M., Li, X., Yang, Z., Cheng, W., Yuan, Y., Ding, S. & Johnson, L. (2022), 'A new approach to calculate gas saturation in shale reservoirs', *Energy & Fuels* **36**(4), 1904–1915.

Collignon, M., Mazzini, A., Schmid, D. W. & Lupi, M. (2018), 'Modelling fluid flow in active clastic piercements: Challenges and approaches', *Marine and Petroleum Geology* **90**, 157–172.

Dallaston, M. C. & Hewitt, I. J. (2014), 'Free-boundary models of a meltwater conduit', *Physics of Fluids* **26**(8).

Davies, R. J., Mathias, S. A., Swarbrick, R. E. & Tingay, M. J. (2011), 'Probabilistic longevity estimate for the Lusi mud volcano, east java', *Journal of the Geological Society* **168**(2), 517–523.

De Wit, C. & Arens, P. (1950), Moisture content and density of some clay minerals and some remarks on the hydration pattern of clay, *in* 'Transactions of the International Congress of Soil Science, Amsterdam, 1950', pp. 3–3.

Deville, E. & Guerlais, S.-H. (2009), 'Cyclic activity of mud volcanoes: evidences from Trinidad (SE Caribbean)', *Marine and Petroleum Geology* **26**(9), 1681–1691.

Deville, É., Guerlais, S.-H., Lallemant, S. & Schneider, F. (2010), 'Fluid dynamics and subsurface sediment mobilization processes: an overview from Southeast Caribbean', *Basin Research* **22**(4), 361–379.

Dewers, T. & Ortoleva, P. (1994), 'Nonlinear dynamical aspects of deep basin hydrology; fluid

compartment formation and episodic fluid release', *American Journal of Science* **294**(6), 713–755.

Dewynne, J., Howison, S., Ockendon, J. & Xie, W. (1989), 'Asymptotic behavior of solutions to the Stefan problem with a kinetic condition at the free boundary', *The ANZIAM Journal* **31**(1), 81–96.

Dewynne, J. N. (1990), A survey of supercooled Stefan problems, *in* 'Mini-Conference on Free and Moving Boundary and Diffusion Problems', Vol. 30, Centre for Mathematical Analysis, ANU, Canberra, Australia, pp. 42–56.

Duan, Z. & Mao, S. (2006), 'A thermodynamic model for calculating methane solubility, density and gas phase composition of methane-bearing aqueous fluids from 273 to 523 k and from 1 to 2000 bar', *Geochimica et Cosmochimica Acta* **70**(13), 3369–3386.

Dupré, S., Mascle, J., Foucher, J.-P., Harmegnies, F., Woodside, J. & Pierre, C. (2014), 'Warm brine lakes in craters of active mud volcanoes, Menes caldera off NW Egypt: evidence for deep-rooted thermogenic processes', *Geo-Marine Letters* **34**, 153–168.

Dupuis, M., Imbert, P., Odonne, F. & Vendeville, B. (2019), 'Mud volcanism by repeated roof collapse: 3D architecture and evolution of a mud volcano cluster offshore Nigeria', *Marine and Petroleum Geology* **110**, 368–387.

Evans, R. J., Stewart, S. A. & Davies, R. J. (2008), 'The structure and formation of mud volcano summit calderas', *Journal of the Geological Society* **165**(4), 769–780.

Evans, S. L., Jackson, C. A.-L. & Oppo, D. (2020), 'Taking the pulse of salt-detached gravity gliding in the eastern Mediterranean', *Tectonics* pp. 1798–1819.

Fasano, A. & Primicerio, M. (1981), 'New results on some classical parabolic free-boundary problems', *Quarterly of Applied Mathematics* **38**(4), 439–460.

Fasano, A., Primicerio, M., Howison, S. & Ockendon, J. (1989), 'On the singularities of one-dimensional Stefan problems with supercooling', *Mathematical Models for Phase Change Problems* pp. 215–226.

Fasano, A., Primicerio, M., Howison, S. & Ockendon, J. (1990), 'Some remarks on the regularization of supercooled one-phase Stefan problems in one dimension', *Quarterly of Applied Mathematics* **48**(1), 153–168.

Fine, R. A. & Millero, F. J. (1973), 'Compressibility of water as a function of temperature and pressure', *The Journal of Chemical Physics* **59**(10), 5529–5536.

Flemings, P. B., Stump, B. B., Finkbeiner, T. & Zoback, M. (2002), 'Flow focusing in overpressured sandstones: Theory, observations, and applications', *American Journal of Science* **302**(10), 827–855.

Fowler, A. & Robinson, M. (2018), 'Counter-current convection in a volcanic conduit', *Journal of Volcanology and Geothermal Research* **356**, 141–162.

Fowler, A., Scheu, B., Lee, W. & McGuinness, M. (2010), 'A theoretical model of the explosive fragmentation of vesicular magma', *Proceedings of the Royal Society A: Mathematical, Physical and Engineering Sciences* **466**(2115), 731–752.

Friend, D. G., Ely, J. F. & Ingham, H. (1989), 'Tables for the thermophysical properties of methane', *National Institute of Standards and Technology* **1325**, 1–496.

Gay, A., Lopez, M., Cochonat, P., Levaché, D., Sermondadaz, G. & Seranne, M. (2006b), 'Evidences of early to late fluid migration from an upper Miocene turbiditic channel revealed by 3D seismic coupled to geochemical sampling within seafloor pockmarks, Lower Congo Basin', *Marine and Petroleum Geology* **23**(3), 387–399.

Gay, A., Lopez, M., Cochonat, P., Séranne, M., Levaché, D. & Sermondadaz, G. (2006a), 'Isolated seafloor pockmarks linked to BSRs, fluid chimneys, polygonal faults and stacked Oligocene–Miocene turbiditic palaeochannels in the Lower Congo Basin', *Marine Geology* **226**(1-2), 25–40.

Ge, S. & Garven, G. (1992), 'Hydromechanical modeling of tectonically driven groundwater flow with application to the Arkoma foreland basin', *Journal of Geophysical Research: Solid Earth* **97**(B6), 9119–9144.

Geldart, D. (1973), 'Types of gas fluidization', *Powder Technology* **7**(5), 285–292.

Ghalayini, R., Nader, F., Bou Daher, S., Hawie, N. & Chbat, W. (2018), 'Petroleum systems of Lebanon: An update and review', *Journal of Petroleum Geology* **41**(2), 189–214.

Ghanbarzadeh, S., Hesse, M. A., Prodanović, M. & Gardner, J. E. (2015), 'Deformation-assisted fluid percolation in rock salt', *Science* **350**(6264), 1069–1072.

Giresse, P., Loncke, L., Huguen, C., Muller, C. & Mascle, J. (2010), 'Nature and origin of sedimentary clasts associated with mud volcanoes in the Nile deep-sea fan. relationships with fluid venting', *Sedimentary Geology* **228**(3-4), 229–245.

Goldstein, S. (1932), 'Some two-dimensional diffusion problems with circular symmetry', *Proceedings of the London Mathematical Society* **2**(1), 51–88.

Graue, K. (2000), 'Mud volcanoes in deepwater Nigeria', *Marine and Petroleum Geology* **17**(8), 959–974.

Grauls, D. & Baleix, J. (1994), 'Role of overpressures and in situ stresses in fault-controlled hydrocarbon migration: A case study', *Marine and Petroleum Geology* **11**(6), 734–742.

Hagedorn, A. R. & Brown, K. E. (1965), 'Experimental study of pressure gradients occurring during continuous two-phase flow in small-diameter vertical conduits', *Journal of Petroleum technology* **17**(04), 475–484.

Hastings, W. K. (1970), 'Monte Carlo sampling methods using Markov chains and their applications', *Biometrika* **57**, 97–109.

Heinemann, N., Alcalde, J., Miocic, J. M., Hangx, S. J., Kallmeyer, J., Ostertag-Henning, C., Hassanpouryouzband, A., Thaysen, E. M., Strobel, G. J., Schmidt-Hattenberger, C. et al. (2021), 'Enabling large-scale hydrogen storage in porous media–the scientific challenges', *Energy & Environmental Science* **14**(2), 853–864.

Hewitt, D. R. & Balmforth, N. J. (2013), 'Thixotropic gravity currents', *Journal of Fluid Mechanics* **727**, 56–82.

Higgins, G. (1974), 'Mud volcanoes—their nature and origin', *Verhandlungen der Naturforschenden Gesellschaft in Basel* **84**, 101–152.

Hovland, M. & Judd, A. G. (1988), *Seabed pockmarks and seepages: impact on geology, biology, and the marine environment*, Graham & Trotman.

Howison, S., Ockendon, J. & Lacey, A. (1985), 'Singularity development in moving-boundary problems', *The Quarterly Journal of Mechanics and Applied Mathematics* **38**(3), 343–360.

Huppert, H. E. & Neufeld, J. A. (2014), 'The fluid mechanics of carbon dioxide sequestration', *Annual Review of Fluid Mechanics* **46**, 255–272.

Huuse, M., Jackson, C. A.-L., Van Rensbergen, P., Davies, R. J., Flemings, P. B. & Dixon, R. J. (2010), 'Subsurface sediment remobilization and fluid flow in sedimentary basins: an overview', *Basin Research* **22**(4), 342–360.

Huuse, M., Shoulders, S. J., Netoff, D. I. & Cartwright, J. (2005), 'Giant sandstone pipes record basin-scale liquefaction of buried dune sands in the Middle Jurassic of SE Utah', *Terra Nova* **17**(1), 80–85.

Jerolmack, D. J. & Daniels, K. E. (2019), 'Viewing Earth's surface as a soft-matter landscape', *Nature Reviews Physics* **1**(12), 716–730.

Jones, M. (1994), Mechanical principles of sediment deformation, *in* 'The geological deformation of sediments', Springer, pp. 37–71.

Kahle, H.-G., Straub, C., Reilinger, R., McClusky, S., King, R., Hurst, K., Veis, G., Kastens, K. & Cross, P. (1998), 'The strain rate field in the eastern Mediterranean region, estimated by repeated GPS measurements', *Tectonophysics* **294**(3-4), 237–252.

Kass, R. E. & Raftery, A. E. (1995), 'Bayes factors', *Journal of the American Statistical Association* **90**(430), 773–795.

Katz, R. F. (2022), *The dynamics of partially molten rock*, Princeton University Press.

Kearney, L. M., Katz, R. F., MacMinn, C. W., Kirkham, C. & Cartwright, J. (2024), 'Episodic

fluid venting from sedimentary basins fueled by pressurized mudstones', *Proceedings of the National Academy of Sciences* **121**(8), e2312152121. (doi:10.1073/pnas.2312152121).

Kearney, L. M., MacMinn, C. W., Katz, R. F., Kirkham, C. & Cartwright, J. (2023), 'Episodic, compression-driven fluid venting in layered sedimentary basins', *Proceedings of the Royal Society A: Mathematical, Physical and Engineering Sciences* **479**(2274), 20220654. (doi:10.1098/rspa.2022.0654).

Kell, G. & Whalley, E. (1975), 'Reanalysis of the density of liquid water in the range 0–150 c and 0–1 kbar', *The Journal of Chemical Physics* **62**(9), 3496–3503.

King, J. & Riley, D. (2000), 'Asymptotic solutions to the Stefan problem with a constant heat source at the moving boundary', *Proceedings of the Royal Society of London. Series A: Mathematical, Physical and Engineering Sciences* **456**(1997), 1163–1174.

Kirkham, C., Cartwright, J., Hermanrud, C. & Jebsen, C. (2017), 'The spatial, temporal and volumetric analysis of a large mud volcano province within the Eastern Mediterranean', *Marine and Petroleum Geology* **81**, 1–16.

Kirkham, C., Cartwright, J., James, D. & Kearney, L. (2022), 'Episodic venting of extreme subsalt overpressure through a thick evaporitic seal', *Marine and Petroleum Geology* **142**, 105741.

Kopf, A., Deyhle, A., Lavrushin, V. Y., Polyak, B. G., Gieskes, J. M., Buachidze, G. I., Wallmann, K. & Eisenhauer, A. (2003), 'Isotopic evidence (He, B, C) for deep fluid and mud mobilization from mud volcanoes in the Caucasus continental collision zone', *International Journal of Earth Sciences* **92**, 407–425.

Kopf, A. J. (2002), 'Significance of mud volcanism', *Reviews of geophysics* **40**(2), 1–52.

Kopf, A., Robertson, A., Clennell, M. & Flecker, R. (1998), 'Mechanisms of mud extrusion on the Mediterranean Ridge Accretionary Complex', *Geo-Marine Letters* **18**, 97–114.

Kreemer, C., Blewitt, G. & Klein, E. C. (2014), 'A geodetic plate motion and Global Strain Rate Model', *Geochemistry, Geophysics, Geosystems* **15**(10), 3849–3889.

Krevor, S., De Coninck, H., Gasda, S. E., Ghaleigh, N. S., de Gooyert, V., Hajibeygi, H.,

Juanes, R., Neufeld, J., Roberts, J. J. & Swennenhuis, F. (2023), 'Subsurface carbon dioxide and hydrogen storage for a sustainable energy future', *Nature Reviews Earth & Environment* **4**(2), 102–118.

Lazebnik, G. E. & Tsinker, G. P. (1998), Lateral earth pressure "at rest", *in* 'Monitoring of Soil-Structure Interaction: Instruments for Measuring Soil Pressures', Springer, pp. 165–183.

L'Heureux, I. & Fowler, A. D. (2000), 'A simple model of flow patterns in overpressured sedimentary basins with heat transport and fracturing', *Journal of Geophysical Research: Solid Earth* **105**(B10), 23741–23752.

Loncke, L., Mascle, J. & Parties, F. S. (2004), 'Mud volcanoes, gas chimneys, pockmarks and mound in the Nile deep-sea fan (Eastern Mediterranean); geophysical evidences', *Marine and Petroleum Geology* **21**(6), 669–689.

Løseth, H., Wensaas, L., Arntsen, B., Hanken, N., Basire, C. & Graue, K. (2001), 1000 m long gas blow-out pipes, *in* '63rd EAGE Conference & Exhibition', European Association of Geoscientists & Engineers, pp. 1–15.

Løseth, H., Wensaas, L., Arntsen, B., Hanken, N.-M., Basire, C. & Graue, K. (2011), '1000 m long gas blow-out pipes', *Marine and Petroleum Geology* **28**(5), 1047–1060.

Luo, X.-R. (2004), 'Quantitative analysis on overpressuring mechanism resulted from tectonic stress', *Chinese Journal of Geophysics* **47**(6), 1223–1232.

Luo, X. & Vasseur, G. (1997), 'Sealing efficiency of shales', *Terra Nova* **9**(2), 71–74.

Luo, X. & Vasseur, G. (2016), 'Overpressure dissipation mechanisms in sedimentary sections consisting of alternating mud-sand layers', *Marine and Petroleum Geology* **78**, 883–894.

Macedonio, G., Dobran, F. & Neri, A. (1994), 'Erosion processes in volcanic conduits and application to the AD 79 eruption of Vesuvius', *Earth and Planetary Science Letters* **121**(1-2), 137–152.

Maghous, S., Brüch, A., Bernaud, D., Dormieux, L. & Braun, A. (2014), 'Two-dimensional

finite element analysis of gravitational and lateral-driven deformation in sedimentary basins', *International Journal for Numerical and Analytical Methods in Geomechanics* **38**(7), 725–746.

Manga, M., Brumm, M. & Rudolph, M. L. (2009), 'Earthquake triggering of mud volcanoes', *Marine and Petroleum Geology* **26**(9), 1785–1798.

Mascle, J., Mary, F., Praeg, D., Brosolo, L., Camera, L., Ceramicola, S. & Dupré, S. (2014), 'Distribution and geological control of mud volcanoes and other fluid/free gas seepage features in the Mediterranean Sea and nearby Gulf of Cadiz', *Geo-Marine Letters* **34**, 89–110.

Mazzini, A. & Etiope, G. (2017), 'Mud volcanism: An updated review', *Earth-Science Reviews* **168**, 81–112.

Mazzini, A., Svensen, H. H., Forsberg, C. F., Linge, H., Lauritzen, S.-E., Haflidason, H., Hammer, Ø., Planke, S. & Tjelta, T. I. (2017), 'A climatic trigger for the giant Troll pockmark field in the northern north sea', *Earth and Planetary Science Letters* **464**, 24–34.

Moss, J. & Cartwright, J. (2010), 'The spatial and temporal distribution of pipe formation, offshore Namibia', *Marine and Petroleum Geology* **27**(6), 1216–1234.

Muggeridge, A., Abacioglu, Y., England, W. & Smalley, C. (2004), 'Dissipation of anomalous pressures in the subsurface', *Journal of Geophysical Research: Solid Earth* **109**(B11).

Muggeridge, A., Abacioglu, Y., England, W. & Smalley, C. (2005), 'The rate of pressure dissipation from abnormally pressured compartments', *AAPG bulletin* **89**(1), 61–80.

Mullins, W. W. & Sekerka, R. F. (1963), 'Morphological stability of a particle growing by diffusion or heat flow', *Journal of Applied Physics* **34**(2), 323–329.

Muskat, M. (1938), 'The flow of homogeneous fluids through porous media', *Soil Science* **46**(2), 169.

Mutsers, S. & Rietema, K. (1977), 'The effect of interparticle forces on the expansion of a homogeneous gas-fluidized bed', *Powder Technology* **18**(2), 239–248.

Nader, F. H., Inati, L., Ghalayini, R., Hawie, N. & Daher, S. B. (2018), 'Key geological char-

acteristics of the Saida-Tyr Platform along the eastern margin of the Levant Basin, offshore Lebanon: implications for hydrocarbon exploration', *Oil & Gas Science and Technology* **73**, 50.

Nermoen, A., Galland, O., Jettestuen, E., Fristad, K., Podladchikov, Y., Svensen, H. & Malthe-Sørenssen, A. (2010), 'Experimental and analytic modeling of piercement structures', *Journal of Geophysical Research: Solid Earth* **115**(B10).

Neuzil, C. E. (1986), 'Groundwater flow in low-permeability environments', *Water Resources Research* **22**(8), 1163–1195.

Nichols, R., Sparks, R. & Wilson, C. (1994), 'Experimental studies of the fluidization of layered sediments and the formation of fluid escape structures', *Sedimentology* **41**(2), 233–253.

Noble, E. (1963), 'Formation of ore deposits by water of compaction', *Economic Geology* **58**(7), 1145–1156.

Obermeier, S. F. (1996), 'Use of liquefaction-induced features for paleoseismic analysis — an overview of how seismic liquefaction features can be distinguished from other features and how their regional distribution and properties of source sediment can be used to infer the location and strength of Holocene paleo-earthquakes', *Engineering Geology* **44**(1-4), 1–76.

Obradors-Prats, J., Rouainia, M., Aplin, A. C. & Crook, A. J. (2016), 'Stress and pore pressure histories in complex tectonic settings predicted with coupled geomechanical–fluid flow models', *Marine and Petroleum Geology* **76**, 464–477.

Obradors-Prats, J., Rouainia, M., Aplin, A. C. & Crook, A. J. (2017*a*), 'Assessing the implications of tectonic compaction on pore pressure using a coupled geomechanical approach', *Marine and Petroleum Geology* **79**, 31–43.

Obradors-Prats, J., Rouainia, M., Aplin, A. & Crook, A. (2017*b*), 'Hydromechanical modeling of stress, pore pressure, and porosity evolution in fold-and-thrust belt systems', *Journal of Geophysical Research: Solid Earth* **122**(11), 9383–9403.

Okland, D., Gabrielsen, G. K., Gjerde, J., Koen, S. & Williams, E. L. (2002), The importance

of extended leak-off test data for combatting lost circulation, *in* 'SPE/ISRM Rock Mechanics Conference', OnePetro.

Oppo, D., Evans, S., Iacopini, D., Kabir, S. M., Maselli, V. & Jackson, C. A.-L. (2021), 'Leaky salt: Pipe trails record the history of cross-evaporite fluid escape in the northern Levant Basin, Eastern Mediterranean', *Basin Research* **33**(3), 1798–1819.

Ortega, J., Hebert, R. & Gellman, Y. (2018), The dynamic Tamar reservoir: Insights from five years of production, *in* 'Scientific Conference: Eastern Mediterranean—an emerging major petroleum province', pp. 48–49.

Osborne, M. J. & Swarbrick, R. E. (1997), 'Mechanisms for generating overpressure in sedimentary basins: A reevaluation', *AAPG bulletin* **81**(6), 1023–1041.

Palano, M., Imprescia, P. & Gresta, S. (2013), 'Current stress and strain-rate fields across the Dead Sea Fault System: Constraints from seismological data and GPS observations', *Earth and Planetary Science Letters* **369**, 305–316.

Pereira, V. E. & Fowler, A. C. (2020), 'Exsolving two-phase flow in oil wells', *Geophysical & Astrophysical Fluid Dynamics* **114**(3), 283–305.

Pierre, C., Bayon, G., Blanc-Valleron, M.-M., Mascle, J. & Dupré, S. (2014), 'Authigenic carbonates related to active seepage of methane-rich hot brines at the Cheops mud volcano, Menes caldera (Nile deep-sea fan, eastern Mediterranean Sea)', *Geo-Marine Letters* **34**, 253–267.

Planke, S., Svensen, H., Hovland, M., Banks, D. & Jamtveit, B. (2003), 'Mud and fluid migration in active mud volcanoes in Azerbaijan', *Geo-Marine Letters* **23**, 258–268.

Poettman, F. H. & Carpenter, P. G. (1952), The multiphase flow of gas, oil, and water through vertical flow strings with application to the design of gas-lift installations, *in* 'Drilling and Production practice', OnePetro.

Price, N. J. & Cosgrove, J. W. (1990), *Analysis of geological structures*, Cambridge University Press.

Prinzhofer, A. & Deville, E. (2013), 'Origins of hydrocarbon gas seeping out from offshore mud volcanoes in the Nile delta', *Tectonophysics* **591**, 52–61.

Pryce, E., Kirkham, C. & Cartwright, J. (2023), 'Crater formation during the onset of mud volcanism', *Geology* **51**(3), 252–256.

Quareni, F. & Mulargia, F. (1993), 'Modeling the closure of volcanic conduits with an application to Mount Vesuvius', *Journal of Geophysical Research: Solid Earth* **98**(B3), 4221–4229.

Raaen, A., Horsrud, P., Kjørholt, H. & Økland, D. (2006), 'Improved routine estimation of the minimum horizontal stress component from extended leak-off tests', *International Journal of Rock Mechanics and Mining Sciences* **43**(1), 37–48.

Rahmati, H., Jafarpour, M., Azadbakht, S., Nouri, A., Vaziri, H., Chan, D. & Xiao, Y. (2013), 'Review of sand production prediction models', *Journal of Petroleum Engineering* **2013**(1), 864981.

Reilly, M. J. & Flemings, P. B. (2010), 'Deep pore pressures and seafloor venting in the Auger Basin, Gulf of Mexico', *Basin Research* **22**(4), 380–397.

Rice, J. & Budiansky, B. (1973), 'Conservation laws and energy-release rates', *Journal of Applied Mechanics* **40**, 201–203.

Richards, K. S. & Reddy, K. R. (2007), 'Critical appraisal of piping phenomena in earth dams', *Bulletin of Engineering Geology and the Environment* **66**, 381–402.

Richardson, J. (1971), 'Incipient fluidization and particulate systems', *Fluidization* **2**, 25–64.

Rietema, K. (1984), 'Powders, what are they', *Powder Technology* **37**(5).

Ringrose, P. S., Furre, A.-K., Gilfillan, S. M., Krevor, S., Landrø, M., Leslie, R., Meckel, T., Nazarian, B. & Zahid, A. (2021), 'Storage of carbon dioxide in saline aquifers: physicochemical processes, key constraints, and scale-up potential', *Annual Review of Chemical and Biomolecular Engineering* **12**, 471–494.

Ringrose, P. S. & Meckel, T. A. (2019), 'Maturing global CO_2 storage resources on offshore continental margins to achieve 2DS emissions reductions', *Scientific reports* **9**(1), 1–10.

Roberts, K., Davies, R. & Stewart, S. (2010), 'Structure of exhumed mud volcano feeder complexes, Azerbaijan', *Basin Research* **22**(4), 439–451.

Roberts, S. J. & Nunn, J. A. (1995), 'Episodic fluid expulsion from geopressured sediments', *Marine and Petroleum Geology* **12**(2), 195–204.

Robertson, A. (1996), 'Mud volcanism on the Mediterranean Ridge: Initial results of ocean drilling program Leg 160', *Geology* **24**(3), 239–242.

Rocha, L. A. S. (1993), Mechanisms of Crater Formation While Drilling a Well, PhD thesis, Louisiana State University.

Rudolph, M. L., Karlstrom, L. & Manga, M. (2011), 'A prediction of the longevity of the Lusi mud eruption, Indonesia', *Earth and Planetary Science Letters* **308**(1-2), 124–130.

Ryan, W. B. (2009), 'Decoding the Mediterranean salinity crisis', *Sedimentology* **56**(1), 95–136.

Saffman, P. G. & Taylor, G. I. (1958), 'The penetration of a fluid into a porous medium or Hele-Shaw cell containing a more viscous liquid', *Proceedings of the Royal Society of London. Series A. Mathematical and Physical Sciences* **245**(1242), 312–329.

Sathaye, K. J., Hesse, M. A., Cassidy, M. & Stockli, D. F. (2014), 'Constraints on the magnitude and rate of CO_2 dissolution at Bravo Dome natural gas field', *Proceedings of the National Academy of Sciences* **111**(43), 15332–15337.

Scandella, B. P., Varadharajan, C., Hemond, H. F., Ruppel, C. & Juanes, R. (2011), 'A conduit dilation model of methane venting from lake sediments', *Geophysical Research Letters* **38**(6).

Shaikh, A., Ruff, J. F. & Abt, S. R. (1988), 'Erosion rate of compacted Na-montmorillonite soils', *Journal of geotechnical engineering* **114**(3), 296–305.

Sherman, B. (1970), 'A general one-phase Stefan problem', *Quarterly of Applied Mathematics* **28**(3), 377–382.

Shoham, O. (2006), *Mechanistic modeling of gas-liquid two-phase flow in pipes*, Society of Petroleum Engineers.

Stewart, S. A. & Davies, R. J. (2006), 'Structure and emplacement of mud volcano systems in the South Caspian Basin', *AAPG bulletin* **90**(5), 771–786.

Subbiah, S. K., Samsuri, A., Mohamad-Hussein, A., Jaafar, M. Z., Chen, Y. R. & Kumar, R. R. (2021), 'Root cause of sand production and methodologies for prediction', *Petroleum* **7**(3), 263–271.

Tingay, M. (2010), 'Anatomy of the Lusi mud eruption, East Java', *ASEG Extended Abstracts* **2010**(1), 1–6.

Tingay, M., Manga, M., Rudolph, M. L. & Davies, R. (2018), 'An alternative review of facts, coincidences and past and future studies of the Lusi eruption', *Marine and Petroleum Geology* **95**, 345–361.

Tingay, M. R., Hillis, R. R., Swarbrick, R. E., Morley, C. K. & Damit, A. R. (2007), "Vertically transferred' overpressures in Brunei: Evidence for a new mechanism for the formation of high-magnitude overpressure', *Geology* **35**(11), 1023–1026.

Tingay, M., Rudolph, M., Manga, M., Davies, R. J. & Wang, C.-Y. (2015), 'Initiation of the Lusi mudflow disaster', *Nature Geoscience* **8**(7), 493–494.

Tribelsky, M. I. & Anisimov, S. I. (2014), 'Tuned Mullins–Sekerka instability: Exact results', *Physical Review E* **90**(4), 042403.

Vardoulakis, I. (2004), 'Fluidisation in artesian flow conditions: Hydromechanically stable granular media', *Geotechnique* **54**(2), 117–130.

Vardoulakis, I., Stavropoulou, M. & Papanastasiou, P. (1996), 'Hydro-mechanical aspects of the sand production problem', *Transport in Porous Media* **22**, 225–244.

Verruijt, A. (1969), 'Elastic storage of aquifers', *Flow through Porous Media* **1**, 331–376.

Weijermars, R., Jackson, M. & Van Harmelen, A. (2014), 'Closure of open wellbores in creeping salt sheets', *Geophysical Journal International* **196**(1), 279–290.

Yang, Y. & Aplin, A. C. (2007), 'Permeability and petrophysical properties of 30 natural mudstones', *Journal of Geophysical Research: Solid Earth* **112**(B3).

Yassir, N. A. (1989), Mud volcanoes and the behaviour of overpressured clays and silts, PhD thesis, University of London.

Yilmaz, Ö. (2001), *Seismic data analysis: Processing, inversion, and interpretation of seismic data*, Society of Exploration Geophysicists.

Zoporowski, A. & Miller, S. A. (2009), 'Modelling eruption cycles and decay of mud volcanoes', *Marine and Petroleum Geology* **26**(9), 1879–1887.